

New Phytologist Supporting Information

Article title: Coupled whole-tree optimality and xylem-hydraulics explain dynamic biomass partitioning

Authors: Aaron Potkay; Anna T. Trugman; Yujie Wang; Martin D. Venturas; William R. L. Anderegg; Caio R. C. Mattos; Ying Fan

Article acceptance date: 25 January 2021

The following Supporting Information is available for this article:

Fig. S1 Comparison optimal/numerical and gradient ascent approximation for optimization of arbitrary fitness surfaces

Fig. S2 Comparison of optimal allocation methods predicted numerically and by THORP's approximation

Fig. S3 Comparison of observed and THORP-predicted leaf water potentials for the Poblet Forest Natural Reserve site

Fig. S4 Root-shoot ratios simulated by control experiment

Fig. S5 LAI and leaf- and sapwood-area relations under reduced air humidity

Fig. S6 Rooting depth and indices of water-stress simulated by control experiment

Fig. S7 Rooting depth and indices of water-stress simulated by experiment with reduced (75%) precipitation

Fig. S8 Rooting depth and indices of water-stress simulated by experiment with further reduced (50%) precipitation

Fig. S9 Rooting depth and indices of water-stress simulated by experiment with further reduced (50%) precipitation and a shallow, 2 m deep groundwater table

Fig. S10 Measures of water-stress and productivity from eCO₂ experiment

Fig. S11 Shoot-root biomass ratio and total biomass from pruning experiments

Fig. S12 Flowchart of model computations

Fig. S13 Model-observation comparison for the tree-size dependence of stem hydraulic conductance

Table S1 Main variables in THORP

Notes S1 Full Model and Simulation Descriptions.

Notes S2 MATLAB code for model and plotting/analyzing data, including forcing data and simulation outputs.

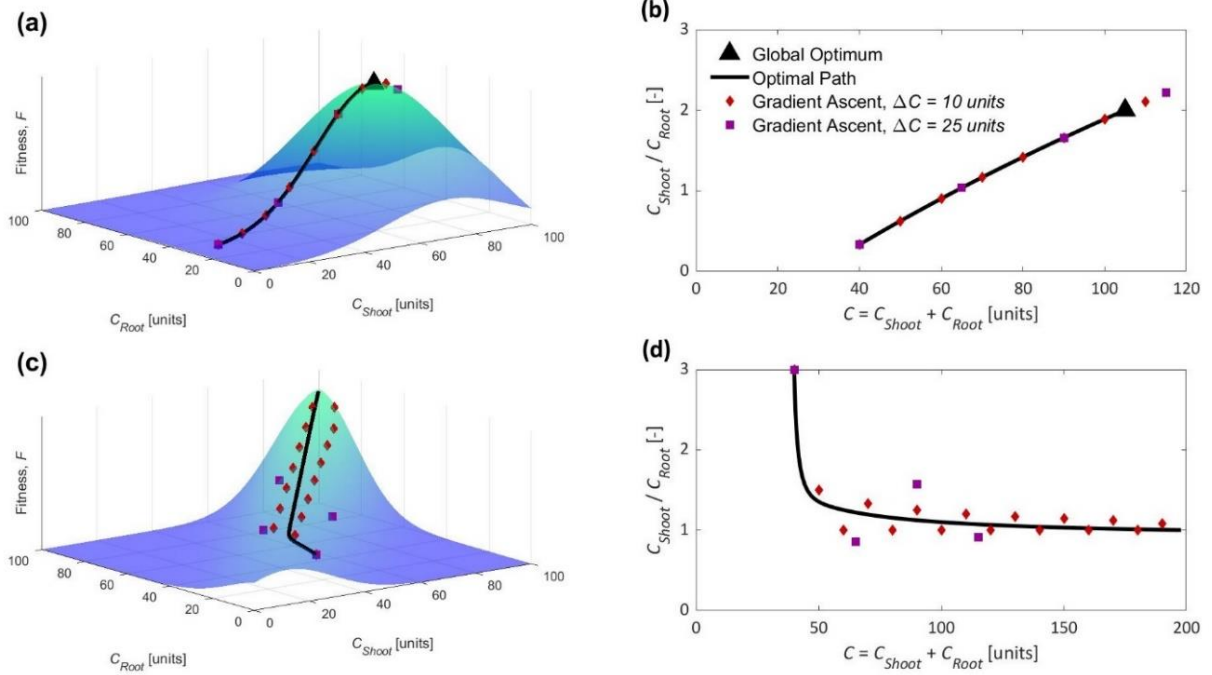


Figure S1: Comparison of true optimal path (black line) and gradient ascent approximation for two arbitrary fitness surfaces, F , (a,c) and corresponding shoot-root ratio (C_{Shoot}/C_{Root}) as a function of total size, C , with two carbon pools ($C = C_{Shoot} + C_{Root}$) (b,d). Surfaces were generated to demonstrate the optimality of the gradient ascent method rather than to accurately describe the shape of the fitness surface sensed by a real tree, because when we introduce the gradient ascent method in our discussion of optimal allocation, we have yet to fully define fitness, which we define later, and because any real fitness surface would not be static but change dynamically in response to environmental drivers. One surface is smooth relative to the size of the allocation increment, ΔC , and has a global optimum (black triangle) (a,b). The second surface is sharper than the first and lacks a global optimum (c,d). Initial coordinates (C_{Shoot} , C_{Root} , F) were arbitrarily chosen, and the true optimal path was solved numerically. Gradient ascent solutions were estimated twice for each surface with different allocation increments of $\Delta C = 10$ units (red diamonds) and $\Delta C = 25$ units (purple squares) to show the sensitivity of the approximation, which depends on both the increment size and the surface's shape. Units are arbitrary in these examples and meaningful only in regard to the size of the domain (100 units for both C_{Shoot} - and C_{Root} -axes).

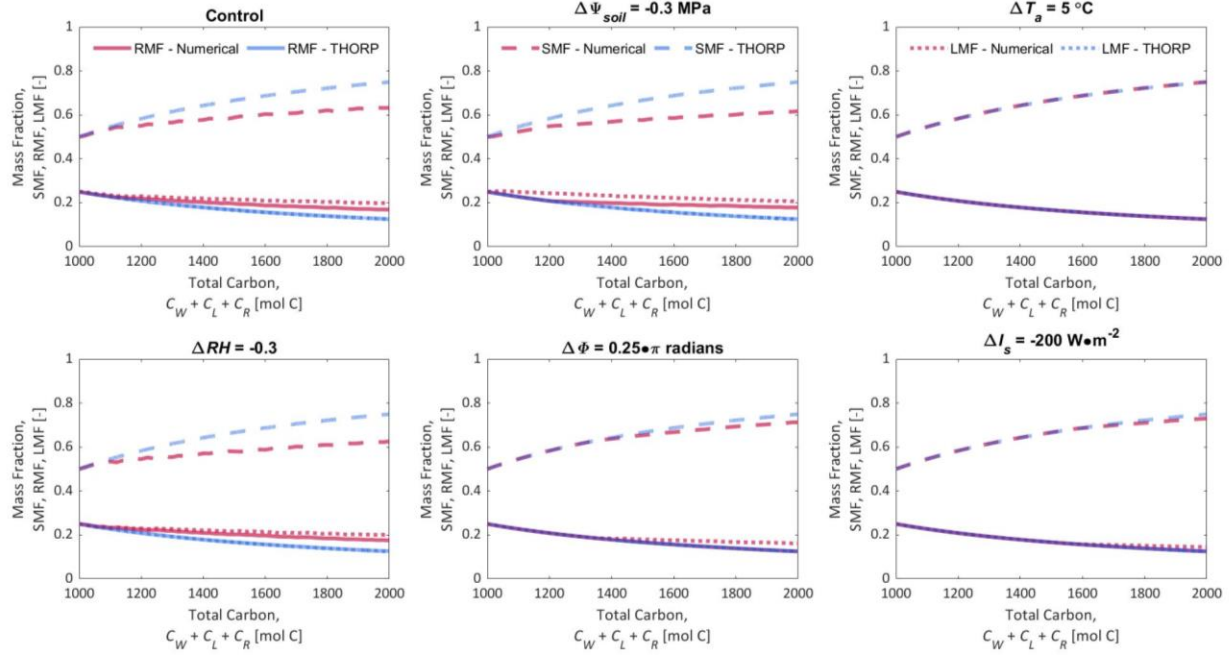


Figure S2: Comparison of true, optimal path that maximizes $a_L \cdot A_n$ (solved numerically and iteratively testing all combinations of potential allocation fractions; red lines) and THORP's allocation method (Eq. S.8.1-3; blue lines) calculated for control experiment (constant environmental conditions; $\Psi_{soil} = -0.55$ MPa, $T_a = 30^\circ\text{C}$, $RH = 0.6$, $I_s = 600 \text{ W}\cdot\text{m}^{-2}$, $\Phi = 0$ radians) and for experiments with modified environmental conditions relative to the control (modifications denoted above each plot). Paths are represented by mass fractions for stems, roots, and leaves (SMF, RMF, and LMF) as a function of the coinciding total carbon. Costs in THORP (both respiratory and senescent) were here set to zero for the sake of comparison between two approaches. Senescence was ignored in each case, and mean lifespans were set equal for the sake of allocation. Experiments represent a simplified case with only a single, 1 m thick soil-root layer. All parameters are the same as shown in Table 3, except we simplified belowground hydraulic resistances into a single parameter instead of solving for interlayer and intralayer root-water fluxes separately ($\beta_{R,H} = 5.1 \cdot 10^3 \text{ MPa}\cdot\text{s}\cdot(\text{mol H}_2\text{O})^{-1}\cdot(\text{mol C})$, $\beta_{R,V} = 0 \text{ MPa}\cdot(\text{mol C})\cdot\text{s}\cdot(\text{mol H}_2\text{O})^{-1}\cdot\text{m}^{-2}$), since we here model a single soil-root layer with only 'horizontal', intralayer-conductive roots.

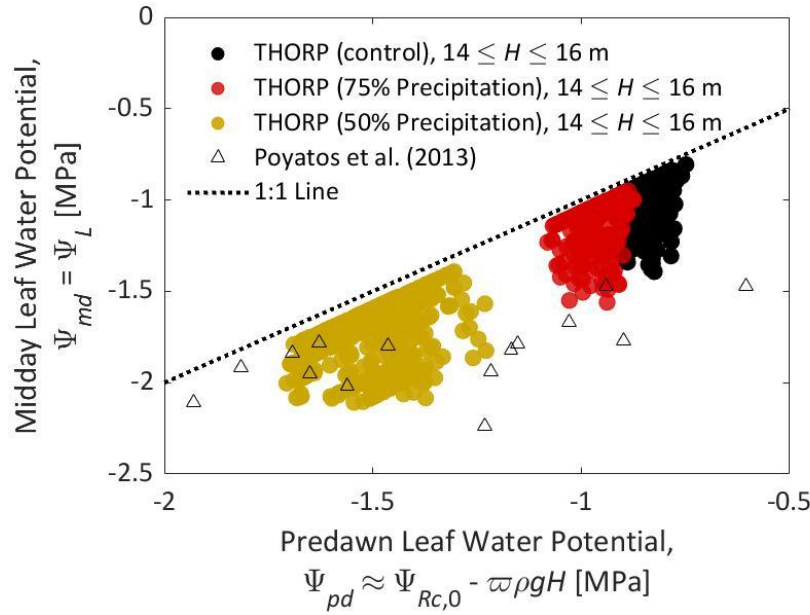


Figure S3: Comparison of predawn and midday leaf water potentials of Scots Pine, Ψ_{pd} and Ψ_{md} , respectively, as reported by Poyatos et al. (2013) for the Poblet Forest Natural Reserve site (triangles) and as predicted by THORP for environmental conditions chosen to partially reflect the same location (circles) (see Section S.10 for discussion of site parameterization). To cover the range of predawn leaf water potentials measured by Poyatos et al. (2013), we show results from THORP as simulated by experiments with full precipitation (black circles; i.e. the control experiment) and reduced precipitation rates: 75% (red circles) and 50% (gold circles) of the precipitation in the control experiment. Poyatos et al. (2013) reported leaf water potentials for trees with heights approximately between 14–16 m for both foliated and defoliated trees, and we show all simulated leaf water potentials predicted by THORP while simulated trees were between the same heights. Additionally, Poyatos et al. (2013) measured midday leaf water potentials on days with ample solar radiation between late summer and early fall, while THORP’s results are shown regardless of season or radiation, and thus we can be satisfied and reasonably trust THORP’s predictions if the bottom envelope of the Ψ_{pd} – Ψ_{md} relationship (i.e. coinciding with relatively warm, sunny days) approximately matches the observations. We estimated Ψ_{pd} for THORP simulations from $\Psi_{Rc,0}$, the root collar water potential expected if there were no transpiration (Eq. S.3.27), minus the hydrostatic, elevation pressure component, $\varpi\rho gH$ (as in Eq. S.3.26). Note that in each simulation with various precipitation regimes, THORP’s full allocation procedures (Section S.8–9) were implemented, so leaf areas, rooting-depths, -masses, and -profiles were allowed to freely adapt to hydrologic conditions throughout each simulation, starting from the same initial allometry (initial $H \approx 4.4$ m; see S.10.1), and may not be comparable between simulations (e.g. Figures 2a,c, 3c,f, S.6a,e, S.7a,e, S.8a,e), which all influence Ψ_{pd} – Ψ_{md} relationships.

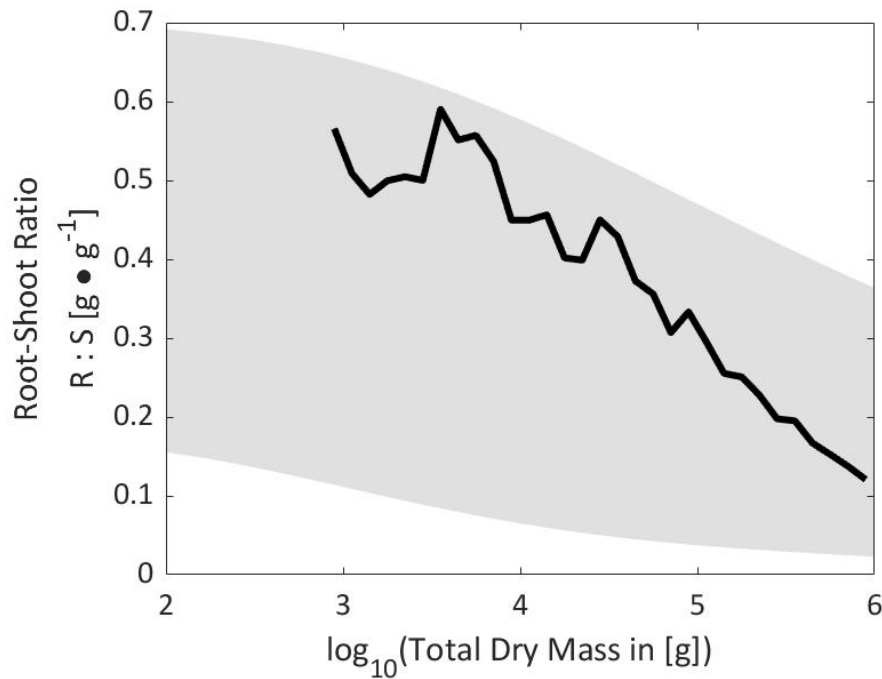


Figure S4: Root-shoot ratio, $R : S$, simulated by control experiment (black line) versus total dry mass. Gray area represents bounds for $R : S$ estimated from the meta-analysis by Poorter et al. (2012). Poorter et al. (2012) did not report the uncertainty of their statistical trends for either $R : S$ or RMF; however, we estimated the bounds of $R : S$ by the method of variance using values extracted from their SI (their Figure S2). To estimate these bounds, we made three assumptions; we assumed that the standard deviations for the base-ten logarithm of leaf- and stem-dry mass in grams (1) were independent of the magnitude of root dry mass, (2) could be approximated by one-fourth of the range of the same values after removing the linear size-trend (i.e. that their ranges approximated ~95% of their theoretical distributions and that the distributions of base-ten logarithm of organ-specific dry masses were normally distributed), and (3) were equal to ~0.37 and ~0.39, respectively, based on Poorter et al.'s (2012) Figure S2. Predictions by THORP were binned into logarithmically-spaced biomass pools ($[10^{3.0}, 10^{3.1}]$, $[10^{3.1}, 10^{3.2}]$, $[10^{3.2}, 10^{3.3}]$, etc.) and averaged to clarify trends.

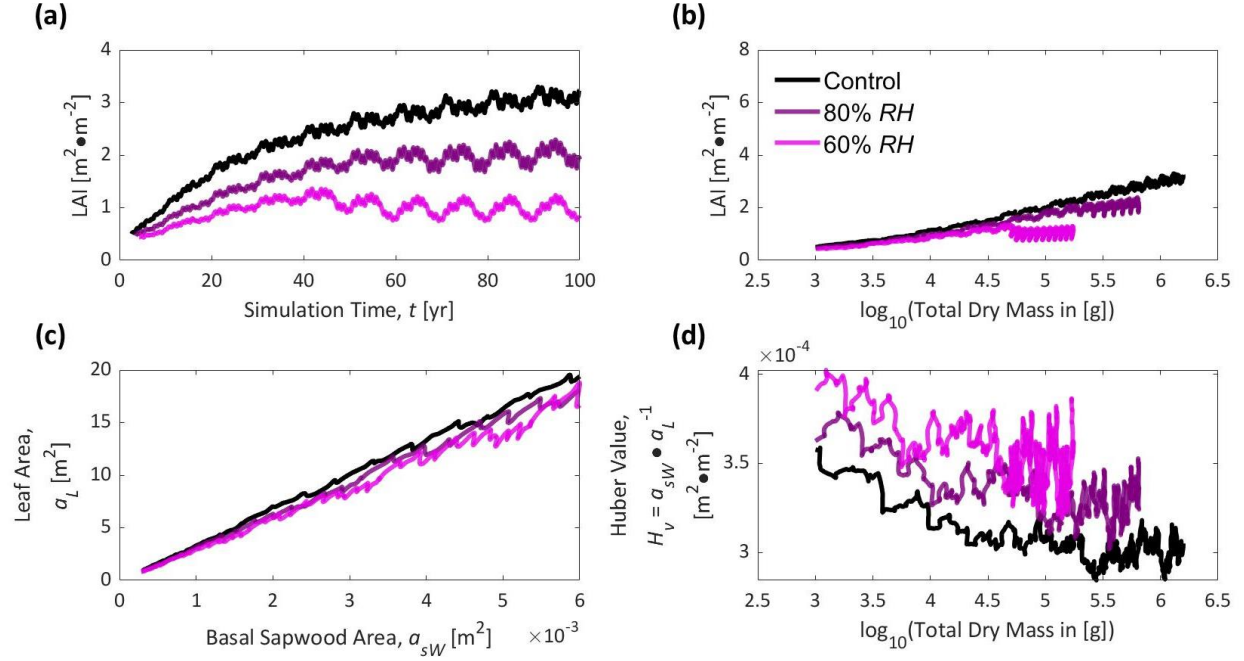


Figure S5: THORP predictions of leaf relations for 100-year Control experiment (black line) and experiments with reduced relative humidity (80% and 60% of Control; dark- and light-purple lines, respectively). Leaf area index ($a_L \cdot \varphi^{-1} \cdot W^{-2}$) versus time (a) and size, expressed as total dry mass (b). (c) Relationship between basal sapwood and total leaf areas. (d) Huber value (sapwood-to-leaf area ratio; $a_{sW}:a_L$) versus tree-size. In (c), the limits of the axes were constrained to the period before desiccation of the soil column (similar to the experiments with reduced precipitation as discussed in the main text) to clarify the response to drier air.

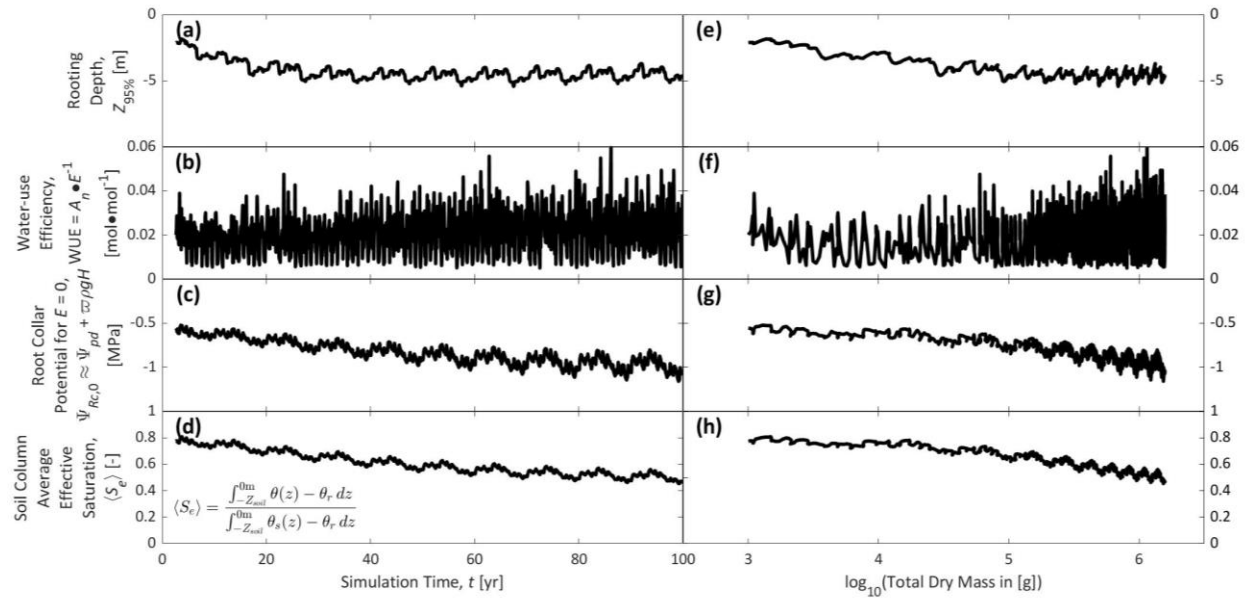


Figure S6: THORP's predictions of rooting depth and various indices of water-stress in an experiment with full precipitation and a free drainage bottom soil column boundary conditions (i.e. the control experiment). Rooting depth to 95% of root biomass, $Z_{95\%}$ (a,e), water-use efficiency, WUE (b,f), the hypothetical root collar water potential expected if there were no transpiration during midday, $\Psi_{Rc,0}$ (Eq. S.3.27), which may be interpreted as the predawn leaf water potential, Ψ_{pd} , normalized to ignore the increasing hydraulic limitations of height experienced during the simulation, $\varrho \rho g H$, to reflect primarily root-soil interactions (c,g), and the average effective saturation of the simulated soil column, $\langle S_e \rangle$ (analogous to Eq. S.2.6), over the thickness of the soil column, Z_{soil} (d,h) against simulation time, t (a-d), and total dry biomass (e-h). All values were averaged over a monthly time-step to clarify trends.

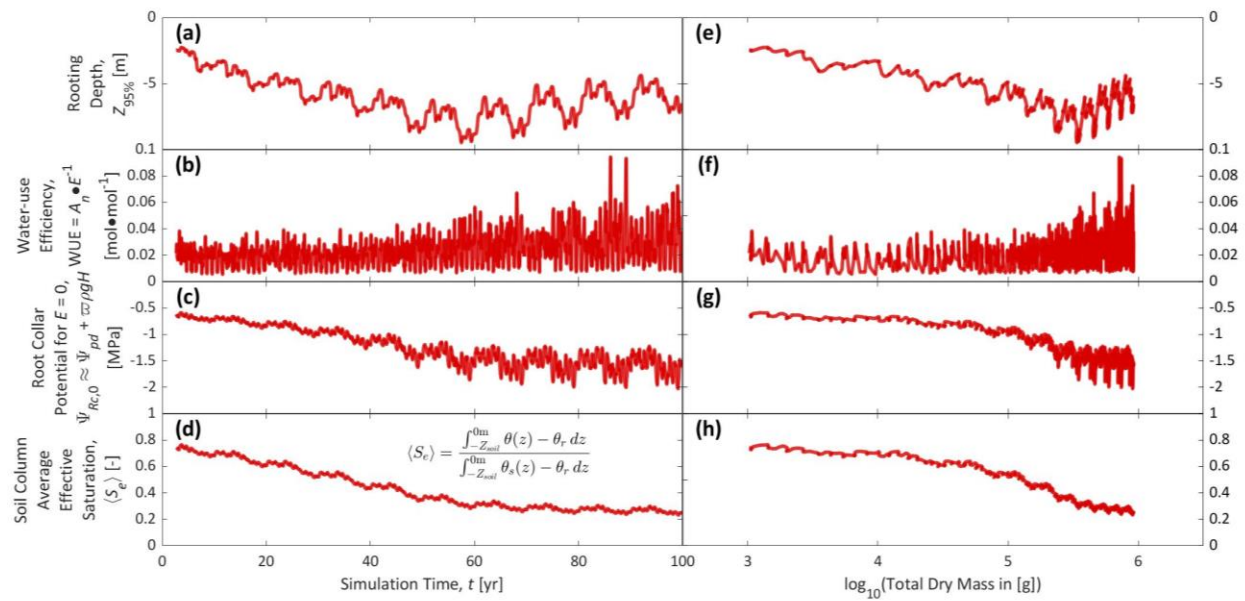


Figure S7: THORP's predictions of rooting depth and various indices of water-stress in an experiment with reduced precipitation (75% of control) and a free drainage bottom soil column boundary conditions. Rooting depth to 95% of root biomass, $Z_{95\%}$ (a,e), water-use efficiency, WUE (b,f), the hypothetical root collar water potential expected if there were no transpiration during midday, $\Psi_{Rc,0}$ (Eq. S.3.27), which may be interpreted as the predawn leaf water potential, Ψ_{pd} , normalized to ignore the increasing hydraulic limitations of height experienced during the simulation, $\varpi \rho g H$, to reflect primarily root-soil interactions (c,g), and the average effective saturation of the simulated soil column, $\langle S_e \rangle$ (analogous to Eq. S.2.6), over the thickness of the soil column, Z_{soil} (d,h) against simulation time, t (a-d), and total dry biomass (e-h). All values were averaged over monthly time-steps to clarify trends.

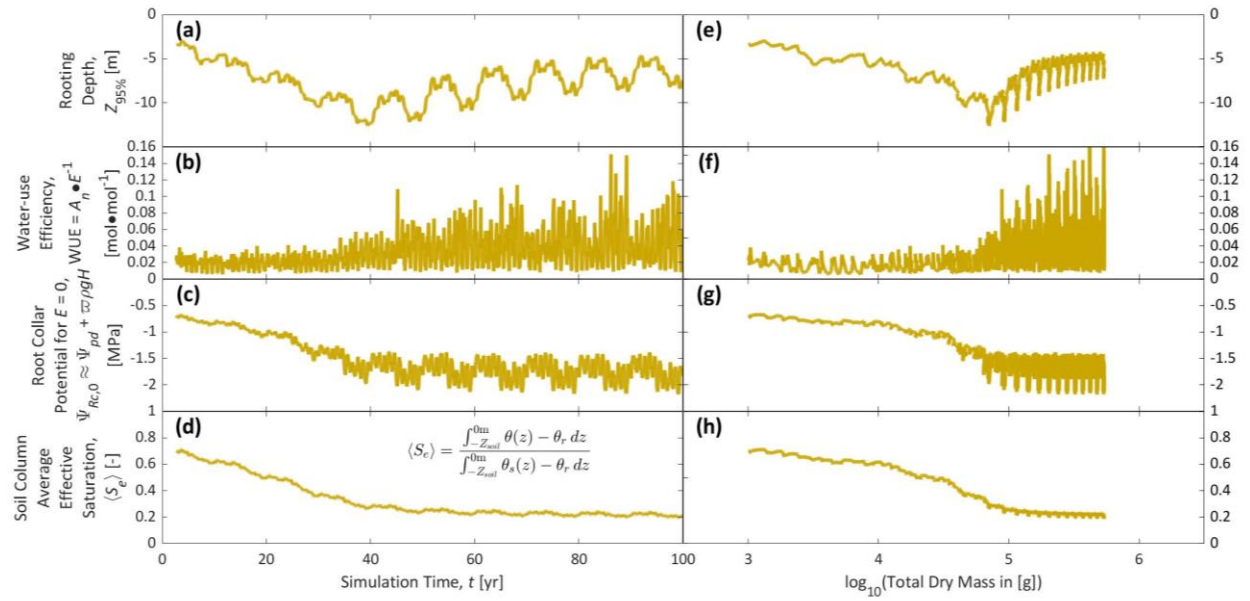


Figure S8: THORP's predictions of rooting depth and various indices of water-stress in an experiment with further reduced precipitation (50% of control) and a free drainage bottom soil column boundary conditions. Rooting depth to 95% of root biomass, $Z_{95\%}$ (a,e), water-use efficiency, WUE (b,f), the hypothetical root collar water potential expected if there were no transpiration during midday, $\Psi_{Rc,0}$ (Eq. S.3.27), which may be interpreted as the predawn leaf water potential, Ψ_{pd} , normalized to ignore the increasing hydraulic limitations of height experienced during the simulation, $\varpi \rho g H$, to reflect primarily root-soil interactions (c,g), and the average effective saturation of the simulated soil column, $\langle S_e \rangle$ (analogous to Eq. S.2.6), over the thickness of the soil column, Z_{soil} (d,h) against simulation time, t (a-d), and total dry biomass (e-h). All values were averaged over monthly time-steps to clarify trends.

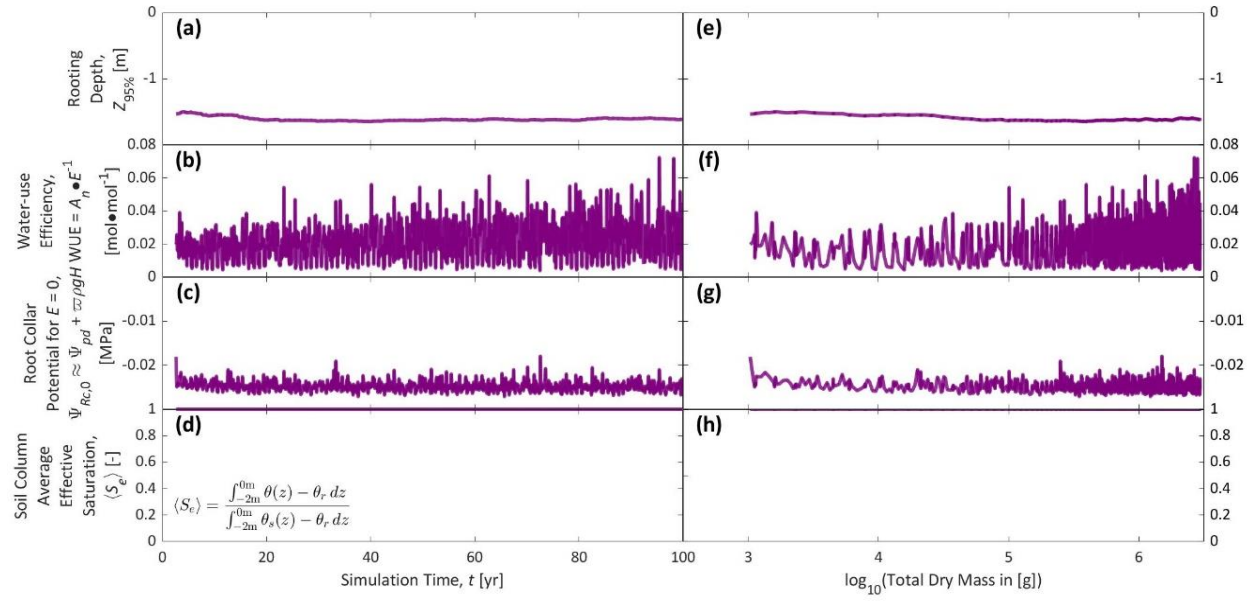


Figure S9: THORP's predictions of rooting depth and various indices of water-stress in an experiment with further reduced precipitation (50% of control) and a groundwater boundary condition at a depth of 2 m. Rooting depth to 95% of root biomass, $Z_{95\%}$ (a,e), water-use efficiency, WUE (b,f), the hypothetical root collar water potential expected if there were no transpiration during midday, $\Psi_{Rc,0}$ (Eq. S.3.27), which may be interpreted as the predawn leaf water potential, Ψ_{pd} , normalized to ignore the increasing hydraulic limitations of height experienced during the simulation, $\alpha \rho g H$, to reflect primarily root-soil interactions (c,g), and the average effective saturation of the simulated soil column, $\langle S_e \rangle$ (analogous to Eq. S.2.6), over the depth of the unsaturated zone where root growth occurred (Figure 5c) (d,h) against simulation time, t (a-d), and total dry biomass (e-h). All values were averaged over monthly time-steps to clarify trends.

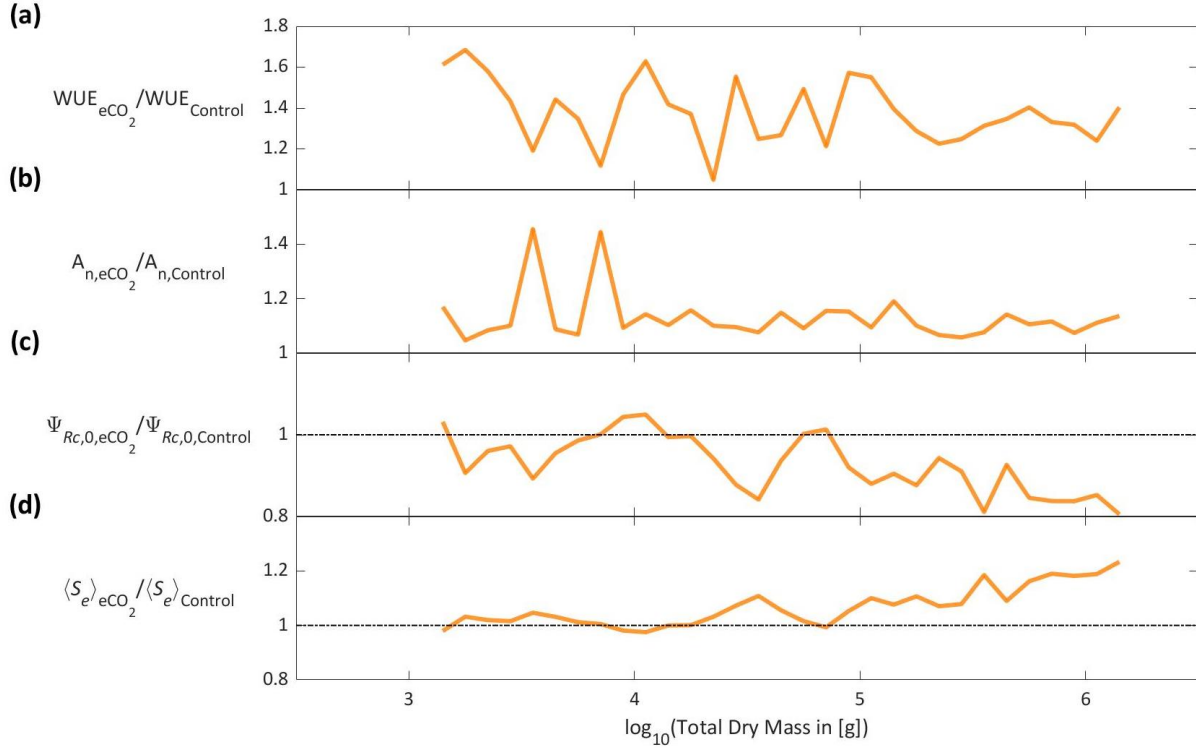


Figure S10: Indices of water-stress and productivity from experiment with elevated atmospheric CO_2 concentrations (eCO_2) relative to control values. Water-use efficiency, WUE (a), Leaf area-specific net carbon assimilation rate, A_n (b), the hypothetical root collar water potential expected if there were no transpiration during midday, $\Psi_{Rc,0}$ (Eq. S.3.27), which may be interpreted as the predawn leaf water potential, Ψ_{pd} , normalized to ignore the increasing hydraulic limitations of height experienced during the simulation, $\sigma \rho g H$, to reflect primarily root-soil interactions (c), and the average effective saturation of the simulated soil column, $\langle S_e \rangle$ (analogous to Eq. S.2.6), over the thickness of the soil column (d) against total dry biomass. All values were binned into logarithmically-spaced biomass pools ($[10^{3.0}, 10^{3.1}]$, $[10^{3.1}, 10^{3.2}]$, $[10^{3.2}, 10^{3.3}]$, etc.) and averaged to clarify trends. Note that WUE is a proxy for $\lambda = \partial A_n / \partial E$ by Buckley et al. (2017; Eq. S.6.12).

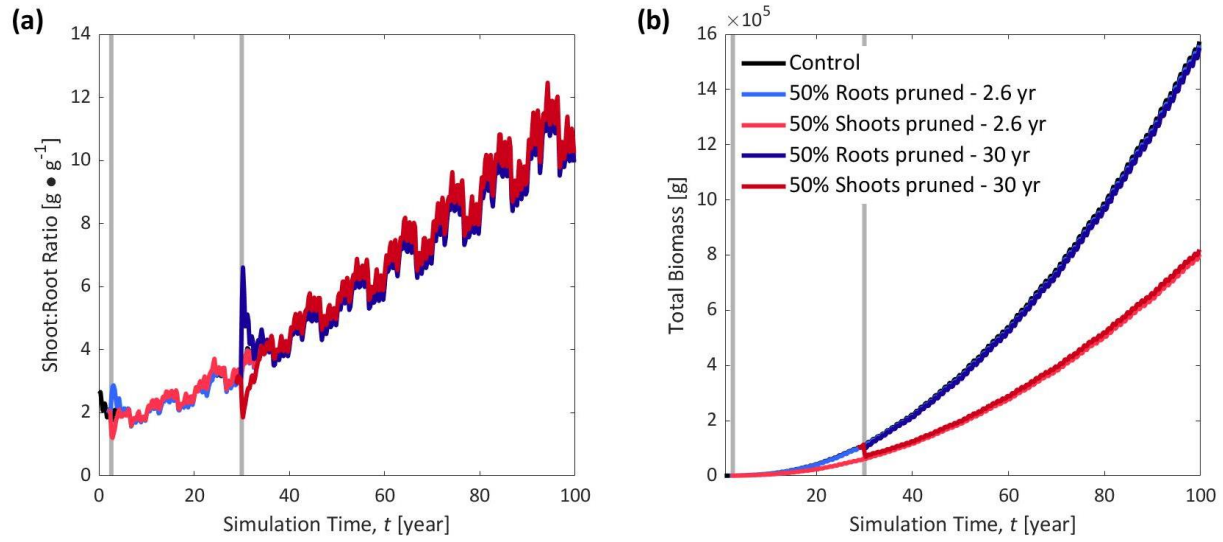


Figure S11: Time-series of THORP predictions with root or shoot pruning at ~2.6 and 30 years into simulation. (a) Shoot-root biomass ratio and (b) Total biomass plotted as function of simulation time. Total biomasses of both aboveground pruning experiments (2.6- and 30-year) overlap with the Control experiment in (b). Vertical, gray bars indicate timing of pruning. Values were averaged over annual time-steps to clarify trends.

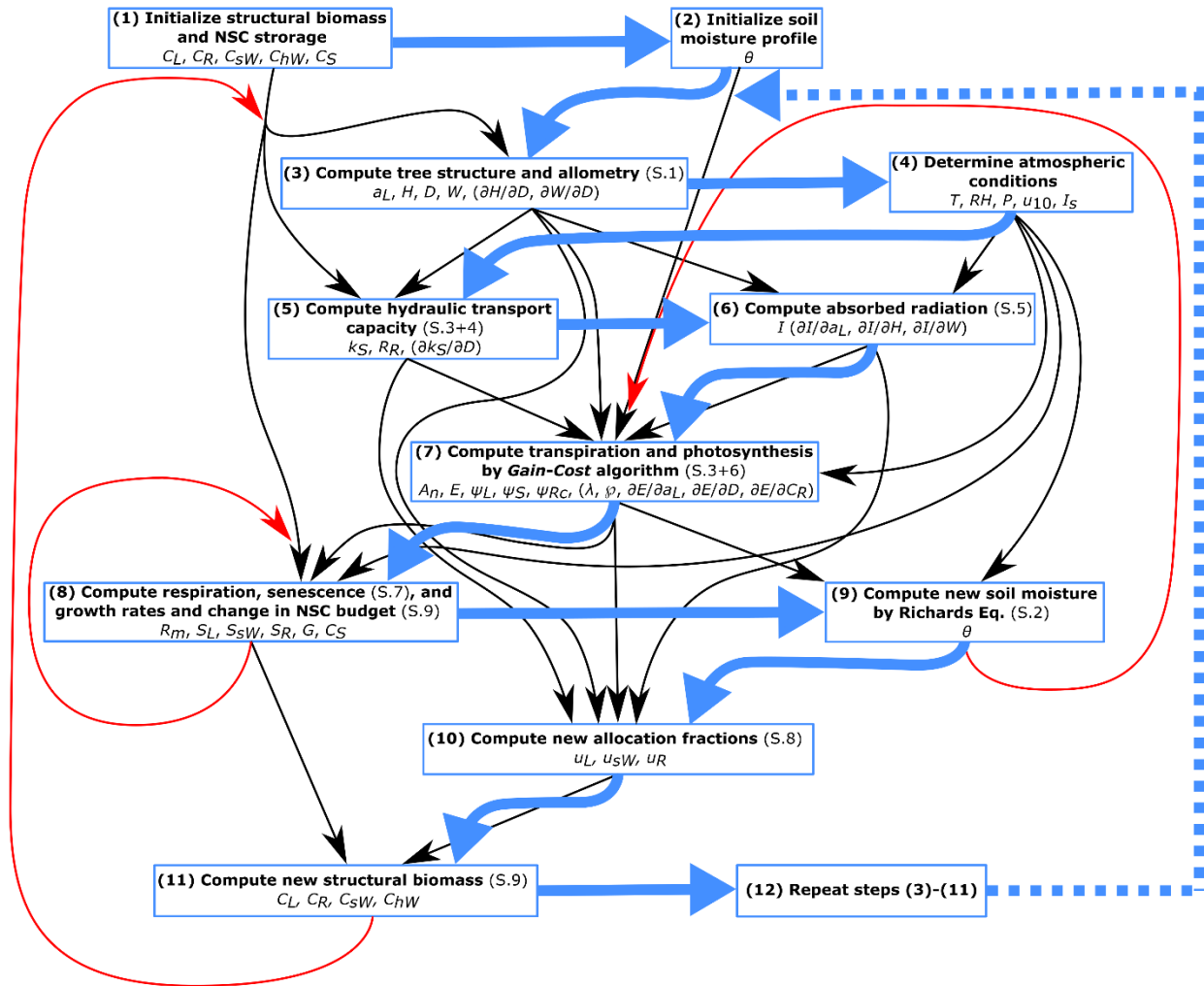


Figure S12: Flowchart of model computations and their relevant variables and sections in this supplementary information file (e.g. S.1-9). Variables in parentheses are terms used in step (10) to calculate optimal allocation fractions. See Table S1 for definition of variables. Blue arrows show the sequential order of steps while thin, black and red lines demonstrate the passing of variables between modules. Thin, black lines represent the passing of variables within a time-step, and thin, red lines represent the passing of variables between successive time-steps.

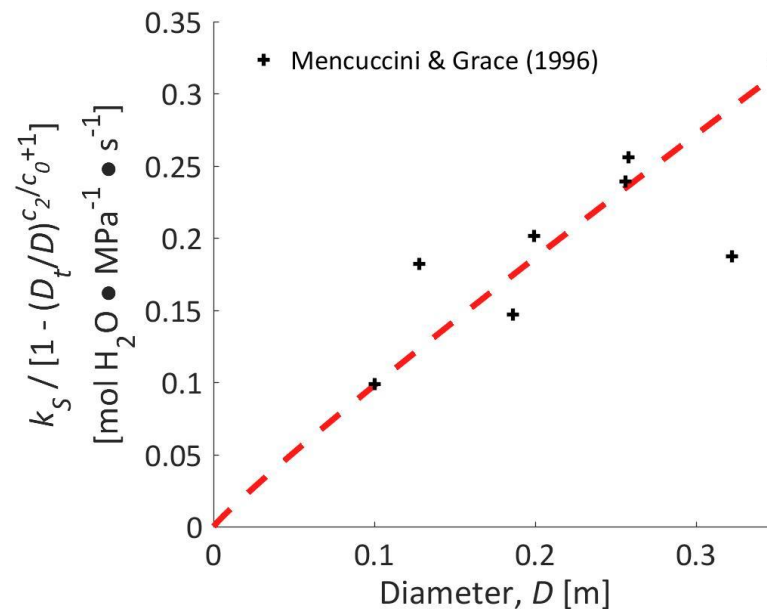


Figure S13: Comparison of stem hydraulic conductances from Mencuccini and Grace (1996) (black crosses) and fit to Eq. S.4.7 (red-dashed line) as function of basal diameter, D . The Y -axis represents the maximum stem conductance expected if no heartwood were present (i.e. $D_t = 0$ m).

Table S1: Main variables in THORP.

Symbo l	Units	Variable
<i>Constants</i>		
R	$[\text{J} \cdot \text{mol}^{-1} \cdot \text{K}^{-1}]$	Universal gas constant ($R = 8.314 \text{ J} \cdot \text{mol}^{-1} \cdot \text{K}^{-1}$)
g	$[\text{m} \cdot \text{s}^{-2}]$	Acceleration due to gravity ($g = 9.81 \text{ m} \cdot \text{s}^{-2}$)
ρ	$[\text{kg} \cdot \text{m}^{-3}]$	Density of water ($\rho = 10^3 \text{ kg} \cdot \text{m}^{-3}$)
m_w	$[\text{kg} \cdot (\text{mol H}_2\text{O})^{-1}]$	Molar mass of water ($m_w = 1.8 \cdot 10^{-2} \text{ kg} \cdot (\text{mol H}_2\text{O})^{-1}$)
ϖ	$[\text{MPa} \cdot \text{Pa}^{-1}]$	Conversion factor from pascals to megapascals ($\varpi = 10^{-6} \text{ MPa} \cdot \text{Pa}^{-1}$)
<i>Environmental Conditions</i>		
c_a	$[\text{kPa}]$	Atmospheric CO_2 concentration
o_a	$[\text{kPa}]$	Atmospheric O_2 concentration
RH	$[-]$	Relative humidity of air
T_a	$[\text{K}]$	Air temperature
T_{soil}	$[\text{K}]$	Soil temperature
P	$[\text{m} \cdot \text{s}^{-1}]$	Precipitation
u_{10}	$[\text{m} \cdot \text{s}^{-1}]$	Windspeed at 10 m elevation
I_s	$[\text{W} \cdot \text{m}^{-2}]$	Incoming solar insolation
Φ	$[-]$	Solar elevation below the zenith in radians
H_n	$[\text{m}]$	Height of neighboring upper canopy
<i>Structural Metrics</i>		
a_L	$[\text{m}^2]$	Leaf area
D	$[\text{m}]$	Basal trunk diameter
D_t	$[\text{m}]$	Diameter of heartwood-sapwood transition
H	$[\text{m}]$	Height
W	$[\text{m}]$	Canopy width
Z	$[\text{m}]$	Rooting depth
LAI	$[-]$	Leaf Area Index (here calculated as $a_L \cdot \varphi^{-1} \cdot W^{-2}$)
<i>Carbon Pools</i>		
C_L	$[\text{mol C}]$	Leaf carbon pool
C_R	$[\text{mol C}]$	Total root carbon pool ($C_R = C_{R,H} + C_{R,V}$)
$C_{R,H}$	$[\text{mol C}]$	Root carbon pool that governs the horizontal (intralayer) portion of root resistance, $R_{R,H}$
$C_{R,V}$	$[\text{mol C}]$	Root carbon pool that governs the vertical (interlayer) portion of root resistance, $R_{R,V}$
C_W	$[\text{mol C}]$	Total aboveground wood carbon (stem) pool ($C_W = C_{sW} + C_{hW}$)
C_{sW}	$[\text{mol C}]$	Sapwood carbon pool
C_{hW}	$[\text{mol C}]$	Heartwood carbon pool
C_S	$[\text{mol C}]$	Nonstructural Carbohydrate (NSC) Storage carbon pool
<i>Respiration, Senescence, and Growth</i>		

R_m	[mol C · s ⁻¹]	Total maintenance respiration
r_R^m	[s ⁻¹]	Carbon pool-specific root maintenance respiration rate ^{1,2}
r_{sW}^m	[s ⁻¹]	Carbon pool-specific sapwood maintenance respiration rate ^{1,3}
S_L	[mol C · s ⁻¹]	Leaf senescence rate
$S_{R,i}$	[mol C · s ⁻¹]	Root senescence rate of <i>i</i> th soil layer
S_{sW}	[mol C · s ⁻¹]	Sapwood senescence rate
G	[mol C · s ⁻¹]	Total (above- and below-ground) growth rate
u_L	[-]	Fraction of G allocated to leaf pool
$u_{R,i}$	[-]	Fraction of G allocated to <i>i</i> th soil layer's root pool
u_{sW}	[-]	Fraction of G allocated to stem (sapwood) pool
Soil Hydraulics		
$\Psi_{soil,i}$	[MPa]	Soil water potential of <i>i</i> th soil layer
$\theta_{s,i}$	[-]	Saturated (maximum) volumetric soil water content of <i>i</i> th soil layer
C_i	[MPa ⁻¹]	Hydraulic capacitance of <i>i</i> th soil layer
$K_{soil,i}$	[m · s ⁻¹]	Hydraulic conductivity of <i>i</i> th soil layer
$K_{soil,sat,i}$	[m · s ⁻¹]	Saturated hydraulic conductivity of <i>i</i> th soil layer
q	[m · s ⁻¹]	Darcy water flux
f_i	[s ⁻¹]	Soil moisture sink term for <i>i</i> th soil layer
Δz_i	[m]	Layer vertical thickness of <i>i</i> th soil layer
z_i	[m]	Depth to center of <i>i</i> th soil layer
E_{soil}	[m · s ⁻¹]	Soil evaporation from ground surface
g_a	[mol H ₂ O · m ⁻² · s ⁻¹]	Air conductivity to vapor transport at soil surface
$e_{soil,sat}$	[kPa]	Saturated vapor pressure of soil surface
$e_{a,sat}$	[kPa]	Saturated vapor pressure of air
e_{soil}	[kPa]	Vapor pressure of soil surface
e_a	[kPa]	Vapor pressure of air
RH_{soil}	[-]	Relative humidity of soil surface
Xylem Hydraulics		
E	[mol H ₂ O · m ⁻² · s ⁻¹]	Leaf area-specific transpiration rate
k_S	[mol H ₂ O · s ⁻¹ · MPa ⁻¹]	Maximum stem (root collar to stem apex) xylem conductance
Ψ_L	[MPa]	Leaf xylem water potential
Ψ_S	[MPa]	Stem xylem water potential
Ψ_{Rc}	[MPa]	Root collar xylem water potential
f_L	[-]	Factor that represents the magnitude of embolism in leaves
f_S	[-]	Factor that represents the magnitude of embolism in stem
f_R	[-]	Factor that represents the magnitude of conductance-loss in roots
$R_{R,i}$	[MPa · s · (mol H ₂ O) ⁻¹]	Root resistance to soil water-uptake of <i>i</i> th soil layer
$R_{R,H,i}$	[MPa · s · (mol H ₂ O) ⁻¹]	Horizontal (intralayer) portion of root resistance of <i>i</i> th soil layer
$R_{R,V,i}$	[MPa · s · (mol H ₂ O) ⁻¹]	Vertical (interlayer) portion of root resistance of <i>i</i> th soil layer

<i>Photosynthesis</i>		
T_L	[K]	Leaf temperature
I	$[\text{W} \cdot \text{m}^{-2}]$	Leaf area-specific intercepted insolation
A_n	$[\text{mol C} \cdot \text{m}^{-2} \cdot \text{s}^{-1}]$	Leaf area-specific net carbon assimilation (photosynthesis) rate
A_j	$[\text{mol C} \cdot \text{m}^{-2} \cdot \text{s}^{-1}]$	Electron transport-limited leaf area-specific gross photosynthesis rate
J	$[\text{mol C} \cdot \text{m}^{-2} \cdot \text{s}^{-1}]$	Actual rate of electron transport
J_l	$[\text{mol C} \cdot \text{m}^{-2} \cdot \text{s}^{-1}]$	Light-limited rate of electron transport
J_{max}	$[\text{mol C} \cdot \text{m}^{-2} \cdot \text{s}^{-1}]$	Maximum rate of electron transport ⁴
A_c	$[\text{mol C} \cdot \text{m}^{-2} \cdot \text{s}^{-1}]$	Carboxylation-limited leaf area-specific gross photosynthesis rate
$V_{c,max}$	$[\text{mol C} \cdot \text{m}^{-2} \cdot \text{s}^{-1}]$	Maximum carboxylation rate ⁴
R_d	$[\text{mol C} \cdot \text{m}^{-2} \cdot \text{s}^{-1}]$	Leaf area-specific dark respiration rate ⁵
G_c	$[\text{mol C} \cdot \text{m}^{-2} \cdot \text{s}^{-1} \cdot \text{kPa}^{-1}]$	Stomatal conductance to CO ₂
G_w	$[\text{mol H}_2\text{O} \cdot \text{m}^{-2} \cdot \text{s}^{-1} \cdot \text{kPa}^{-1}]$	Stomatal conductance to H ₂ O
c_i	[kPa]	Leaf internal CO ₂ concentration
Γ^*	[kPa]	CO ₂ compensation point
K_c	[kPa]	Michaelis–Menten constant for carboxylation
K_o	[kPa]	Michaelis–Menten constant for oxygenation
λ	$[\text{mol C} \cdot (\text{mol H}_2\text{O})^{-1}]$	Marginal water-use efficiency, $\lambda = \partial A_n / \partial E = (\partial A_n / \partial \Psi_L) / (\partial E / \partial \Psi_L)$
\wp	$[\text{mol C} \cdot \text{J}^{-1}]$	Marginal light-use efficiency, $\wp = \partial A_n / \partial I$

¹Temperature-dependent following Q₁₀ relationship

²Q₁₀ = 1.98 for root maintenance respiration of Scots Pine (Marshall & Waring, 1985; Janssens et al., 1999)

³Q₁₀ = 1.80 for sapwood maintenance respiration of Scots Pine (Zha et al., 2004)

⁴Leaf temperature-dependent following Harley and Baldocchi (1995)

⁵Leaf temperature-dependence of R_d is captured through its proportionality with $V_{c,max}$ according to de Pury and Farquhar (1997; $R_d = 0.01 \cdot V_{c,max}$)

Notes S1 – Full model description and simulations

FULL MODEL DESCRIPTION

This appendix describes the THORP (Tree Hydraulics and Optimal Resource Partitioning) model. Symbols and units are summarized in Table S1, and the order of model computations are summarized as a flowchart in Figure S12. In this study, the control simulation was run for a total of 100 years at 6-hour time-steps ($\Delta t = 21600$ s), based on the resolution of NOAA re-analysis data that was used as atmospheric boundary conditions (NCEP/NCAR Reanalysis 1; Kalnay et al., 1996), which are air and soil temperatures, T_a and T_{soil} [K], respectively, relative humidity of the air, RH [-], precipitation rates, P [$\text{m}\cdot\text{s}^{-1}$], windspeeds at 10 m elevation, u_{10} [$\text{m}\cdot\text{s}^{-1}$], and incoming solar insolation, I_s [$\text{W}\cdot\text{m}^{-2}$]. Additional simulations were run for a minimum for 100 years. When trees grew slowly due to resource limitations, simulation were extended until achieving a total tree dry biomass similar to the end of the control simulation (10^6 g of total dry, structural biomass).

THORP predicts the dynamic allocation fractions to each carbon pool (leaves, aboveground woody biomass, and roots within each soil layer) that maximize net assimilation by estimating the allocation fraction to an organ as proportional to its ratio of marginal carbon gain to marginal cost, where the gain is the net canopy photosynthesis rate, and the cost is senescence rates (Eq. 1 in main text). We first describe how THORP models processes affecting the marginal carbon gain and cost terms including allometric and structural relationships (Section S.1), soil water availability (S.2), transpiration (S.3), conductances throughout the tree (S.3-4), light interception (S.5), and photosynthesis, respiration, and senescence rates (S.6-7). Then we describe biomass partitioning (S.8) and lastly growth and carbohydrate storage dynamics (S.9). Lastly, we explain in detail the initialization and parameterization of physiological and environmental parameters and conditions that we applied in the control and other experiments (S.10).

We note that THORP represents key plant mechanisms but ignores others which may serve as secondary drivers of allocation response. Among those, four notable mechanisms are (1) delayed xylem refilling or lack of recovery due to permanent xylem damage, (2) plant water storage, (3) nutrient uptake and partitioning, and (4) osmoregulation, which is regulated by starch-sugar metabolism (Martínez-Vilalta et al., 2016) and phloem-transport (Lacointe & Minchin, 2008; De Schepper & Steppe, 2010), and which may be linked to growth rates through osmolyte-generated turgor and turgor-driven growth (Lockhart, 1965). Here, we address how these mechanisms would affect THORP's predictions:

- (1) THORP currently assumes that xylem refill immediately when water potentials become less-negative and that they refill back to the most possibly conductive for the new water potential (i.e. from the virgin vulnerability curve). This is not realistic; however, many aspects of xylem refilling mechanisms and temporal dynamics remain unanswered. A common approach is to test two end-members by modeling xylem twice, once as refilling immediately and again as never refilling, and then comparing the two results (Venturas et al., 2018). Mackay et al. (2015) have already simulated the progressive hydraulic impairment of xylem associated with delayed refilling. Mackay et al. (2015) and Venturas et al. (2018) considered solely embolism and did not consider the growth of new, fully-functional xylem. However, this approach would be more complicated in THORP which simulates stem growth (and the resulting increase in hydraulic conductance by the construction of new xylem) and thus would potentially require tracking and quantifying the degree of embolism in each stem increment. This tracking may be computationally overwhelming when performed at THORP's short time-step of 6 hours.

Additionally, performing Sperry et al.'s (2017) *Gain-Risk* algorithm for a delayed-refilling case would require solving the algorithm twice (once to solve for the optimal leaf water potential, Ψ_L , using the virgin vulnerability curve, and a second time in search of the stomatal conductance that coincides with the same Ψ_L , except using the nonvirgin vulnerability curve; see methodology in Venturas et al. 2018) and would further burden computation. Nevertheless, THORP's predictions would change if we included delayed refilling or permanent damage. In this hypothetical case, the lower hydraulic conductance (due to longer-lasting embolism or xylem occlusions) would trigger two coinciding events. The lower hydraulic conductance would require a steeper hydraulic gradient and thus more-negative xylem potentials to maintain transpiration (Sperry & Love, 2015; Sperry et al., 2016). Additionally, the lower conductance would lead to stomatal closure (Sperry et al., 2017), which could cause the marginal water-use, λ , to increase (Mäkelä et al., 1996; Manzoni et al., 2011). Both events (the increase in the hydraulic gradient and the increase in λ) would alter *marginal gain* terms for leaves, stems, and roots (through Eq. S.3.56-57, Eq. S.3.59, and Eq. S.8.6-8), and THORP would allocate more growth to stems and roots and less to leaves. These changes in stem and root allocation would only magnify the responses that THORP already predicts under water-stress and would only affect THORP's predictions quantitatively, but not qualitatively. Future versions of THORP may describe delayed refilling.

- (2) THORP ignores plant water storage, since our representation of xylem hydraulics is largely based on Sperry et al. (1998; which included hydraulic capacitance, but it was set to zero), and since no previous tests of the *Gain-Risk* algorithm have included plant water storage (Venturas et al., 2018; Wang et al., 2019). We expect that if we included plant water storage, then THORP would allocate less to stems and roots, however only transiently, since hydraulic capacitance would buffer against water-stress, and delay stomatal closure (and thus delay embolism and the increases in hydraulic gradient and λ). Water storage's effect on allocation would oppose that of delayed xylem refilling as long as the duration of drought was shorter than that of the alleviation provided by storage. Future versions of THORP may include water storage.
- (3) THORP currently assumes that nutrients are neither limiting nor alter the optimal path for allocation (which is the common framework for many past optimality models; e.g. Franklin, 2007; Mäkelä et al., 2008; McMurtrie et al., 2008). Consequently, we do not explicitly simulate nutrient uptake and partitioning. Instead, it is assumed that nutrient uptake at least equals demand and that nutrient concentrations of biomass are fixed (though never defined). However, we can already imagine at least two cases in which nutrients should matter, but THORP would not correctly respond. First, the model would capture neither reduced growth rates (LeBauer & Treseder, 2008; Li et al., 2018) nor increased root allocation (Poorter & Nagel, 2000) during periods of limited nutrient access. Second, THORP cannot currently capture any changes in the photosynthetic apparatus ($V_{c,max}$ and J_{max}) that may result from environmental change and which would alter THORP's predictions of photosynthesis, hydraulics, and allocation. Such changes in photosynthesis are often related to leaf nitrogen content (Field & Mooney, 1986; Evans, 1989), which varies plastically (Luo et al., 2006), and changes are theorized to occur during CO₂ enrichment (Franklin, 2007; Mäkelä et al., 2008; McMurtrie et al., 2008) to optimize productivity, even according to theory that focuses on plant hydraulics (Sperry et al., 2017, 2019). Modeling dynamic, optimal nitrogen allocation is possible (Caldararu et al., 2020) and may improve THORP's predictions under light limitation (partially through coinciding changes in specific leaf area; Meir et al. 2002), and offer insight into the roles of nutrient limitations during

Free Air CO₂ Enrichment (FACE) experiments. Future versions of THORP may include nitrogen dynamics.

- (4) A mechanistic representation of osmoregulation (and its links to nonstructural carbohydrate (NSC) metabolism and phloem transport) would have no effect on THORP's predictions of the allocation fractions (u_L , u_{sw} , u_{RH} , u_{RV}) at least for the same physiological and environmental conditions. We imagine that modeling osmoregulation would be part of a broader representation of NSC dynamics including sugar-starch metabolism (Lacointe & Minchin, 2008; Schiestl-Aalto et al., 2019), phloem transport (Thompson & Holbrook, 2003; Hölttä et al., 2006, 2009), and turgor-driven growth (Lockhart, 1965; Steppe et al., 2006; Hölttä et al., 2010; Coussement et al., 2018; Cabon et al., 2020a,b). This phloem-growth module would ultimately inform THORP how to mechanistically predict NSC-storage-growth relations, especially the whole-tree growth rate, G , and the module would replace THORP's current, simple NSC dynamics presented here (Eq. S.9.1-2). This approach would offer a mechanistic means of estimating G and its dependence on tree size and environmental conditions through their effects on turgor, phloem transport, and sink demand. These mechanisms are currently and crudely imitated by formulating G as a function of NSC storage and temperature (Eq. S.9.2). Though the phloem-growth module would cause little-to-no change in THORP's predicted allocation fractions, it would nonetheless affect the predicted allometry, since allometry is the time-integral of the product of allocation fraction (u_L , u_{sw} , u_{RH} , u_{RV}) and growth rate (G) minus the relevant senescence (Eq. S.9.3-5). Consequently, the allometry would better reflect a physiology better adapted to more favorable (wetter, warmer) conditions, during which higher growth rates, G , would occur (assuming that allocation fractions react to environmental conditions instantaneously or at time-scales shorter than those over which growth rates react). We recognize that the resulting different growth rates, G , would alter the existing physiology (e.g. size) for a given age and thus alter the allocation fractions, which are based on different size-mediated allocation demands. However, our simulations suggest that there is an optimal allocation path independent of growth rate when environmental conditions are reasonably static. In conclusion, phloem-growth considerations should cause THORP's predicted allometry to better optimized for the favorable conditions of a highly seasonal environment, and their influence will become increasingly muted as seasonality diminishes and as environmental conditions become more static. Though not currently mechanistically predicted, this trend for the allometry to best adapted to the growing season rather than other times of the year is produced by the temperature- and NSC-dependence in Eq. S.9.2. A future version of THORP with such a phloem-growth module is currently being designed by the first author.

S.1 Allometric Scaling and Structural Metrics

Tree structure in THORP, particularly that describing aboveground organs, is largely based on Buckley and Roberts (2006a,b), except we constrain tree height, H [m], basal diameter, D [m], and canopy width, W [m], by power-law scaling functions (West et al., 2009). Belowground organs are not given an explicit physical representation (e.g. specific root length, root area, etc.) besides the size of the root carbon pool in each soil layer, which characterizes the potential for root-water uptake (see Section S.3). The simulated tree is represented by two aboveground carbon pools: leaf and wood carbon pools, C_L and C_W [mol C], respectively. The latter is the sum of a hydraulically-conductive and respiring sapwood pool, C_{sw} [mol C], and nonconductive and non-respiring heartwood pool, C_{hw} [mol C] ($C_W = C_{sw} + C_{hw}$). THORP includes multiple total root carbon pools with the number of pools based on the number of soil

layers. The root carbon pool of an individual soil layer is denoted by $C_{R,i}$ [mol C], where the subscript i signifies the index of the soil layer. Each soil layer contains two distinct root pools: (1) a pool responsible for conducting water within the soil layer ‘horizontally’, $C_{R,H,i}$, and (2) a pool responsible for conducting water among the soil layers ‘vertically’ towards the aboveground portion of the tree, $C_{R,V,i}$. The total, integrated root carbon pool, C_R [mol C] is the sum of all of the tree’s individual root carbon pools ($C_R = \sum C_{R,i} = \sum (C_{R,H,i} + C_{R,V,i})$ for all soil layers, i). Physically, vertical root pools represent solely transporting roots (i.e. xylem) and may be interpreted as a taproot. Horizontal root pools represent both absorbing roots (i.e. fine-roots) and the xylem pathway between absorption and the nearest segment of taproot.

It is notable that the model includes multiple root and soil layers (i.e. multiple $C_{R,i}$), but not canopy layers (i.e. single C_L). This representation was chosen for simplicity and to ease potential implementation in large scale land surface models. Regardless of the representation of vegetation, land surface models already discretize soil columns into multiple layers to solve the soil-water balance by Richards equation through finite-difference (as done here; section S.2). In their vegetation schemes, these models already contain multiple root pools distributed in depth (though often through a fixed, parameterized exponential decline in root biomass with depth; e.g. Oleson et al., 2010, 2013; Lawrence et al., 2019; Shao et al., 2019). Multiple soil and root pools are necessary to differentiate shallow soil moisture from deeper water reserves and thus also to predict vegetation’s dependence on deep soil moisture and groundwater. We expect these deeper reserves to become more important under drought (e.g. Mackay et al., 2020; McLaughlin et al., 2020). Detailed physiological modeling of canopies suggests that plant optimization methods are sensitive to the level of detail in interception models (e.g. Buckley et al., 2002) and thus should depend on canopy layering. Here, we have applied a simple representation of light interception with a single canopy layer (section S.5), since little evidence from comparisons of large-scale vegetation models suggest that multilayered canopy models perform better than single layered canopy schemes in land surface models (e.g. Walker et al., 2014). The model can be adapted for a multilayer canopy scheme in future versions.

The relevant tree dimensions are total canopy leaf area, a_L [m²], height, H [m], canopy width, W [m], basal diameter, D [m], and the diameter of the heartwood-sapwood transition, D_t [m]. Leaf area is the product of the leaf carbon pool and the specific leaf area (SLA), X_L [m² · (mol C)⁻¹] ($a_L = X_L \cdot C_L$). Wood carbon-volume relations in THORP are similar to those used by Buckley and Roberts (2006a,b) and Mäkelä (1986).

$$C_W = \rho_{CS} \xi H D^2 \quad (\text{S.1.1})$$

Both the empirical form factor, ξ [-], and the stem’s carbon density, ρ_{CS} [mol C · m⁻³] are assumed constant. This formulation of wood carbon does not explicitly represent canopy width; however, its contribution is here implicitly represented by the form factor, ξ . Assuming area-preserving branching (da Vinci’s rule; Horn, 2000; von Allmen et al., 2012) and that sapwood area is uniform along the water flow path of tree (Pipe model; Shinozaki et al., 1964), the form of Eq. S.1.1 may also describe heartwood carbon-volume relations ($C_{HW} = \rho_{CS} \xi H \cdot D_t^2$).

Tree height and canopy width, H and W , respectively, are power-law functions of basal diameter, D (West et al., 2009)

$$H = b_0 \left(\frac{D}{D_{ref}} \right)^{c_0} \quad (\text{S.1.2})$$

$$W = b_1 \left(\frac{D}{D_{ref}} \right)^{c_1} \quad (\text{S.1.3})$$

where b_0 and b_1 are scaling constants [m] ($H = b_0$ and $W = b_1$ when $D = D_{ref} = 1$ m), and c_0 and c_1 are scaling exponents [-]. After combining Eq. S.1.1 and S.1.2, wood carbon may be defined independently of H .

$$C_W = \rho_{CS} \xi b_0 D_{ref}^{-c_0} D^{2+c_0} \quad (S.1.4)$$

From Eq. S.1.2-4, the following derivatives may be defined which will be used later in Section S.3 and S.8 to calculate allocation fractions.

$$\frac{\partial H}{\partial D} = c_0 \frac{H}{D} \quad (S.1.5)$$

$$\frac{\partial W}{\partial D} = c_1 \frac{W}{D} \quad (S.1.6)$$

$$\frac{dD}{dC_W} = \frac{1}{2+c_0} \frac{D}{C_W} \quad (S.1.7)$$

By definition of a constant specific leaf area, $da_L/dC_L = X_L$.

S.2 Soil Hydrology

The soil column is discretized into multiple layers identified by index i . The index of the shallowest layer is $i = 1$, and deeper layers have larger indices. Each layer is defined by a depth to its midpoint, z_i (positive is down) [m], and a layer thickness, Δz_i [m]. Layer thicknesses increase as a geometric series such that the total soil depth, number of soil layers, N , and the thickness of the first layer are user-specified (default of 30 m, $N = 15$ layers, and 0.1 m respectively). When a groundwater table is introduced and the table's depth is deeper than the bottom of the initially parameterized soil column, then the soil column thickness is subsequently increased following the same geometric series as initially calculated (maintaining the same values of z_i for the first, original N layers) by determining a new value of N , for which the groundwater table depth is shallower than or equal in depth to the bottom of the soil column.

Soil moisture is modeled by the 1-D vertical form of Richards equation (Richardson, 1922; Richards, 1931), which may be expressed continuously as

$$\frac{\partial \theta}{\partial t} = C \frac{\partial \Psi_{soil}}{\partial t} = -\frac{\partial q}{\partial x} + f = \frac{\partial}{\partial x} \left[K_{soil} \left(\frac{1}{\omega \rho g} \frac{\partial \Psi_{soil}}{\partial x} + 1 \right) \right] + f \quad (S.2.1)$$

where t is time [s], x is the vertical Cartesian coordinate (positive is up) [m], q is the Darcy flux [$\text{m} \cdot \text{s}^{-1}$], θ is the volumetric water content [-], Ψ_{soil} is the matric soil water potential [MPa], $C = \partial \theta / \partial \Psi_{soil}$ is the soil's hydraulic capacitance [MPa^{-1}], K_{soil} is the hydraulic conductivity of soil [$\text{m} \cdot \text{s}^{-1}$], ω is a factor that converts from Pa to MPa ($\omega = 10^{-6} \text{ MPa} \cdot \text{Pa}^{-1}$), ρ is the density of water [$\text{kg} \cdot \text{m}^{-3}$], g is the acceleration due to gravity [$\text{m} \cdot \text{s}^{-2}$], and f is a source term that here describes the loss of soil water to transpiration [s^{-1}] (i.e. f is negative when root-water uptake occurs; however, f may be positive depending on the gradient of water potential between soil and root, enabling hydraulic redistribution). Roots conduct water from each soil layer in a manner analogous to an in-parallel resistor, and each layer contributes its portion of transpiration, E_i , to the total leaf-area specific transpiration, E [$\text{mol H}_2\text{O} \cdot \text{m}^{-2} \cdot \text{s}^{-1}$] (see section S.3 for modeling of transpiration) such that all contributions sum to the total.

$$E = \sum_{i=1}^N E_i \quad (S.2.2)$$

The discrete form of the sink term in the i th soil layer is

$$f_i = -\frac{m_w a_L E_i}{\rho \Delta z_i W^2} \quad (\text{S.2.3})$$

where m_w is the molar mass of water [$\text{kg} \cdot (\text{mol H}_2\text{O})^{-1}$], a_L is the total canopy leaf area [m^2], and W is the canopy width [m]. Lateral root extent is not explicitly represented in THORP, and consequently we approximate roots extent as equal to canopy width.

Hydraulic conductivity, K_{soil} , and water retention, which defines the hydraulic capacitance, $\partial\theta/\partial\Psi_{\text{soil}}$, are defined by van Genuchten's (1980) formulation

$$K_{\text{soil}} = K_{\text{soil,sat}} S_e^{0.5} \left[1 - \left(1 - S_e^{\frac{n_{VG}}{1-n_{VG}}} \right)^{1-\frac{1}{n_{VG}}} \right]^2 \quad (\text{S.2.4})$$

$$\theta = \theta_r + (\theta_s - \theta_r) S_e \quad (\text{S.2.5})$$

where $K_{\text{soil,sat}}$ is the saturated or maximum hydraulic conductance [$\text{m}\cdot\text{s}^{-1}$], n_{VG} is a shape parameter [-], α_{VG} is a scaling parameter [MPa^{-1}], θ_r is the residual or minimum volumetric water content [-], θ_s is the saturated or maximum volumetric water content [-], and S_e is the effective saturation [-] given by the following.

$$S_e = \begin{cases} [1 + (\alpha_{VG} |\Psi_{\text{soil}}|)^{n_{VG}}]^{-1+\frac{1}{n_{VG}}} & \Psi_{\text{soil}} \leq 0 \\ 1, & \Psi_{\text{soil}} > 0 \end{cases} \quad (\text{S.2.6})$$

In general, both the soil's saturated hydraulic conductivity, $K_{\text{soil,sat}}$, and porosity, here represented by θ_s , are heterogeneous and decline with depth exponentially (Beven & Kirkby, 1979). This heterogeneity is described discretely as

$$K_{\text{soil,sat},i} = K_{\text{soil,sat},0} \exp\left(-\frac{z_i}{e_K}\right) \quad (\text{S.2.7})$$

$$\theta_{s,i} = \theta_{s,0} \exp\left(-\frac{z_i}{e_n}\right) \quad (\text{S.2.8})$$

where $K_{\text{soil,sat},0}$ is the saturated hydraulic conductivity at the ground surface [$\text{m}\cdot\text{s}^{-1}$], $\theta_{s,0}$ is the saturated or maximum volumetric water content at the ground surface [-], and e_K and e_n are e-folding depths that describe how rapidly saturated conductivity and porosity decline with depth, respectively [m].

Flux (or Neumann) boundary conditions are applied at the upper boundary (soil surface) to solve Richards equations such that the magnitude of the Darcy flux at the ground surface equals either the infiltration or soil-evaporation rate depending on whether or not precipitation is occurring. Infiltration is currently assumed equal to the precipitation rate. The default lower boundary condition (at the bottom of the soil column, default 30 m) is in free drainage, which was chosen because the water table at the simulated site (see description of control simulation below; Tillar Valley within the Poblet Forest Natural Reserve, Prades Mountains, Northeastern Iberian Peninsula, 41° 19' 58.05" N, 1° 0' 52.26" E; Poyatos et al., 2013, 2018) has been estimated as deep as 70-100 m which agrees with nearby water table depth observations (Fan et al., 2013). These boundary conditions are described discretely as

$$q_1 = \begin{cases} -P, & P > 0 \\ E_{\text{soil}}, & P = 0 \end{cases} \quad (\text{S.2.9})$$

$$q_N = -K_{soil,N} \quad (S.2.10)$$

where P is precipitation [$\text{m}\cdot\text{s}^{-1}$], E_{soil} is soil evaporation [$\text{m}\cdot\text{s}^{-1}$], and the subscript N denotes the index of the deepest soil layer. Positive and negative fluxes are upward and downward, respectively. Soil evaporation is modeled by a simple, linearized form of Dalton's law of evaporation (Penman, 1948)

$$E_{soil} = \begin{cases} \frac{m_w g_a}{\rho P_{atm}} (e_{soil} - e_a), & e_{soil} > e_a \\ 0, & e_{soil} \leq e_a \end{cases} \quad (S.2.11)$$

where P_{atm} is atmospheric pressure [kPa]. The vapor pressure of the soil surface and air, e_{soil} and e_a [kPa] respectively, are determined from saturated vapor pressures, $e_{soil,sat}$ and $e_{a,sat}$ [kPa], at soil and air temperatures, T_a and T_{soil} [K], respectively, which are estimated by Tetens' (1930) equation, and by the relative humidities of the soil surface and air, RH_{soil} and RH [-], respectively, where RH_{soil} is solved by Philip and de Vries' (1957) equation.

$$RH_{soil} = \exp\left(\frac{\varpi m_w}{\rho R T_{soil}} \Psi_{soil,1}\right) \quad (S.2.12)$$

A conversion factor, ϖ , converts between units of Pascals and Megapascals ($\varpi = 10^{-6} \text{ MPa}\cdot\text{Pa}^{-1}$). The air's conductivity to vapor transport at the soil surface, g_a [$\text{mol H}_2\text{O}\cdot\text{m}^{-2}\cdot\text{s}^{-1}$], is estimated crudely from mean wind speed at 10 m elevation, u_{10} [$\text{m}\cdot\text{s}^{-1}$], by Eq. 7.33 in Campbell and Norman (1998).

Richards equation (Eq. S.2) is solved numerically as the following expanded partial differential equation in THORP by implicit finite difference

$$C \frac{\partial \Psi_{soil}}{\partial t} = \frac{K_{soil}}{\varpi \rho g} \frac{\partial^2 \Psi_{soil}}{\partial x^2} + \left(\frac{K'_{soil}}{\varpi \rho g} + \frac{\partial K_{soil}}{\partial \Psi_{soil}} \right) \frac{\partial \Psi_{soil}}{\partial x} + \frac{K_{soil}}{K_{soil,sat}} K'_{soil,sat} + f \quad (S.2.13)$$

where K'_{soil} and $K'_{soil,sat}$ are mathematically identical to $\partial K_{soil}/\partial x$ and $\partial K_{soil,sat}/\partial x$, respectively, but are treated as spatially-heterogeneous terms that are constant within a given time-step for the sake of numerical solution and are evaluated numerically by explicit finite difference from vectorized forms of K_{soil} and $K_{soil,sat}$. We emphasize that K'_{soil} is considered a constant within a time-step but not between time-steps and is updated at the beginning of each time-step. For numerical differentiation, we distinguish between two distances, $\Delta z_{i \rightarrow i+1}$ and Δz_i . We denote the distance between the centers of node i and node $i+1$ as $\Delta z_{i \rightarrow i+1}$; we use these distances to calculate the gradient of properties that exist at the centers of nodes. We denote the distance between the upper and lower boundaries of node i as Δz_i ; we use these distances to calculate the gradient of those properties that exist at the boundaries of nodes, namely vertical fluxes, q . We use superscripts to denote values in time (e.g. $\partial \Psi_{soil}/\partial t \approx (\Psi_{soil}^{t+\Delta t} - \Psi_{soil}^t)/\Delta t$). Eq. S.2.13 is solved as a system of N linear, coupled, discrete equations with N unknowns, namely $\Psi_{soil}^{t+\Delta t}$ at each node, that simplify to the general form

$$\mathbf{a}_i \Psi_{soil,i-1}^{t+\Delta t} + \mathbf{b}_i \Psi_{soil,i}^{t+\Delta t} + \mathbf{c}_i \Psi_{soil,i+1}^{t+\Delta t} = \mathbf{d}_i \quad (S.2.14)$$

where vectors \mathbf{a} , \mathbf{b} , and \mathbf{c} have units of [$\text{MPa}^{-1}\cdot\text{s}^{-1}$], vector \mathbf{d} is in units of [s^{-1}], and they are defined by the following.

$$\mathbf{a}_i = \frac{\frac{1}{\varpi \rho g} \left(\frac{K_{soil,i}}{\Delta z_i} + K'_{soil,i} \right) + \frac{\partial K_{soil,i}}{\partial \Psi_{soil,i}}}{\Delta z_{i-1 \rightarrow i}} \quad (S.2.15)$$

$$\mathbf{c}_i = \frac{\frac{1}{\varpi \rho g} \frac{K_{soil,i}}{\Delta z_i}}{\Delta z_{i \rightarrow i+1}} \quad (S.2.16)$$

$$\mathbf{b}_i = -\mathbf{a}_i - \mathbf{c}_i - \frac{C_i}{\Delta t} \quad (\text{S.2.17})$$

$$\mathbf{d}_i = -f_i - \frac{C_i}{\Delta t} \Psi_{soil,i}^t - \frac{K_{soil,i}}{K_{soil,sat,i}} K'_{soil,sat,i} \quad (\text{S.2.18})$$

This system of equations is valid for all nodes ($i \in [1, N]$), except at the boundaries ($i = 1$ and $i = N$) where several modifications must be made to account for the boundary conditions.

$$\mathbf{a}_1 = 0 \quad (\text{S.2.19})$$

$$\mathbf{a}_N = \frac{\frac{2}{\varpi \rho g} \frac{K_{soil,N}}{\Delta z_N}}{\Delta z_N} \quad (\text{S.2.20})$$

$$\mathbf{c}_1 = \frac{\frac{2}{\varpi \rho g} \frac{K_{soil,1}}{\Delta z_1}}{\Delta z_1} \quad (\text{S.2.21})$$

$$\mathbf{c}_N = 0 \quad (\text{S.2.22})$$

$$\mathbf{d}_1 = -f_1 - \frac{C_1}{\Delta t} \Psi_{soil,1}^t - \frac{K_{soil,1}}{K_{soil,sat,1}} K'_{soil,sat,1} + 2 \frac{q_1 + K_{soil,1}}{\Delta z_1} \quad (\text{S.2.23})$$

$$\mathbf{d}_N = -f_N - \frac{C_N}{\Delta t} \Psi_{soil,N}^t - \frac{K_{soil,N}}{K_{soil,sat,N}} K'_{soil,sat,N} - 2 \frac{q_N + K_{soil,N}}{\Delta z_N} \quad (\text{S.2.24})$$

With Eq. S.2.19-22 in place of Eq. S.2.15-16, vector \mathbf{b} may still be calculated by Eq. S.2.17 at $i = 1$ and $i = N$.

Eq. S.2.14 is solved in matrix notation as $\Psi^{t+\Delta t}_{soil} = \mathbf{A}^{-1} \mathbf{d} = \mathbf{A} \mathbf{d}$ where $\Psi^{t+\Delta t}_{soil}$ is a vector of all $\Psi^{t+\Delta t}_{soil}$ within the domain, and \mathbf{A} is an N by N sized matrix for which we present an example for the case of $N = 5$. Note that both \mathbf{a}_1 and \mathbf{c}_N never appear in \mathbf{A} .

$$\mathbf{A} = \begin{bmatrix} \mathbf{b}_1 & \mathbf{c}_1 & 0 & 0 & 0 \\ \mathbf{a}_2 & \mathbf{b}_2 & \mathbf{c}_2 & 0 & 0 \\ 0 & \mathbf{a}_3 & \mathbf{b}_3 & \mathbf{c}_3 & 0 \\ 0 & 0 & \mathbf{a}_4 & \mathbf{b}_4 & \mathbf{c}_4 \\ 0 & 0 & 0 & \mathbf{a}_5 & \mathbf{b}_5 \end{bmatrix} \quad (\text{S.2.25})$$

In alternative simulations with an introduced groundwater table, the lower boundary condition is treated as a constant soil water potential (Dirichlet) boundary condition. We set the pressure at the bottom of the soil column, $\Psi_{soil,LBC}$ [MPa], equal to the pressure that it would be if in hydrostatic equilibrium with a groundwater table of user-specified depth, $\Psi_{soil,LBC} = \varpi \cdot \rho \cdot g \cdot (d_{soil} - d_{WT})$, where d_{soil} is the depth to the bottom of the soil column [m] (default 30 m deep), and d_{WT} is the depth to the water table [m]. We recognize that this formulation does not necessitate that the true location of the water table (i.e. where $\Psi_{soil} = 0$) stay constant, and it should vary seasonally and due to transpirational changes. In this case, our numerical solution is still valid, as long as \mathbf{a}_N and \mathbf{b}_N are calculated by Eq. S.2.15 and S.2.17, respectively, with equal to \mathbf{c}_N zero (same as Eq. S.2.22), and \mathbf{d}_N is calculated by the following expression instead of Eq. S.2.24.

$$\mathbf{d}_N = -f_N - \frac{C_N}{\Delta t} \Psi_{soil,N}^t - \frac{K_{soil,N}}{K_{soil,sat,N}} K'_{soil,sat,N} - \frac{2}{\varpi \rho g} \frac{K_{soil,i}}{\Delta z_N^2} \Psi_{soil,LBC} \quad (\text{S.2.26})$$

S.3 Xylem Hydraulics

Xylem water potentials throughout the tree are assumed in steady-state in THORP for a given transpiration rate. Transpirative fluxes are solved through the belowground roots, the aboveground woody biomass, and within the canopy by the gradient of water potentials: soil water potentials, Ψ_{soil} [MPa], and xylem water potentials at the root collar, the stem apex, and leaf, Ψ_{Rc} , Ψ_S , and Ψ_L , respectively [MPa]. Values of Ψ_{Rc} , Ψ_S , and Ψ_L are determined such that the resulting fluxes are equal. Hydraulic conductances throughout the tree are organ-specific, and the conductance of roots vary between soil layers depending on the distribution of root-carbon with depth. This representation of xylem hydraulics is near-identical to that presented in Sperry et al. (2017), except gravitational potential gradients are fully represented, and root-water uptake has been modified so that rhizosphere resistances are not explicitly modeled but are implicitly represented through a belowground (soil-root) bulk hydraulic resistance.

Roots conduct water from each soil layer in a manner analogous to an in-parallel resistor (Section S.2), and each layer contributes its portion of transpiration, E_i , to the leaf-area specific transpiration, E [$\text{mol H}_2\text{O} \cdot \text{m}^{-2} \cdot \text{s}^{-1}$], where i represents the index of the soil layer, and the shallowest layer is denoted by $i = 1$ (see Eq. S.2.2). For a given root collar pressure, a soil layer's total water flux, $a_L E_i$ [$\text{mol H}_2\text{O} \cdot \text{s}^{-1}$], where a_L is the leaf area [m^2], is given by

$$a_L E_i = \frac{\Psi_{soil,i} - \Psi_{Rc} - \varpi \rho g z_i}{R_{R,i}} \quad (\text{S.3.1})$$

where $R_{R,i}$ is the hydraulic resistance of the roots in the i th soil layer [$\text{MPa} \cdot \text{s} \cdot (\text{mol H}_2\text{O})^{-1}$] that implicitly represents all processes that effect water flow between bulk soil and root collar, including embolism (Domec et al., 2006), rhizosphere resistance (Newman, 1969; Sperry et al., 1998), root shrinkage (Herkelrath et al., 1977), and switching between apoplastic and symplastic pathways (Fiscus, 1975; Steudle & Peterson, 1998). We do not explicitly model these processes to simplify our representation of root-water uptake and its parameterization and because belowground hydraulic resistances of trees are typically estimated from measurements of potential gradients between root collar and bulk soil which does not capture the various mechanisms separately (e.g. Martínez-Vilalta et al., 2007; Poyatos et al., 2018; Lintunen et al., 2019). This formulation of root-water uptake as in-parallel resistors does not explicitly represent the possibility of in-series resistances associated with water having to pass through axially through xylem that span multiple soil layers during the water's ascent to the root collar. These additional resistances are captured implicitly in THORP by defining a layer's root resistance, $R_{R,i}$, as the sum of 'horizontal' (intralayer), $R_{R,H,i}$ [$\text{MPa} \cdot \text{s} \cdot (\text{mol H}_2\text{O})^{-1}$], and 'vertical' (interlayer) resistances of the layer and all shallower layers, $R_{R,V,j}$ [$\text{MPa} \cdot \text{s} \cdot (\text{mol H}_2\text{O})^{-1}$], where j is all indices less than or equal to i .

$$R_{R,i} = R_{R,H,i} + \sum_{j=1}^i R_{R,V,j} \quad (\text{S.3.2})$$

This formulation of root hydraulic resistances prevents water uptake from soil-layers that are not hydraulically connected to the root collar. For example, if the k th soil layer contains no roots (specifically no $C_{R,V,k} = 0$), then water cannot be transported to the tree's xylem from layers deeper than k , regardless if those deeper layers contain roots. 'Horizontal' root resistances of a layer are assumed to be inversely-proportional to the intralayer-conductive root-carbon pool within that layer, $C_{R,H,i}$ [mol C]. This proportionality is defined by a proportionality constant, $\beta_{R,H}$ [$\text{MPa} \cdot \text{s} \cdot (\text{mol H}_2\text{O})^{-1} \cdot \text{mol C}$], that describes the minimum resistance, and a unitless factor, $f_{R,i}$ [-], that captures the increase in 'horizontal' resistance under increased water-stress, which is here represented by the water potentials along the root's hydraulic pathway, $\Psi_{soil,i}$ and Ψ_{Rc} . This unitless factor represents the magnitude of conductance loss relative to its maximum through the integral Kirchhoff transform (Sperry et al., 1998) and is defined by a Weibull function with two parameters, b_R [MPa] and c_R [-]. It should be noted that $f_{R,i}$ does not solely represent

embolism and cannot be interpreted as purely analogous to a vulnerability curve; nonetheless, we have formulated $f_{R,i}$ in terms of a belowground, effective vulnerability curve, $VC_R(\Psi)$.

$$R_{R,H,i} = \frac{\beta_{R,H}}{f_{R,i} C_{R,H,i}} \quad (\text{S.3.3})$$

$$f_{R,i} = \begin{cases} \frac{\int_{\Psi_{RC}}^{\Psi_{soil,i}} VC_R(\Psi) d\Psi}{\Psi_{soil,i} - \Psi_{RC}} = \frac{\int_{\Psi_{RC}}^{\Psi_{soil,i}} e^{-\left(\frac{-\Psi}{b_R}\right)^{c_R}} d\Psi}{\Psi_{soil,i} - \Psi_{RC}}, & \Psi_{soil,i} \neq \Psi_{RC} \\ VC_R(\Psi_{soil,i}) = e^{-\left(\frac{-\Psi_{soil,i}}{b_R}\right)^{c_R}}, & \Psi_{soil,i} = \Psi_{RC} \end{cases} \quad (\text{S.3.4})$$

‘Vertical’ root resistances are assumed proportional to the ratio of the square of the layer thickness, Δz_i^2 , and the interlayer-conductive root carbon pool, $C_{R,V,i}$ [mol C] by a proportionality constant, $\beta_{R,V}$ [MPa · mol C · s · (mol H₂O)⁻¹ · m⁻²]. We chose to represent this proportionality by Δz_i^2 , because the vertical conductivity is likely linearly proportional to the root area projected onto the horizontal plane, or at least as a first-order approximation, which is proportional to $C_{R,V,i}/\Delta z_i$, assuming that $C_{R,V}$ is analogous to volume. Converting from a conductivity to conductance requires another division by the appropriate length, Δz_i , and hence, we expect conductance be proportional to $C_{R,V,i}/\Delta z_i^2$. This formulation was also chosen so that the sum ‘vertical’ resistance would not depend on vertical discretization of the soil column when the root carbon concentration, $C_{R,V,i}/\Delta z_i$ [mol C · m⁻¹], was uniform among soil layers.

$$R_{R,V,i} = \beta_{R,V} \frac{\Delta z_i^2}{C_{R,V,i}} \quad (\text{S.3.5})$$

In equilibrium, the total amount of water conducted by roots, $a_L \cdot E$, equals the transpirative flux through the xylem of stems. In THORP, stem apex xylem potentials, Ψ_s , are determined from root collar xylem potentials, Ψ_{RC} , such that

$$a_L E = f_S k_S (\Psi_{RC} - \Psi_s - \varpi \rho g H) \quad (\text{S.3.6})$$

where k_S is the maximum stem conductance [mol H₂O · s⁻¹ · MPa⁻¹], H is tree height [m], and f_S is a unitless embolism factor that represents the magnitude of embolism in the stem through the integral Kirchhoff transform (Sperry et al., 1998) and is defined by a Weibull function that describes the stem’s vulnerability to embolism, $VC_S(\Psi)$, with two parameters, b_S [MPa] and c_S [-].

$$f_S = \frac{\int_{\Psi_S}^{\Psi_{RC}} VC_S(\Psi) d\Psi}{\Psi_{RC} - \Psi_S} = \frac{\int_{\Psi_S}^{\Psi_{RC}} e^{-\left(\frac{-\Psi}{b_S}\right)^{c_S}} d\Psi}{\Psi_{RC} - \Psi_S} \quad (\text{S.3.7})$$

The maximum stem conductance, k_S , scales with tree size as a power-law function of the sapwood and heartwood areas from an assumed fractal-like hydraulic tree architecture similar to West et al. (1999), Savage et al. (2010), Sperry et al. (2012), and Hölttä et al. (2013). See Section S.4 for the full derivation of how THORP models the scaling between stem conductance and aboveground woody biomass.

Leaf water potentials, Ψ_L , are determined from stem apex potentials, Ψ_s , such that

$$E = f_L k_L (\Psi_s - \Psi_L) \quad (\text{S.3.8})$$

where k_L is the leaf area-specific maximum leaf conductance, k_L [mol H₂O · m⁻² · s⁻¹ · MPa⁻¹], and f_L is a unitless factor that represents the magnitude of embolism in leaves through the integral Kirchhoff transform (Sperry et al., 1998). Vulnerability to embolism is defined by a Weibull function, $VC_L(\Psi)$, with two parameters, b_L [MPa] and c_L [-].

$$f_L = \frac{\int_{\Psi_L}^{\Psi_S} VC_L(\Psi) d\Psi}{\Psi_S - \Psi_L} = \frac{\int_{\Psi_L}^{\Psi_S} e^{-\left(\frac{-\Psi}{b_L}\right)^{c_L}} d\Psi}{\Psi_S - \Psi_L} \quad (\text{S.3.9})$$

Lastly, transpiration is also defined by the diffusional conductance to water vapor from the leaf, G_w [mol $\text{H}_2\text{O} \cdot \text{m}^{-2} \cdot \text{s}^{-1} \cdot \text{kPa}^{-1}$]. Unlike Sperry et al. (2017), we ignore transpirational leaf cooling and assume that leaf and air temperatures are equal (see Section S.6 for explanation). Due to this simplification, the vapor pressure difference between leaf and air is $e_{a,sat}(1 - RH)$, where $e_{a,sat}$ is the air's saturated vapor pressure [kPa], and RH is the air's relative humidity (both terms introduced in Section S.2).

$$E = G_w e_{a,sat} (1 - RH) \quad (\text{S.3.10})$$

The remainder of this subsection is devoted to finding an approximate solution for the derivatives of transpiration with respect to biomass, represented by dE/dD , dE/da_L , $dE/dC_{R,H,i}$, and $dE/dC_{R,V,i}$ for sapwood, leaf, and the two root carbon pools, respectively, which are used in Section S.8 to approximate the optimal path for allocation. The following expression can be derived from Eq. S.3.4, Eq. S.3.7, and Eq. S.3.9 and will be used in remainder of this section (Eq. S.3.16-65).

$$\frac{\partial f_{R,i}}{\partial \Psi_{Rc}} = \begin{cases} \frac{f_{R,i} - VC_R(\Psi_{Rc})}{\Psi_{soil,i} - \Psi_{Rc}}, & \Psi_{soil,i} \neq \Psi_{Rc} \\ \frac{1}{2} \frac{\partial VC_R(\Psi_{Rc})}{\partial \Psi_{Rc}}, & \Psi_{soil,i} = \Psi_{Rc} \end{cases} \quad (\text{S.3.11})$$

$$\frac{\partial f_S}{\partial \Psi_S} = \frac{f_S - VC_S(\Psi_S)}{\Psi_{Rc} - \Psi_S} \quad (\text{S.3.12})$$

$$\frac{\partial f_S}{\partial \Psi_{Rc}} = \frac{VC_S(\Psi_{Rc}) - f_S}{\Psi_{Rc} - \Psi_S} \quad (\text{S.3.13})$$

$$\frac{\partial f_L}{\partial \Psi_L} = \frac{f_L - VC_L(\Psi_L)}{\Psi_S - \Psi_L} \quad (\text{S.3.14})$$

$$\frac{\partial f_L}{\partial \Psi_S} = \frac{VC_L(\Psi_S) - f_L}{\Psi_S - \Psi_L} \quad (\text{S.3.15})$$

The one-half in Eq. S.3.11 comes from $f_{R,i}$ being a mean of $VC_R(\Psi_{Rc})$ and $VC_R(\Psi_{soil,i})$. Rather than derive dE/dD , dE/da_L , $dE/dC_{R,H,i}$, and $dE/dC_{R,V,i}$ separately, we derive a general equation, $dE/d\epsilon$, that may be later simplified to reach each specific derivative. From the previous equations in this section, it is possible to estimate two definitions of $d\Psi_S/d\epsilon$, which can be set equal and rearranged for $dE/d\epsilon$. The first definition of $d\Psi_S/d\epsilon$ requires differentiating Ψ_S as defined by Eq. S.3.6, and defining $df_S/d\epsilon = \partial f_S/\partial \Psi_S \cdot d\Psi_S/d\epsilon + \partial f_S/\partial \Psi_{Rc} \cdot d\Psi_{Rc}/d\epsilon$ by the chain-rule,

$$\Psi_S = \Psi_{Rc} - \omega \rho g H - \frac{a_L E}{f_S k_S} \quad (\text{S.3.16a})$$

$$\Rightarrow \frac{d\Psi_S}{d\epsilon} = \left\{ \begin{aligned} & \frac{d\Psi_{Rc}}{d\epsilon} - \omega \rho g \frac{\partial H}{\partial \epsilon} - \frac{1}{f_S k_S} \left(E \frac{da_L}{d\epsilon} + a_L \frac{dE}{d\epsilon} \right) \\ & + \frac{\partial \Psi_S}{\partial f_S} \left(\frac{\partial f_S}{\partial \Psi_S} \frac{d\Psi_S}{d\epsilon} + \frac{\partial f_S}{\partial \Psi_{Rc}} \frac{d\Psi_{Rc}}{d\epsilon} \right) + \frac{\partial \Psi_S}{\partial k_S} \frac{\partial k_S}{\partial \epsilon} \end{aligned} \right\} \quad (\text{S.3.16b})$$

$$\Rightarrow \frac{\partial \Psi_S}{\partial f_S} = \frac{a_L E}{f_S^2 k_S} \quad (\text{S.3.16c})$$

$$\Rightarrow \frac{\partial \Psi_S}{\partial k_S} = \frac{a_L E}{f_S k_S^2} \quad (\text{S.3.16d})$$

$$\Rightarrow \frac{d\Psi_S}{d\epsilon} = \frac{1}{\mathfrak{a}} \left[\mathfrak{b} \frac{d\Psi_{Rc}}{d\epsilon} - \omega \rho g \frac{\partial H}{\partial \epsilon} + \frac{a_L E}{f_S k_S^2} \frac{\partial k_S}{\partial \epsilon} - \frac{1}{f_S k_S} \left(E \frac{da_L}{d\epsilon} + a_L \frac{dE}{d\epsilon} \right) \right] \quad (\text{S.3.16e})$$

where \mathfrak{a} and \mathfrak{b} are unitless terms.

$$\mathfrak{a} = 1 - \frac{a_L E}{f_S^2 k_S} \frac{\partial f_S}{\partial \Psi_S} = \frac{1}{f_S} V C_S(\Psi_S) + \frac{\omega \rho g H}{\Psi_{Rc} - \Psi_S} \left(1 - \frac{1}{f_S} V C_S(\Psi_S) \right) \quad (\text{S.3.17})$$

$$\mathfrak{b} = 1 + \frac{a_L E}{f_S^2 k_S} \frac{\partial f_S}{\partial \Psi_{Rc}} = \frac{1}{f_S} V C_S(\Psi_{Rc}) + \frac{\omega \rho g H}{\Psi_{Rc} - \Psi_S} \left(1 - \frac{1}{f_S} V C_S(\Psi_{Rc}) \right) \quad (\text{S.3.18})$$

Completing this first definition requires defining $d\Psi_{Rc}/d\epsilon$. We assume soil hydrology is independent from physiology such that $d\Psi_{soil,i}/d\epsilon_j = 0$ for all combinations of i potentials and j soil layers (if applicable) and by consequence that $df_{R,i}/d\epsilon = \partial f_{R,i}/\partial \Psi_{Rc} \cdot d\Psi_{Rc}/d\epsilon$ to derive the following equation from Eq. S.2.2 and Eq. S.3.2-4 and simplify,

$$\Psi_{Rc} = \frac{-a_L E + \sum_{j=1}^N \frac{\Psi_{soil,j} - \omega \rho g z_j}{R_{R,j}}}{\sum_{j=1}^N \frac{1}{R_{R,j}}} \quad (\text{S.3.19a})$$

$$\Rightarrow \frac{d\Psi_{Rc}}{d\epsilon} = \frac{\partial \Psi_{Rc}}{\partial (a_L E)} \frac{d(a_L E)}{d\epsilon} + \sum_{j=1}^N \frac{\partial \Psi_{Rc}}{\partial R_{R,j}} \left(\frac{\partial R_{R,j}}{\partial \epsilon} + \frac{\partial R_{R,j}}{\partial f_{R,j}} \frac{\partial f_{R,j}}{\partial \Psi_{Rc}} \frac{d\Psi_{Rc}}{d\epsilon} \right) \quad (\text{S.3.19b})$$

$$\Rightarrow \frac{d\Psi_{Rc}}{d\epsilon} = \frac{-\frac{a_L \frac{dE}{d\epsilon} + E \frac{da_L}{d\epsilon}}{\sum_{j=1}^N \frac{1}{R_{R,j}}} + \sum_{j=1}^N \frac{\partial \Psi_{Rc}}{\partial R_{R,j}} \frac{\partial R_{R,j}}{\partial \epsilon}}{1 - \sum_{j=1}^N \frac{\partial \Psi_{Rc}}{\partial R_{R,j}} \frac{\partial R_{R,j}}{\partial f_{R,j}} \frac{\partial f_{R,j}}{\partial \Psi_{Rc}}} \quad (\text{S.3.19c})$$

$$\Rightarrow \frac{\partial \Psi_{Rc}}{\partial R_{R,j}} = \frac{-a_L E + \left(\sum_{i=1}^N \frac{\Psi_{soil,i} - \omega \rho g z_i}{R_{R,i}} \right) - (\Psi_{soil,j} - \omega \rho g z_j) \left(\sum_{i=1}^N \frac{1}{R_{R,i}} \right)}{R_{R,j}^2 \left(\sum_{i=1}^N \frac{1}{R_{R,i}} \right)^2} \quad (\text{S.3.19d})$$

$$\Rightarrow \frac{\partial \Psi_{Rc}}{\partial R_{R,j}} = \frac{\Psi_{Rc} - \Psi_{soil,j} + \omega \rho g z_j}{R_{R,j}^2 \left(\sum_{i=1}^N \frac{1}{R_{R,i}} \right)} \quad (\text{S.3.19e})$$

$$\Rightarrow \frac{\partial \Psi_{Rc}}{\partial R_{R,j}} = -\frac{1}{\left(\sum_{i=1}^N \frac{1}{R_{R,i}} \right)} \frac{a_L E_j}{R_{R,j}} \quad (\text{S.3.19f})$$

$$\Rightarrow \frac{d\Psi_{Rc}}{d\epsilon} = \frac{-\left(a_L \frac{dE}{d\epsilon} + E \frac{da_L}{d\epsilon} \right) - \sum_{j=1}^N a_L \frac{E_j}{R_{R,j}} \frac{\partial R_{R,j}}{\partial \epsilon}}{\left(\sum_{i=1}^N \frac{1}{R_{R,i}} \right) - \left(\sum_{j=1}^N a_L \frac{R_{R,H,j}}{f_{R,j}} \frac{\partial f_{R,j}}{\partial \Psi_{Rc}} \right)} \quad (\text{S.3.19g})$$

$$\Rightarrow \frac{d\Psi_{Rc}}{d\epsilon} = \frac{-1}{\mathfrak{c}} \left[\frac{dE}{d\epsilon} + \frac{E}{a_L} \frac{da_L}{d\epsilon} + \sum_{j=1}^N \frac{E_j}{R_{R,j}} \frac{\partial R_{R,j}}{\partial \epsilon} \right] \quad (\text{S.3.19h})$$

where \mathfrak{c} is a term with the same units as leaf area-specific maximum leaf conductance, k_L [$\text{mol H}_2\text{O} \cdot \text{m}^{-2} \cdot \text{s}^{-1} \cdot \text{MPa}^{-1}$],

$$\mathfrak{c} = \sum_{j=1}^N \frac{1}{R_{R,j}} \left(\frac{1}{a_L} - E_j \frac{R_{R,H,j}}{f_{R,j}} \frac{\partial f_{R,j}}{\partial \Psi_{Rc}} \right) \quad (\text{S.3.20})$$

which can be more intuitively interpreted as $\mathfrak{c} = -dE/d\Psi_{Rc}$. By plugging Eq. S.3.19h into Eq. S.3.16e, we achieve our first definition for $d\Psi_S/d\epsilon$.

$$\frac{d\Psi_S}{d\epsilon} = -\frac{1}{\mathfrak{a}} \left[\left(\frac{\mathfrak{b}}{\mathfrak{c}} + \frac{a_L}{f_S k_S} \right) \left(\frac{dE}{d\epsilon} + \frac{E}{a_L} \frac{da_L}{d\epsilon} \right) + \varpi \rho g \frac{\partial H}{\partial \epsilon} - \frac{a_L E}{f_S k_S^2} \frac{\partial k_S}{\partial \epsilon} + \frac{\mathfrak{b}}{\mathfrak{c}} \sum_{j=1}^N \frac{E_j}{R_{R,j}} \frac{\partial R_{R,j}}{\partial \epsilon} \right] \quad (\text{S.3.21})$$

The derivation for the second definition of $d\Psi_S/d\epsilon$ begins by differentiating Ψ_S as defined by Eq. S.3.8, and defining $df_L/d\epsilon = \partial f_L/\partial \Psi_S \cdot d\Psi_S/d\epsilon + \partial f_L/\partial \Psi_L \cdot d\Psi_L/d\epsilon$,

$$\Psi_S = \Psi_L + \frac{E}{f_L k_L} \quad (\text{S.3.22a})$$

$$\Rightarrow \frac{d\Psi_S}{d\epsilon} = \frac{d\Psi_L}{d\epsilon} + \frac{\partial \Psi_S}{\partial E} \frac{dE}{d\epsilon} + \frac{\partial \Psi_S}{\partial f_L} \left(\frac{\partial f_L}{\partial \Psi_S} \frac{d\Psi_S}{d\epsilon} + \frac{\partial f_L}{\partial \Psi_L} \frac{d\Psi_L}{d\epsilon} \right) \quad (\text{S.3.22b})$$

$$\Rightarrow \frac{\partial \Psi_S}{\partial f_L} = -\frac{E}{f_L^2 k_L} \quad (\text{S.3.22c})$$

$$\Rightarrow \frac{d\Psi_S}{d\epsilon} = \frac{1}{\mathfrak{d}} \left(\mathfrak{e} \frac{d\Psi_L}{d\epsilon} + \frac{1}{f_L k_L} \frac{dE}{d\epsilon} \right) \quad (\text{S.3.22d})$$

where \mathfrak{d} , and \mathfrak{e} are unitless terms.

$$\mathfrak{d} = 1 + \frac{E}{f_L^2 k_L} \frac{\partial f_L}{\partial \Psi_S} = \frac{1}{f_L} V C_L(\Psi_S) \quad (\text{S.3.23})$$

$$\mathfrak{e} = 1 - \frac{E}{f_L^2 k_L} \frac{\partial f_L}{\partial \Psi_L} = \frac{1}{f_L} V C_L(\Psi_L) \quad (\text{S.3.24})$$

Completing this second definition requires defining $d\Psi_L/d\epsilon$, which we calculate by defining transpiration, E , from the integral supply curve (Sperry & Love, 2015),

$$E = \int_{\Psi_L}^{\Psi_{L,0}} k_c d\Psi \quad (\text{S.3.25})$$

where $k_c = -dE/d\Psi_L$ is the canopy conductance [$\text{mol H}_2\text{O} \cdot \text{m}^{-2} \cdot \text{s}^{-1} \cdot \text{MPa}^{-1}$], $\Psi_{L,0}$ is the leaf water potential [MPa] from the supply curve at which $E = 0$, coinciding with $k_c = k_{c,max}$, and Ψ_L is the realized leaf water potential [MPa]. $\Psi_{L,0}$ can be defined by from Eq. S.3.1, Eq. S.3.6 and Eq. S.3.8 by setting E to zero,

$$\Psi_{L,0} = \Psi_{Rc,0} - \varpi \rho g H \quad (\text{S.3.26})$$

$$\Psi_{Rc,0} = \frac{\sum_{i=1}^N \frac{\Psi_{soil,i} - \varpi \rho g z_i}{R_{R,0,i}}}{\sum_{i=1}^N \frac{1}{R_{R,0,i}}} \quad (\text{S.3.27})$$

where subscripts of 0 denote values coinciding with $\Psi_{L,0}$ and $E = 0$. We apply Leibniz's rule to the supply curve as defined by Eq. S.3.25 and rearrange.

$$\frac{d\Psi_L}{d\epsilon} = -\frac{1}{k_c} \frac{dE}{d\epsilon} + \frac{k_{c,max}}{k_c} \frac{d\Psi_{L,0}}{d\epsilon} + \frac{1}{k_c} \int_{\Psi_L}^{\Psi_{L,0}} \frac{dk_c}{d\epsilon} d\Psi \quad (\text{S.3.28})$$

From Eq. S.3.23-24, we define $d\Psi_{L,0}/d\epsilon$, and note that the solution for $d\Psi_{Rc,0}/d\epsilon$ is simplified case of Eq. S.3.19h when setting $E = 0$ and $dE/d\epsilon = 0$:

$$\frac{d\Psi_{Rc,0}}{d\epsilon} = -\frac{1}{\mathfrak{c}_0} \sum_{i=1}^N \frac{E_{0,i}}{R_{R,0,i}} \frac{\partial R_{R,0,i}}{\partial \epsilon} \quad (\text{S.3.29})$$

$$\frac{d\Psi_{L,0}}{d\epsilon} = \frac{d\Psi_{Rc,0}}{d\epsilon} - \varpi \rho g \frac{\partial H}{\partial \epsilon} \quad (\text{S.3.30})$$

Before proceeding with our derivation for our second solution of $d\Psi_L/d\epsilon$, we must define k_c to solve the integral term in Eq. S.3.28. We solve for $k_c = -dE/d\Psi$ by solving for $d\Psi_L/dE$ from a definition of Ψ_L based on a combination of Eq. S.3.1, Eq.S.3.6, and Eq.S.3.8 and taking the reciprocal.

$$\Psi_L = \frac{\sum_{j=1}^N \frac{\Psi_{soil,j} - \varpi \rho g z_j}{R_{R,j}}}{\sum_{j=1}^N \frac{1}{R_{R,j}}} - \varpi \rho g H - \left(\frac{1}{f_L k_L} + \frac{a_L}{f_S k_S} + \frac{a_L}{\sum_{j=1}^N \frac{1}{R_{R,j}}} \right) E \quad (\text{S.3.31a})$$

$$\Rightarrow \frac{d\Psi_L}{dE} = \left\{ \begin{array}{l} \frac{\partial \Psi_L}{\partial E} + \frac{\partial \Psi_L}{\partial f_L} \left(\frac{\partial f_L}{\partial \Psi_S} \frac{d\Psi_S}{dE} + \frac{\partial f_L}{\partial \Psi_L} \frac{d\Psi_L}{dE} \right) \\ + \frac{\partial \Psi_L}{\partial f_S} \left(\frac{\partial f_S}{\partial \Psi_{Rc}} \frac{d\Psi_{Rc}}{dE} + \frac{\partial f_S}{\partial \Psi_S} \frac{d\Psi_S}{dE} \right) \\ + \frac{d\Psi_{Rc}}{dE} \sum_{j=1}^N \frac{\partial \Psi_L}{\partial R_{R,j}} \frac{\partial R_{R,j}}{\partial \Psi_{Rc}} \end{array} \right\} \quad (\text{S.3.31b})$$

$$\Rightarrow \frac{d\Psi_L}{dE} = \left\{ \begin{array}{l} \frac{\partial \Psi_L}{\partial E} + \left(\frac{\partial \Psi_L}{\partial f_L} \frac{\partial f_L}{\partial \Psi_S} + \frac{\partial \Psi_L}{\partial f_S} \frac{\partial f_S}{\partial \Psi_S} \right) \frac{d\Psi_S}{dE} \\ + \left(\frac{\partial \Psi_L}{\partial f_S} \frac{\partial f_S}{\partial \Psi_{Rc}} + \sum_{j=1}^N \frac{\partial \Psi_L}{\partial R_{R,j}} \frac{\partial R_{R,j}}{\partial \Psi_{Rc}} \right) \frac{d\Psi_{Rc}}{dE} \end{array} \right\} \quad (\text{S.3.31c})$$

$$\Rightarrow \frac{\partial \Psi_L}{\partial E} = - \left(\frac{1}{f_L k_L} + \frac{a_L}{f_S k_S} + \frac{a_L}{\sum_{j=1}^N \frac{1}{R_{R,j}}} \right) \quad (\text{S.3.27d})$$

$$\Rightarrow \frac{\partial \Psi_L}{\partial f_L} = \frac{E}{f_L^2 k_L} \quad (\text{S.3.31e})$$

$$\Rightarrow \frac{\partial \Psi_L}{\partial f_S} = \frac{a_L E}{f_S^2 k_S} \quad (\text{S.3.31f})$$

$$\Rightarrow \frac{\partial \Psi_L}{\partial R_{R,j}} = \frac{\partial \Psi_{Rc}}{\partial R_{R,j}} = - \frac{1}{\left(\sum_{i=1}^N \frac{1}{R_{R,i}} \right)} \frac{a_L E_j}{R_{R,j}} \quad (\text{S.3.27g})$$

$$\Rightarrow \frac{d\Psi_S}{dE} = \frac{1}{\mathfrak{a}} \left[\mathfrak{b} \frac{d\Psi_{Rc}}{dE} - \frac{a_L}{f_S k_S} \right] \quad (\text{S.3.31h})$$

$$\Rightarrow \frac{d\Psi_{Rc}}{dE} = \frac{-1}{\mathfrak{c}} \quad (\text{S.3.31i})$$

$$\Rightarrow \frac{d\Psi_L}{dE} = - \frac{1}{f_L k_L} - \frac{\mathfrak{d}}{\mathfrak{a}} \left(\frac{\mathfrak{b}}{\mathfrak{c}} + \frac{a_L}{f_S k_S} \right) \quad (\text{S.3.31j})$$

$$\Rightarrow k_c = - \frac{dE}{d\Psi_L} = \frac{-1}{\frac{d\Psi_L}{dE}} \quad (\text{S.3.31k})$$

$$\Rightarrow k_c = \frac{\mathfrak{e}}{\frac{1}{f_L k_L} + \frac{\mathfrak{d}}{\mathfrak{a}} \left(\frac{\mathfrak{b}}{\mathfrak{c}} + \frac{a_L}{f_S k_S} \right)} \quad (\text{S.3.31j})$$

This definition of k_c is not complete, since several of the included terms require *a priori* knowledge of the xylem water potentials throughout the tree. However, from Eq. S.3.31j, we can define the maximum canopy conductance, $k_{c,max}$, since \mathfrak{a} , \mathfrak{b} , \mathfrak{d} , and \mathfrak{e} equal to zero when $E = 0$,

$$k_{c,max} = \frac{1}{\frac{1}{f_{L,0} k_L} + \frac{1}{\mathfrak{c}_0} + \frac{a_L}{f_{S,0} k_S}} \quad (\text{S.3.32})$$

where $f_{L,0}$ and $f_{S,0}$ are values of f_L and f_S when $E = 0$, which require only *a priori* knowledge of $\Psi_{Rc,0}$ to define.

$$f_{L,0} = VC_L(\Psi_{RC,0} - \varpi \rho g H) \quad (\text{S.3.33})$$

$$f_{S,0} = \frac{\int_{\Psi_{RC,0} - \varpi \rho g H}^{\Psi_{RC,0}} VC_S(\Psi) d\Psi}{\varpi \rho g H} \quad (\text{S.3.34})$$

A second definition of k_c can be defined from *gain-risk* algorithm's objective function for stomata optimization (Sperry et al., 2017),

$$\max_{\Psi_L} \left[\frac{A_n}{A_{n,max}} - \frac{k_{c,max} - k_c}{k_{c,max}} \right] = \max_{\Psi_L} \left[\frac{A_n}{A_{n,max}} + \frac{k_c}{k_{c,max}} \right] \quad (\text{S.3.35a})$$

$$\Rightarrow \frac{1}{A_{n,max}} \frac{dA_n}{d\Psi} + \frac{1}{k_{c,max}} \frac{dk_c}{d\Psi} = -\frac{\lambda}{A_{n,max}} k_c + \frac{1}{k_{c,max}} \frac{dk_c}{d\Psi} = 0 \quad (\text{S.3.35b})$$

$$\Rightarrow \frac{dk_c}{d\Psi_L} = -\frac{k_{c,max}}{A_{n,max}} \frac{dA_n}{d\Psi_L} = \lambda \frac{k_{c,max}}{A_{n,max}} k_c \quad (\text{S.3.35c})$$

$$\Rightarrow k_c = k_{c,max} \exp \left[\frac{k_{c,max}}{A_{n,max}} \int_{\Psi_L}^{\Psi_{L,0}} \lambda(\Psi) d\Psi \right] \quad (\text{S.3.35d})$$

where $A_{n,max}$ is the maximum value of net photosynthesis expected within the possible ranges of stomatal control (Sperry et al., 2017), and where the optimal or realized Ψ_L is the value of Ψ_L at which the two definitions of k_c given by Eq. S.3.31j and Eq. S.3.35d are equal. Now with definitions for both k_c and $k_{c,max}$, we return to our derivation of the second solution of $d\Psi_L/d\epsilon$. We decompose the integral in Eq. S.3.28 in approximate form below.

$$\int_{\Psi_L}^{\Psi_{L,0}} \frac{dk_c}{d\epsilon} d\Psi \cong \left\{ \begin{aligned} & \frac{d\Psi_L}{d\epsilon} \int_{\Psi_L}^{\Psi_{L,0}} \frac{dk_c}{d\Psi_L} d\Psi \\ & + \frac{\partial k_{c,max}}{\partial \epsilon} \int_{\Psi_L}^{\Psi_{L,0}} \frac{\partial k_c}{\partial k_{c,max}} d\Psi \\ & + \frac{\partial A_{n,max}}{\partial \epsilon} \int_{\Psi_L}^{\Psi_{L,0}} \frac{\partial k_c}{\partial A_{n,max}} d\Psi \end{aligned} \right\} \quad (\text{S.3.36})$$

We have assumed that the change in k_c can reasonably be approximated by the changes in the three terms from the *gain-risk* algorithm that control k_c most, namely Ψ_L , $k_{c,max}$, and $A_{n,max}$. From Eq. S.3.35c, the first integral on the right-hand side of Eq. S.3.36 can be solved.

$$\int_{\Psi_L}^{\Psi_{L,0}} \frac{dk_c}{d\Psi_L} d\Psi = -\frac{k_{c,max}}{A_{n,max}} \int_{\Psi_L}^{\Psi_{L,0}} \frac{dA_n}{d\Psi_L} d\Psi = \frac{k_{c,max}}{A_{n,max}} A_n \quad (\text{S.3.37})$$

From Eq. S.3.35d, we define $\partial k_c / \partial k_{c,max}$,

$$\frac{\partial k_c}{\partial k_{c,max}} = \frac{k_c}{k_{c,max}} \left[1 + \ln \left(\frac{k_c}{k_{c,max}} \right) \right] = \frac{k_c}{k_{c,max}} \left[1 + \frac{k_{c,max}}{A_{n,max}} \int_{\Psi_L}^{\Psi_{L,0}} \lambda d\Psi \right] \quad (\text{S.3.38a})$$

$$\Rightarrow \frac{\partial k_c}{\partial k_{c,max}} = \frac{1}{k_{c,max}} \left[k_c + \frac{k_{c,max}}{A_{n,max}} \int_{\Psi_L}^{\Psi_{L,0}} k_c \lambda d\Psi \right] = \frac{k_c}{k_{c,max}} + \frac{A_n}{A_{n,max}} \quad (\text{S.3.38b})$$

which we integrate to achieve the second integral term on the right-hand side of Eq. S.3.36.

$$\int_{\Psi_L}^{\Psi_{L,0}} \frac{\partial k_c}{\partial k_{c,max}} d\Psi = \frac{E}{k_{c,max}} + \frac{A_n}{A_{n,max}} (\Psi_{L,0} - \Psi_L) \quad (\text{S.3.39})$$

Similarly, from Eq. S.3.35d, we can define the third integral term on the right-hand side of Eq. S.3.36.

$$\frac{\partial k_c}{\partial A_{n,max}} = -\frac{k_c}{A_{n,max}} \ln\left(\frac{k_c}{k_{c,max}}\right) = -\frac{k_c k_{c,max}}{A_{n,max}^2} \int_{\Psi_L}^{\Psi_{L,0}} \lambda d\Psi \quad (\text{S.3.40a})$$

$$\Rightarrow \frac{\partial k_c}{\partial A_{n,max}} = -\frac{k_{c,max}}{A_{n,max}^2} \int_{\Psi_L}^{\Psi_{L,0}} k_c \lambda d\Psi = -k_{c,max} \frac{A_n}{A_{n,max}^2} \quad (\text{S.3.40b})$$

$$\Rightarrow \int_{\Psi_L}^{\Psi_{L,0}} \frac{\partial k_c}{\partial A_{n,max}} d\Psi = -k_{c,max} \frac{A_n}{A_{n,max}^2} (\Psi_{L,0} - \Psi_L) \quad (\text{S.3.40c})$$

Since we have ignored transpirational cooling, leaf temperature is constant with regards to the stomatal optimization, and $A_{n,max}$ always co-occurs with E_{max} , and the $dA_{n,max}/d\epsilon$ can be written as

$$\frac{dA_{n,max}}{d\epsilon} = \lambda_{crit} \frac{dE_{max}}{d\epsilon} + \wp_{crit} \frac{dI}{d\epsilon} \quad (\text{S.3.41})$$

where λ_{crit} and \wp_{crit} are the marginal water- and light-use efficiencies evaluated at $A_n = A_{n,max}$ and $E = E_{max}$, and I is the light capture. The marginal light-use efficiency is later defined in Eq. S.6.5, and $dI/d\epsilon$ terms are defined by Eq. S.5.3-5. Similar to Eq. S.3.25, we can define E_{max} from the supply curve,

$$E_{max} = \int_{\Psi_{L,crit}}^{\Psi_{L,0}} k_c d\Psi \quad (\text{S.3.42})$$

where $\Psi_{L,crit}$ is the most-negative possible leaf water potential at which $k_c = 0$. Like Eq. S.3.28, we apply the Leibniz's rule to calculate the derivative of E_{max} (recall that $k_c = 0$ at $\Psi_{L,crit}$),

$$\frac{dE_{max}}{d\epsilon} = k_{c,max} \frac{d\Psi_{L,0}}{d\epsilon} + \int_{\Psi_{L,crit}}^{\Psi_{L,0}} \frac{dk_c}{d\epsilon} d\Psi \quad (\text{S.3.43})$$

which when combined with Eq. S.3.28 reveals the following expression.

$$\frac{dE_{max}}{d\epsilon} = \frac{dE}{d\epsilon} + k_c \frac{d\Psi_L}{d\epsilon} + \int_{\Psi_{L,crit}}^{\Psi_L} \frac{dk_c}{d\epsilon} d\Psi \quad (\text{S.3.44})$$

To solve the integral on the right-hand side of Eq. S.3.44, we make the same approximation as in Eq. S.3.36 for the new bounds of integration.

$$\int_{\Psi_{L,crit}}^{\Psi_L} \frac{dk_c}{d\epsilon} d\Psi \cong \left\{ \begin{aligned} &\frac{d\Psi_L}{d\epsilon} \int_{\Psi_{L,crit}}^{\Psi_L} \frac{dk_c}{d\Psi} d\Psi \\ &+ \frac{dk_{c,max}}{d\epsilon} \int_{\Psi_{L,crit}}^{\Psi_L} \frac{dk_c}{dk_{c,max}} d\Psi \\ &+ \frac{dA_{n,max}}{d\epsilon} \int_{\Psi_{L,crit}}^{\Psi_L} \frac{dk_c}{dA_{n,max}} d\Psi \end{aligned} \right\} \quad (\text{S.3.45})$$

We evaluate each integral term on the right-hand side of Eq. S.3.45 by applying the same procedures applied between Eq. S.3.37-40 for the new bounds of integration.

$$\int_{\Psi_{L,crit}}^{\Psi_L} \frac{dk_c}{d\epsilon} d\Psi = \left\{ \begin{aligned} &k_{c,max} \left(1 - \frac{A_n}{A_{n,max}}\right) \frac{d\Psi_L}{d\epsilon} \\ &+ \left[\frac{E_{max}-E}{k_{c,max}} + \frac{A_n}{A_{n,max}} (\Psi_L - \Psi_{L,crit}) \right] \frac{dk_{c,max}}{d\epsilon} \\ &- k_{c,max} \frac{A_n}{A_{n,max}^2} (\Psi_L - \Psi_{L,crit}) \frac{dA_{n,max}}{d\epsilon} \end{aligned} \right\} \quad (\text{S.3.46})$$

Plugging Eq. S.3.36 into Eq. S.3.41 gives a final definition for $dA_{n,max}/d\epsilon$.

$$\frac{dA_{n,max}}{d\epsilon} = \lambda_{crit} \left\{ \begin{aligned} & \frac{dE}{d\epsilon} + \left[k_c + k_{c,max} \left(1 - \frac{A_n}{A_{n,max}} \right) \right] \frac{d\Psi_L}{d\epsilon} \\ & + \left[\frac{E_{max}-E}{k_{c,max}} + \frac{A_n}{A_{n,max}} (\Psi_L - \Psi_{L,crit}) \right] \frac{dk_{c,max}}{d\epsilon} \\ & - k_{c,max} \frac{A_n}{A_{n,max}^2} (\Psi_L - \Psi_{L,crit}) \frac{dA_{n,max}}{d\epsilon} \end{aligned} \right\} + \wp_{crit} \frac{dI}{d\epsilon} \quad (S.3.47a)$$

$$\Rightarrow \frac{dA_{n,max}}{d\epsilon} = \frac{\lambda_{crit} \left\{ \begin{aligned} & \frac{dE}{d\epsilon} + \left[k_c + k_{c,max} \left(1 - \frac{A_n}{A_{n,max}} \right) \right] \frac{d\Psi_L}{d\epsilon} \\ & + \left[\frac{E_{max}-E}{k_{c,max}} + \frac{A_n}{A_{n,max}} (\Psi_L - \Psi_{L,crit}) \right] \frac{dk_{c,max}}{d\epsilon} \end{aligned} \right\} + \wp_{crit} \frac{dI}{d\epsilon}}{1 + \lambda_{crit} k_{c,max} \frac{A_n}{A_{n,max}^2} (\Psi_L - \Psi_{L,crit})} \quad (S.3.47b)$$

Combination of Eq. S.3.36-37, Eq. S.3.39, Eq. S.3.40c, and Eq. S.3.47b provides a solution for the integral in Eq. S.3.28,

$$\int_{\Psi_L}^{\Psi_{L,0}} \frac{dk_c}{d\epsilon} d\Psi = \left\{ \begin{aligned} & k_{c,max} \frac{A_n}{A_{n,max}} \frac{d\Psi_L}{d\epsilon} \\ & + \left[\frac{E}{k_{c,max}} + \frac{A_n}{A_{n,max}} (\Psi_{L,0} - \Psi_L) \right] \frac{dk_{c,max}}{d\epsilon} \\ & - \wp \left\{ \begin{aligned} & \frac{dE}{d\epsilon} + \left[k_c + k_{c,max} \left(1 - \frac{A_n}{A_{n,max}} \right) \right] \frac{d\Psi_L}{d\epsilon} \\ & + \left[\frac{E_{max}-E}{k_{c,max}} + \frac{A_n}{A_{n,max}} (\Psi_L - \Psi_{L,crit}) \right] \frac{dk_{c,max}}{d\epsilon} \end{aligned} \right\} + \frac{\wp_{crit}}{\lambda_{crit}} \frac{dI}{d\epsilon} \end{aligned} \right\} \quad (S.3.48a)$$

$$\Rightarrow \int_{\Psi_L}^{\Psi_{L,0}} \frac{dk_c}{d\epsilon} d\Psi = \mathfrak{h} k_c \frac{d\Psi_L}{d\epsilon} + \mathfrak{i} \frac{dk_{c,max}}{d\epsilon} - \wp \frac{dE}{d\epsilon} - \wp \frac{\wp_{crit}}{\lambda_{crit}} \frac{dI}{d\epsilon} \quad (S.3.48b)$$

where \wp and \mathfrak{h} are unitless terms, and \mathfrak{i} has units of pressure [MPa].

$$\wp = \frac{\lambda_{crit} k_{c,max} \frac{A_n}{A_{n,max}^2} (\Psi_{L,0} - \Psi_L)}{1 + \lambda_{crit} k_{c,max} \frac{A_n}{A_{n,max}^2} (\Psi_L - \Psi_{L,crit})} \quad (S.3.49)$$

$$\mathfrak{h} = \frac{k_{c,max}}{k_c} \frac{A_n}{A_{n,max}} - \wp \left[1 + \frac{k_{c,max}}{k_c} \left(1 - \frac{A_n}{A_{n,max}} \right) \right] \quad (S.3.50)$$

$$\mathfrak{i} = \frac{E}{k_{c,max}} + \frac{A_n}{A_{n,max}} (\Psi_{L,0} - \Psi_L) - \wp \left[\frac{E_{max}-E}{k_{c,max}} + \frac{A_n}{A_{n,max}} (\Psi_L - \Psi_{L,crit}) \right] \quad (S.3.51)$$

Combining Eq. S.3.48b and Eq. S.3.28 and rearranging completes our equation for $d\Psi_L/d\epsilon$,

$$(1 - \mathfrak{h}) \frac{d\Psi_L}{d\epsilon} = -\frac{1}{k_c} (1 + \wp) \frac{dE}{d\epsilon} + \frac{k_{c,max}}{k_c} \frac{d\Psi_{L,0}}{d\epsilon} + \frac{\mathfrak{i}}{k_c} \frac{dk_{c,max}}{d\epsilon} - \frac{\wp}{k_c} \frac{\wp_{crit}}{\lambda_{crit}} \frac{dI}{d\epsilon} \quad (S.3.52)$$

which is further combined with Eq. S.3.22d to complete our second definition of $d\Psi_S/d\epsilon$.

$$\frac{d\Psi_S}{d\epsilon} = \left\{ \begin{aligned} & \frac{1}{\mathfrak{d}} \left(\frac{1}{f_L k_L} - \frac{\mathfrak{e} (1 + \wp)}{k_c (1 - \mathfrak{h})} \right) \frac{dE}{d\epsilon} \\ & + \frac{\mathfrak{e}}{\mathfrak{d} (1 - \mathfrak{h})} \frac{1}{k_{c,max}} \frac{d\Psi_{L,0}}{d\epsilon} \\ & + \frac{\mathfrak{e}}{\mathfrak{d} (1 - \mathfrak{h})} \frac{1}{k_c} \frac{\mathfrak{i}}{dk_{c,max}} \frac{dk_{c,max}}{d\epsilon} \\ & - \frac{\mathfrak{e}}{\mathfrak{d} (1 - \mathfrak{h})} \frac{1}{k_c} \frac{\wp}{\lambda_{crit}} \frac{dI}{d\epsilon} \end{aligned} \right\} \quad (S.3.53)$$

Now with two definitions of $d\Psi_S/d\epsilon$, we combine Eq. S.3.21 and Eq. S.3.53 and rearrange for our final equation for $dE/d\epsilon$.

$$\frac{dE}{d\epsilon} = \frac{\left(\begin{aligned} & -\frac{E}{a} \left(\frac{b}{a_L c} + \frac{1}{f_S k_S} \right) \frac{da_L}{d\epsilon} \\ & + \frac{e}{d} \frac{1}{(h-1)k_c} \left(\frac{dk_{c,max}}{d\epsilon} + k_{c,max} \frac{d\Psi_{RC,0}}{d\epsilon} \right) \\ & - \frac{e}{d} \frac{1}{(h-1)k_c} \frac{\rho_{crit} dl}{d\epsilon} \\ & - \left(\frac{1}{a} + \frac{e}{d} \frac{1}{(h-1)k_c} \right) \varpi \rho g \frac{\partial H}{\partial \epsilon} + \frac{a_L E}{a f_S k_S^2} \frac{\partial k_S}{\partial \epsilon} \\ & - \frac{b}{a c} \sum_{j=1}^N \frac{E_j}{R_{R,j}} \frac{\partial R_{R,j}}{\partial \epsilon} \end{aligned} \right)}{\frac{1}{d} \left(\frac{1}{f_L k_L} + \frac{e}{k_c (h-1)} \right) + \frac{1}{a} \left(\frac{b}{c} + \frac{a_L}{f_S k_S} \right)} \quad (S.3.54)$$

Given the definition of k_c given by Eq. S.3.31j, the denominator in Eq. S.3.54 can be simplified and the total expression further simplifies to the following expression.

$$\frac{dE}{d\epsilon} = \frac{1}{h+g} \left\{ \begin{aligned} & -k_c \frac{E}{a_L} \frac{(h-1)}{e} \left(\frac{e}{k_c} - \frac{1}{f_L k_L} \right) \frac{da_L}{d\epsilon} + \frac{dk_{c,max}}{d\epsilon} + k_{c,max} \frac{d\Psi_{RC,0}}{d\epsilon} \\ & - \left[k_c (h-1) \frac{d}{ae} + k_{c,max} \right] \varpi \rho g \frac{\partial H}{\partial \epsilon} + k_c (h-1) \frac{d}{ae} \frac{a_L E}{f_S k_S^2} \frac{\partial k_S}{\partial \epsilon} \\ & - \frac{e}{d} \frac{\rho_{crit}}{\lambda_{crit}} \frac{dl}{d\epsilon} - k_c (h-1) \frac{d}{ace} \sum_{j=1}^N \frac{E_j}{R_{R,j}} \frac{\partial R_{R,j}}{\partial \epsilon} \end{aligned} \right\} \quad (S.3.55)$$

In Eq. S.3.54-55, recall that k_c refers to the optimal value of k_c determined through the *gain-risk* stomata optimization algorithm (i.e. k_c at the optimal or realized Ψ_L). Note that evaluating Eq. S.3.55 requires developing the entire supply curve (i.e. E for $\Psi_{L,0} \leq \Psi \leq \Psi_{L,crit}$) (Sperry & Love, 2015) for two reasons. First, the supply curve has to be formulated to find the optimal Ψ_L through the *gain-risk* algorithm (Sperry et al., 2017) and other relevant terms in Eq. S.3.54 that coincide with the optimal Ψ_L (e.g. k_c , a , b , c , d , e , etc.). Second, the entire supply curve is necessary to evaluate other terms in Eq. S.3.55 that coincide with $\Psi_{L,0}$ (e.g. $d\Psi_{RC,0}/d\epsilon$) and $\Psi_{L,crit}$ (e.g. λ_{crit} and ρ_{crit}). Eq. S.3.55 can be further simplified to represent the derivatives of E specific to either sapwood biomass ($\epsilon = D$), leaf biomass ($\epsilon = a_L$), or root biomass ($\epsilon = C_{R,H,i}$ or $\epsilon = C_{R,V,i}$). For sapwood, Eq. S.3.55 simplifies to

$$\frac{dE}{dD} = \frac{1}{h+g} \left\{ \begin{aligned} & - \left[k_c (h-1) \frac{d}{ae} + k_{c,max} \right] \varpi \rho g \frac{\partial H}{\partial D} + k_c (h-1) \frac{d}{ae} \frac{a_L E}{f_S k_S^2} \frac{\partial k_S}{\partial D} \\ & + \frac{dk_{c,max}}{dD} - \frac{e}{d} \frac{\rho_{crit}}{\lambda_{crit}} \left(\frac{\partial I}{\partial H} \frac{\partial H}{\partial D} + \frac{\partial I}{\partial W} \frac{\partial W}{\partial D} \right) \end{aligned} \right\} \quad (S.3.56)$$

where $\partial H/\partial D$ and $\partial W/\partial D$ terms were previously defined by Eq. S.1.5-6, $\partial I/\partial H$ and $\partial I/\partial W$ terms are later defined by Eq. S.5.4-5, and $\partial k_S/\partial D$ is defined later by Eq. S.4.8. For leaves, Eq. S.3.55 simplifies to

$$\frac{dE}{da_L} = \frac{1}{h+g} \left[-k_c \frac{E}{a_L} \frac{(h-1)}{e} \left(\frac{e}{k_c} - \frac{1}{f_L k_L} \right) + \frac{dk_{c,max}}{da_L} - \frac{e}{d} \frac{\rho_{crit}}{\lambda_{crit}} \frac{dl}{da_L} \right] \quad (S.3.57)$$

where $\partial I/\partial a_L$ is later defined by Eq. S.5.3. Given Eq. S.3.3-5, the partial derivatives of root resistance may be defined,

$$\frac{\partial R_{R,j}}{\partial C_{R,H,i}} = \begin{cases} -\frac{R_{R,H,j}}{C_{R,H,i}} & j = i \\ 0, & j \neq i \end{cases} \quad (S.3.58a)$$

$$\frac{\partial R_{R,j}}{\partial C_{R,V,i}} = \begin{cases} -\frac{R_{R,V,i}}{C_{R,V,i}}, & j \geq i \\ 0, & j < i \end{cases} \quad (\text{S.3.58b})$$

and Eq. S.3.55 simplifies for the two roots to

$$\frac{dE}{dC_{R,H,i}} = \frac{1}{\mathbb{h} + \mathbb{g}} \left[\mathbb{h} \frac{dk_{c,max}}{dC_{R,H,i}} + k_{c,max} \frac{d\Psi_{RC,0}}{dC_{R,H,i}} + (\mathbb{h} - 1) \frac{\mathbb{d}\mathbb{b}}{\mathbb{a}\mathbb{c}\mathbb{e}} \frac{k_c E_i}{C_{R,H,i}} \frac{R_{R,H,j}}{R_{R,i}} \right] \quad (\text{S.3.59a})$$

$$\frac{dE}{dC_{R,V,i}} = \frac{1}{\mathbb{h} + \mathbb{g}} \left[\mathbb{h} \frac{dk_{c,max}}{dC_{R,V,i}} + k_{c,max} \frac{d\Psi_{RC,0}}{dC_{R,V,i}} + (\mathbb{h} - 1) \frac{\mathbb{d}\mathbb{b}}{\mathbb{a}\mathbb{c}\mathbb{e}} \frac{k_c}{C_{R,V,i}} \left(\sum_{j=i}^N E_j \frac{R_{R,V,j}}{R_{R,j}} \right) \right] \quad (\text{S.3.59b})$$

where $d\Psi_{RC,0}/d\epsilon$ is solved by combining Eq. S.3.29 with Eq. S.3.58.

$$\frac{d\Psi_{RC,0}}{dC_{R,H,i}} = \frac{1}{\mathbb{c}_0} \frac{E_{0,i}}{C_{R,H,i}} \frac{R_{R,H,0,i}}{R_{R,0,i}} \quad (\text{S.3.60a})$$

$$\frac{d\Psi_{RC,0}}{dC_{R,V,i}} = \frac{1}{\mathbb{c}_0} \frac{1}{C_{R,V,i}} \left(\sum_{j=i}^N E_{0,j} \frac{R_{R,V,0,j}}{R_{R,0,j}} \right) \quad (\text{S.3.60b})$$

In Eq. S.3.54-55, Eq. S.3.56-57, and Eq. S.3.59, we have not yet explicitly defined any of the $dk_{c,max}/d\epsilon$ terms. These terms may be defined by differentiating Eq. S.3.32 and using the definitions provided by Eq. S.3.33-34 as well as the definition of \mathbb{c}_0 .

$$\frac{dk_{c,max}}{d\epsilon} = \left\{ \begin{aligned} & \frac{\partial k_{c,max}}{\partial f_{L,0}} \left(\frac{\partial f_{L,0}}{\partial \Psi_{RC,0}} \frac{d\Psi_{RC,0}}{d\epsilon} + \frac{\partial f_{L,0}}{\partial H} \frac{\partial H}{\partial \epsilon} \right) + \frac{\partial k_{c,max}}{\partial f_{S,0}} \left(\frac{\partial f_{S,0}}{\partial \Psi_{RC,0}} \frac{d\Psi_{RC,0}}{d\epsilon} + \frac{\partial f_{S,0}}{\partial H} \frac{\partial H}{\partial \epsilon} \right) + \frac{\partial k_{c,max}}{\partial \mathbb{c}_0} \frac{\partial \mathbb{c}_0}{\partial a_L} \frac{da_L}{d\epsilon} \\ & + \frac{\partial k_{c,max}}{\partial \mathbb{c}_0} \sum_{j=1}^N \left[\frac{\partial \mathbb{c}_0}{\partial R_{R,0,j}} \frac{\partial R_{R,0,j}}{\partial \epsilon} + \frac{\partial \mathbb{c}_0}{\partial R_{R,H,0,j}} \frac{\partial R_{R,H,0,j}}{\partial \epsilon} + \left(\frac{\partial \mathbb{c}_0}{\partial f_{R,0,j}} + \frac{\partial \mathbb{c}_0}{\partial R_{R,0,j}} \frac{\partial R_{R,0,j}}{\partial f_{R,0,j}} + \frac{\partial \mathbb{c}_0}{\partial R_{R,H,0,j}} \frac{\partial R_{R,H,0,j}}{\partial f_{R,0,j}} \right) \frac{\partial f_{R,0,j}}{\partial \Psi_{RC,0}} + \frac{\partial \mathbb{c}_0}{\partial \left(\frac{\partial f_{R,0,j}}{\partial \Psi_{RC,0}} \right)} \frac{d \left(\frac{\partial f_{R,0,j}}{\partial \Psi_{RC,0}} \right)}{d\epsilon} \right] \frac{d\Psi_{RC,0}}{d\epsilon} \\ & + \frac{\partial k_{c,max}}{\partial a_L} \frac{da_L}{d\epsilon} + \frac{\partial k_{c,max}}{\partial k_S} \frac{dk_S}{d\epsilon} \end{aligned} \right\} \quad (\text{S.3.61a})$$

$$\Rightarrow \frac{dk_{c,max}}{d\epsilon} = \left\{ \begin{aligned} & \left[\frac{\partial k_{c,max}}{\partial f_{L,0}} \frac{\partial f_{L,0}}{\partial \Psi_{RC,0}} + \frac{\partial k_{c,max}}{\partial f_{S,0}} \frac{\partial f_{S,0}}{\partial \Psi_{RC,0}} \right] \frac{d\Psi_{RC,0}}{d\epsilon} \\ & + \frac{\partial k_{c,max}}{\partial \mathbb{c}_0} \sum_{j=1}^N \left[\left(\frac{\partial \mathbb{c}_0}{\partial f_{R,0,j}} + \frac{\partial \mathbb{c}_0}{\partial R_{R,0,j}} \frac{\partial R_{R,0,j}}{\partial f_{R,0,j}} + \frac{\partial \mathbb{c}_0}{\partial R_{R,H,0,j}} \frac{\partial R_{R,H,0,j}}{\partial f_{R,0,j}} \right) \frac{\partial f_{R,0,j}}{\partial \Psi_{RC,0}} + \frac{\partial \mathbb{c}_0}{\partial \left(\frac{\partial f_{R,0,j}}{\partial \Psi_{RC,0}} \right)} \frac{d \left(\frac{\partial f_{R,0,j}}{\partial \Psi_{RC,0}} \right)}{d\epsilon} \right] \frac{d\Psi_{RC,0}}{d\epsilon} \\ & + \left(\frac{\partial k_{c,max}}{\partial f_{L,0}} \frac{\partial f_{L,0}}{\partial H} + \frac{\partial k_{c,max}}{\partial f_{S,0}} \frac{\partial f_{S,0}}{\partial H} \right) \frac{\partial H}{\partial \epsilon} \\ & + \left(\frac{\partial k_{c,max}}{\partial a_L} + \frac{\partial k_{c,max}}{\partial \mathbb{c}_0} \frac{\partial \mathbb{c}_0}{\partial a_L} \right) \frac{da_L}{d\epsilon} \\ & + \frac{\partial k_{c,max}}{\partial k_S} \frac{dk_S}{d\epsilon} \\ & + \frac{\partial k_{c,max}}{\partial \mathbb{c}_0} \sum_{j=1}^N \left(\frac{\partial \mathbb{c}_0}{\partial R_{R,0,j}} \frac{\partial R_{R,0,j}}{\partial \epsilon} + \frac{\partial \mathbb{c}_0}{\partial R_{R,H,0,j}} \frac{\partial R_{R,H,0,j}}{\partial \epsilon} \right) \end{aligned} \right\} \quad (\text{S.3.61b})$$

$$\Rightarrow \frac{\partial k_{c,max}}{\partial f_{L,0}} = \frac{k_{c,max}^2}{k_L f_{L,0}^2} \quad (\text{S.3.61c})$$

$$\Rightarrow \frac{\partial k_{c,max}}{\partial \mathbb{c}_0} = \frac{k_{c,max}^2}{\mathbb{c}_0^2} \quad (\text{S.3.61d})$$

$$\Rightarrow \frac{\partial k_{c,max}}{\partial a_L} = -\frac{k_{c,max}^2}{k_S f_{S,0}} \quad (\text{S.3.61e})$$

$$\Rightarrow \frac{\partial k_{c,max}}{\partial k_S} = \frac{a_L k_{c,max}^2}{k_S^2 f_{S,0}} \quad (\text{S.3.61f})$$

$$\Rightarrow \frac{\partial k_{c,max}}{\partial f_{S,0}} = \frac{a_L k_{c,max}^2}{k_S f_{S,0}^2} \quad (\text{S.3.61g})$$

$$\Rightarrow \frac{\partial c_0}{\partial f_{R,0,j}} = \frac{E_{0,j}}{f_{R,0,j}^2} \frac{R_{R,H,0,j}}{R_{R,0,j}} \frac{\partial f_{R,0,j}}{\partial \Psi_{Rc}} \quad (\text{S.3.61h})$$

$$\Rightarrow \frac{\partial c_0}{\partial a_L} = -\frac{1}{a_L^2} \sum_{j=1}^N \frac{1}{R_{R,0,j}} \quad (\text{S.3.61i})$$

$$\Rightarrow \frac{\partial c_0}{\partial R_{R,0,j}} = \frac{1}{R_{R,0,j}^2} \left(E_{0,j} \frac{R_{R,H,0,j}}{f_{R,0,j}} \frac{\partial f_{R,0,j}}{\partial \Psi_{Rc}} - \frac{1}{a_L} \right) \quad (\text{S.3.61j})$$

$$\Rightarrow \frac{\partial R_{R,0,j}}{\partial f_{R,0,j}} = -\frac{R_{R,H,0,j}}{f_{R,0,j}} \quad (\text{S.3.61k})$$

$$\Rightarrow \frac{\partial c_0}{\partial R_{R,H,0,j}} = -\frac{E_{0,j}}{f_{R,0,j} R_{R,0,j}} \frac{\partial f_{R,0,j}}{\partial \Psi_{Rc}} \quad (\text{S.3.61l})$$

$$\Rightarrow \frac{\partial R_{R,H,0,j}}{\partial f_{R,0,j}} = \frac{\partial R_{R,0,j}}{\partial f_{R,0,j}} = -\frac{R_{R,H,0,j}}{f_{R,0,j}} \quad (\text{S.3.61m})$$

$$\Rightarrow \frac{\partial c_0}{\partial \left(\frac{\partial f_{R,0,j}}{\partial \Psi_{Rc,0}} \right)} = -\frac{E_{0,j}}{f_{R,0,j}} \frac{R_{R,H,0,j}}{R_{R,0,j}} \quad (\text{S.3.61n})$$

$$\Rightarrow \frac{d \left(\frac{\partial f_{R,0,j}}{\partial \Psi_{Rc,0}} \right)}{d \Psi_{Rc,0}} = \frac{\partial^2 f_{R,0,j}}{\partial \Psi_{Rc,0}^2} + \frac{\partial \left(\frac{\partial f_{R,0,j}}{\partial \Psi_{Rc,0}} \right)}{\partial f_{R,0,j}} \frac{\partial f_{R,0,j}}{\partial \Psi_{Rc,0}} + \frac{\partial \left(\frac{\partial f_{R,0,j}}{\partial \Psi_{Rc,0}} \right)}{\partial (VC_R(\Psi_{Rc}))} \frac{\partial (VC_R(\Psi_{Rc}))}{\partial \Psi_{Rc,0}} \quad (\text{S.3.61o})$$

$$\Rightarrow \frac{d \left(\frac{\partial f_{R,0,j}}{\partial \Psi_{Rc,0}} \right)}{d \Psi_{Rc,0}} = \begin{cases} \frac{2 \frac{\partial f_{R,0,j}}{\partial \Psi_{Rc,0}} \frac{\partial VC_R(\Psi_{Rc})}{\partial \Psi_{Rc}}}{\Psi_{soil,i} - \Psi_{Rc,0}}, & \Psi_{soil,j} \neq \Psi_{Rc,0} \\ \frac{1}{3} \frac{\partial^2 VC_R(\Psi_{Rc})}{\partial \Psi_{Rc}^2}, & \Psi_{soil,j} = \Psi_{Rc,0} \end{cases} \quad (\text{S.3.61p})$$

$$\Rightarrow \frac{\partial f_{L,0}}{\partial \Psi_{Rc,0}} = \frac{\partial VC_L(\Psi_{Rc,0} - \varpi \rho g H)}{\partial (\Psi_{Rc,0} - \varpi \rho g H)} \quad (\text{S.3.61q})$$

$$\Rightarrow \frac{\partial f_{L,0}}{\partial H} = -\varpi \rho g \frac{\partial VC_L(\Psi_{Rc,0} - \varpi \rho g H)}{\partial (\Psi_{Rc,0} - \varpi \rho g H)} = -\varpi \rho g \frac{\partial f_{L,0}}{\partial \Psi_{Rc,0}} \quad (\text{S.3.61r})$$

$$\Rightarrow \frac{\partial f_{S,0}}{\partial \Psi_{Rc,0}} = \frac{VC_S(\Psi_{Rc,0}) - VC_S(\Psi_{Rc,0} - \varpi \rho g H)}{\varpi \rho g H} \quad (\text{S.3.61s})$$

$$\Rightarrow \frac{\partial f_{S,0}}{\partial H} = \frac{VC_S(\Psi_{Rc,0} - \varpi \rho g H) - f_{S,0}}{H} \quad (\text{S.3.61t})$$

$$\Rightarrow \frac{dk_{c,max}}{d\epsilon} = k_{c,max}^2 \left\{ \begin{aligned} & \frac{a_L}{k_S^2 f_{S,0}} \frac{dk_S}{d\epsilon} + \left(\frac{\partial f_{L,0}}{k_L f_{L,0}^2} + a_L \frac{\partial f_{S,0}}{k_S f_{S,0}^2} \right) \frac{d \Psi_{Rc,0}}{d\epsilon} \\ & + \frac{1}{c_0^2} \sum_{j=1}^N \left[\left(2 \frac{E_{0,j}}{f_{R,0,j}^2} \frac{R_{R,H,0,j}}{R_{R,0,j}} \frac{\partial f_{R,0,j}}{\partial \Psi_{Rc}} - \frac{R_{R,H,0,j}}{f_{R,0,j} R_{R,0,j}} \left(E_{0,j} \frac{R_{R,H,0,j}}{f_{R,0,j}} \frac{\partial f_{R,0,j}}{\partial \Psi_{Rc}} - \frac{1}{a_L} \right) \right) \frac{\partial f_{R,0,j}}{\partial \Psi_{Rc,0}} - \frac{E_{0,j}}{f_{R,0,j}} \frac{R_{R,H,0,j}}{R_{R,0,j}} \frac{d \left(\frac{\partial f_{R,0,j}}{\partial \Psi_{Rc,0}} \right)}{d \Psi_{Rc,0}} \right] \frac{d \Psi_{Rc,0}}{d\epsilon} \\ & + \left(\frac{\partial f_{L,0}}{k_L f_{L,0}^2} + a_L \frac{\partial f_{S,0}}{k_S f_{S,0}^2} \right) \frac{\partial H}{\partial \epsilon} + \left(\frac{1}{k_S f_{S,0}} - \frac{1}{c_0^2 a_L^2} \sum_{j=1}^N \frac{1}{R_{R,0,j}} \right) \frac{da_L}{d\epsilon} \\ & + \frac{1}{c_0^2} \sum_{j=1}^N \left[\frac{1}{R_{R,0,j}^2} \left(E_{0,j} \frac{R_{R,H,0,j}}{f_{R,0,j}} \frac{\partial f_{R,0,j}}{\partial \Psi_{Rc}} - \frac{1}{a_L} \right) \frac{\partial R_{R,0,j}}{\partial \epsilon} - \frac{E_{0,j}}{f_{R,0,j} R_{R,0,j}} \frac{\partial f_{R,0,j}}{\partial \Psi_{Rc}} \frac{\partial R_{R,H,0,j}}{\partial \epsilon} \right] \end{aligned} \right\} \quad (\text{S.3.61u})$$

For sapwood, leaf, and the two root pools, Eq. S.3.61u simplifies to the following expressions for $dk_{c,max}/dD$, $dk_{c,max}/da_L$, $dk_{c,max}/dC_{R,H,i}$, and $dk_{c,max}/dC_{R,V,i}$ given Eq. S.3.58.

$$\frac{dk_{c,max}}{dD} = k_{c,max}^2 \left[\left(\frac{\partial f_{L,0}}{k_L f_{L,0}^2} + a_L \frac{\partial f_{S,0}}{k_S f_{S,0}^2} \right) \frac{\partial H}{\partial D} + \frac{a_L}{k_S^2 f_{S,0}} \frac{dk_S}{dD} \right] \quad (\text{S.3.62})$$

$$\frac{dk_{c,max}}{da_L} = k_{c,max}^2 \left(\frac{1}{k_{sf,s,0}} - \frac{1}{c_0^2 a_L^2} \sum_{j=1}^N \frac{1}{R_{R,0,j}} \right) \quad (S.3.63)$$

$$\frac{dk_{c,max}}{dC_{R,H,i}} = k_{c,max}^2 \left\{ + \frac{1}{c_0^2} \sum_{j=1}^N \left\{ \left[2 \frac{E_{0,j}}{f_{R,0,j}^2} \frac{R_{R,H,0,j}}{R_{R,0,j}} \frac{\partial f_{R,0,j}}{\partial \Psi_{RC}} + \frac{R_{R,H,0,j}}{f_{R,0,j} R_{R,0,j}^2} \left(\frac{1}{a_L} - E_{0,j} \frac{R_{R,H,0,j}}{f_{R,0,j}} \frac{\partial f_{R,0,j}}{\partial \Psi_{RC}} \right) \right] \frac{\partial f_{R,0,j}}{\partial \Psi_{RC,0}} - \frac{E_{0,j}}{f_{R,0,j}} \frac{R_{R,H,0,j}}{R_{R,0,j}} \frac{d \left(\frac{\partial f_{R,0,j}}{\partial \Psi_{RC,0}} \right)}{d \Psi_{RC,0}} \right\} \right. \quad (S.3.64)$$

$$\left. + \frac{1}{c_0^2} \frac{1}{C_{R,H,i}} \frac{R_{R,H,0,i}}{R_{R,0,i}^2} \left(\frac{1}{a_L} + E_{0,i} \frac{R_{R,0,i} - R_{R,H,0,i}}{f_{R,0,i}} \frac{\partial f_{R,0,i}}{\partial \Psi_{RC}} \right) \right\} \left(\frac{\frac{\partial f_{L,0}}{\partial \Psi_{RC,0}}}{k_L f_{L,0}^2} + a_L \frac{\frac{\partial f_{S,0}}{\partial \Psi_{RC,0}}}{k_S f_{S,0}^2} \right) \frac{d \Psi_{RC,0}}{d C_{R,H,i}} \right\} \quad (S.3.65)$$

S.4 Scaling of Stem Conductances with Tree Size

The scaling of stem xylem conductance, k_S [$\text{mol H}_2\text{O} \cdot \text{s}^{-1} \cdot \text{MPa}^{-1}$], with tree size is modeled in THORP by an assumed fractal-like hydraulic tree architecture (West et al., 1999; Savage et al., 2010; Sperry et al. 2012; Hölttä et al., 2013) that accounts for the volumes of both sapwood and heartwood. In this section, we derive the general equation which THORP uses to capture the change in stem conductance with size. Stem conductance is represented as a series of conductors connected in-parallel radially and connected in-series axially. We represent the total conductance as the following equation, in which $K_S(x)$ is the xylem conductivity [$\text{mol H}_2\text{O} \cdot \text{m} \cdot \text{s}^{-1} \cdot \text{MPa}^{-1}$] at a distance x [m] from the apex.

$$(k_S)^{-1} = \int_0^H (K_S(x))^{-1} dx \quad (S.4.1)$$

The xylem conductivity of an individual branch is given by the Hagen–Poiseuille equation integrated radially from the heartwood-sapwood transition of the branch, $d_i(x)$ [m], and the outer diameter, $d(x)$ [m], for a branch at a distance x from the apex. Note that $d(H) = D$ and $d_i(H) = D_i$, where D and D_i are the trunk diameter and diameter of the heartwood-sapwood transition at the base of the tree [m], respectively, which THORP tracks continuously through simulation (see Section S.1 for assumed tree allometry). The total xylem conductivity at x is approximated as the conductivity of a single branch multiplied by $(H/x)^2$ to account for the in-parallel flow across multiple branches (Hölttä et al., 2013; their Eq. A1), assuming that sapwood area is conserved. We express this formation as a proportionality rather than an equality, and all proportionality constants are lumped together as a single term. The lumped proportionality constant represents multiple mechanisms, including viscosity and the additional resistances from inter-vessel pitting and pit membranes that are not accounted for in the Hagen–Poiseuille equation. The lumped proportionality additionally accounts for the individual proportionalities for subsequently-assumed scaling laws (taper and packing).

$$K_S(x) \propto \left(\frac{H}{x} \right)^2 \int_{d_t(x)/2}^{d(x)/2} R_x(r)^4 N_x(r) r dr \quad (S.4.2)$$

R_x is the xylem conduit radius, and N_x is the number of xylem conduits. The additional multiplier of r is present to convert from Cartesian to polar coordinates. According to taper and packing functions, R_x and N_x scale as power functions of r (Savage et al., 2010; Sperry et al. 2012). The theoretical taper and packing functions that optimize space filling are R_x proportional to $r^{1/3}$ and N_x proportional to r^{-2} ,

respectively (Savage et al., 2010). However, we wish not to constrain the exact values of the exponents relating R_x and N_x to r , since empirical values of the taper and packing exponents may not converge on their optimal values (von Allmen et al., 2012). We replace the $R_x^4 N_x r$ proportionality with a single power-law function of r with dummy scaling-exponent, β ,

$$K_S(x) \propto \left(\frac{H}{x}\right)^2 \int_{d_t(x)/2}^{d(x)/2} r^\beta dr \quad (\text{S.4.3})$$

which simplifies to the following expression for $K_S(x)$ upon integration.

$$K_S(x) \propto \left(\frac{H}{x}\right)^2 [d(x)^{\beta+1} - d_t(x)^{\beta+1}] \quad (\text{S.4.4})$$

We further assume that sapwood area is conserved along the height of the tree ($d_t(x)/d(x) = D_t/D$; Shinozaki et al., 1964; Horn, 2000; von Allmen et al., 2012) and that branch diameter approximately scales linearly with distance from apex, $d(x) \propto x$ (Hölttä et al., 2013; Mäkelä et al., 2019), or at least for Scots Pine for which we have parameterized THORP in our validation in the main text. This linear scaling of branch diameter with x does not entirely agree with THORP's power-law scaling of tree height, H , with basal diameter, D ($\log(H) \propto c_0 \log(D)$; see Section S.1). However, we have chosen this representation, because it better captures the concentration of hydraulic resistances near the apex which dominates in the total stem resistance. Combining Eq. S.4.1 and Eq. S.4.4 and integrating leads to

$$k_S \propto H^\beta \left[1 - \left(\frac{D_t}{D}\right)^{\beta+1}\right] \quad (\text{S.4.5})$$

which upon replacement of H with its equivalent D (recall $\log(H) \propto c_0 \log(D)$), further simplifies to the following proportionality.

$$k_S \propto D^{\beta c_0} \left[1 - \left(\frac{D_t}{D}\right)^{\beta+1}\right] \quad (\text{S.4.6})$$

We replace the dummy exponent, β , with c_2/c_0 , where c_2 is a new scaling exponent that describes how stem conductance scales with basal diameter when there is no heartwood ($\log(k_S) \propto c_2 \log(D)$ when $D_t = 0$ m). We also remove the proportionality by adding a lumped proportionality constant, b_2 [$\text{mol H}_2\text{O} \cdot \text{s}^{-1} \cdot \text{MPa}^{-1}$], and a reference diameter, $D_{ref} = 1$ m, for dimensional consistency.

$$k_S = b_2 \left(\frac{D}{D_{ref}}\right)^{c_2} \left[1 - \left(\frac{D_t}{D}\right)^{\frac{c_2}{c_0}+1}\right] \quad (\text{S.4.7})$$

We recognize that our assumption of uniform heartwood fraction along the stem (i.e. $d_t(x)/d(x) = D_t/D$) is unconventional and is only intended to simplify our approximate solution for hydraulic conductance. It is possible to consider non-uniform heartwood distributions by power-law scaling functions of branch diameter (Sperry et al., 2012; von Allmen et al., 2012; Hölttä et al., 2013). Such added detail would make branch segments closest to the apex (where there should be proportionally less heartwood) more conductive than currently modeled. However, the current model effectively assumes infinite apex branches (recall previously assuming the number of branches equals $(H/x)^2$) which likely overestimates their contribution to the whole-stem conductance. The latter assumption likely (at least partially) compensates for the lack of the former.

We estimated b_2 for Scots Pine by fitting Eq. S.4.7 to whole-tree stem conductance data from Mencuccini and Grace (1996) by ordinary-least squares regression assuming fixed values for c_0 and c_2 . Mencuccini and Grace's (1996) conductance measurements include the effects of embolism, so we

calculated the maximum stem conductance from their reported values assuming a 10% loss conductance at field conditions based on Torres-Ruiz et al. (2016) for Scots Pine. We fixed c_0 at 0.64, which is the slope regressed when plotting $\log(H)$ against $\log(D)$ for Scots Pine using H and D data from the Hyytiälä, Kroof, and Peitz PROFOUND (Reyer et al., 2019) sites and from Mencuccini & Grace (1996). This value of c_0 agrees nicely with the theoretical value of $\frac{2}{3}$ based on elastic similarity and Euler buckling (McMahon, 1973; Niklas & Spatz, 2004). We fixed c_2 so that $k_S \propto H^{1.45}$ for Scots Pine when no heartwood is present based on Hölttä et al. (2013; see their Table 4; i.e. $c_2 = 1.45 \cdot c_0$). We regressed b_2 as the slope of two transformed axes, Y and X , where $Y = k_S/[1 - (D_t/D)^{\beta+1}]$ is the expected conductance if there were no heartwood and the entire stem was conductive ($D_t = 0$ m), where again $\beta = c_2/c_0$, and $X = (D/D_{ref})^{c_2}$. The diameter of the heartwood-sapwood transition, D_t , was estimated from stem- and sapwood- basal areas reported by Mencuccini and Grace (1996). A comparison of the observed and modeled stem conductances are shown in Figure S13.

The derivative of maximum stem conductance, k_S (Eq. S.4.7), with respect to basal diameter simplifies to the following expression which will be used later in Section S.8 to calculate allocation fractions and was previously denoted in Section S.3 (particularly through Eq. S.3.28).

$$\frac{dk_S}{dD} = \frac{c_2 + \left(\frac{c_2}{c_0} + 1 - c_2\right) \left(\frac{D_t}{D}\right)^{\frac{c_2}{c_0} + 1}}{1 - \left(\frac{D_t}{D}\right)^{\frac{c_2}{c_0} + 1}} \frac{k_S}{D} \quad (\text{S.4.8})$$

S.5 Light Interception

Light interception of an individual tree is modeled in THORP as a simple form of the Beer-Lambert law for a canopy of uniform spatial distribution of leaf area similar to the formulation used by Buckley and Roberts (2006a,b). The target tree's canopy at height, H , sits below an overstory canopy with height, H_n , that shades the target tree and represents aboveground competition. Similar to the target tree, the leaves of the overstory are approximated as uniformly distributed between H_n and H . Additionally, we apply the perfect plasticity approximation (Strigul et al., 2008) such that the stand density is equal to W^2 . The absorbed light is represented by the leaf area-averaged solar insolation, I [$\text{W} \cdot \text{m}^{-2}$], given by

$$I = I_s \frac{W^2}{a_L} \cos(\Phi) e^{-K_n \max(0, H_n - H) \sec(\Phi)} \left(1 - e^{-\frac{\kappa_L a_L}{\phi W^2} \sec(\Phi)}\right) \quad (\text{S.5.1})$$

where I_s is the incoming insolation [$\text{W} \cdot \text{m}^{-2}$], Φ is the solar elevation below the zenith [-], κ_L is a dimensionless canopy extinction coefficient [-], ϕ is the ratio of total- to projected-leaf area [-] ($\text{LAI} = a_L \cdot \phi^{-1} \cdot W^{-2}$ by the perfect plasticity approximation; Strigul et al., 2008), which is here treated as a constant, and K_n is the effective extinction coefficient relative to path length of beams passing through neighboring trees [m^{-1}] defined in part by the overstory's total leaf area index, L_n [-].

$$K_n = \kappa_L \frac{L_n}{H_n} \quad (\text{S.5.2})$$

Solar zenith angles are estimated from the site's latitude, declination from the sun, and the hour-angle ignoring right ascension.

The derivatives of light capture, I , with respect to leaf area, height, and canopy width simplify to the following expressions which will be used later in Section S.8 to calculate allocation fractions.

$$\frac{dI}{da_L} = -\frac{1}{a_L} \left(I - I_s \frac{\kappa_L}{\varphi} e^{-\left[\kappa_n \max(0, H_n - H) + \frac{\kappa_L a_L}{\varphi W^2} \right] \sec(\Phi)} \right) \quad (\text{S.5.3})$$

$$\frac{\partial I}{\partial H} = \begin{cases} K_n I \sec(\Phi), & H_n > H \\ 0 & H_n \leq H \end{cases} \quad (\text{S.5.4})$$

$$\frac{\partial I}{\partial W} = \frac{2}{W} \left(I - I_s \frac{\kappa_L}{\varphi} e^{-\left[\kappa_n \max(0, H_n - H) + \frac{\kappa_L a_L}{\varphi W^2} \right] \sec(\Phi)} \right) \quad (\text{S.5.5})$$

S.6 Photosynthesis and *Gain-Risk* Stomata Optimization

The net assimilation rate, A_n [$\text{mol C} \cdot \text{m}^{-2} \cdot \text{s}^{-1}$], is given by two expressions. The first expression describes the supply-limited rate of CO_2 diffusion through stomata and is defined by the conductance, G_c [$\text{mol CO}_2 \cdot \text{m}^{-2} \cdot \text{s}^{-1} \cdot \text{kPa}^{-1}$] ($G_c = G_w/1.6$, where G_w was introduced in Eq. S.3.10), and the concentration gradient between the atmosphere and the intercellular leaf space, $c_a - c_i$ [kPa]. The second expression describes the demand-limited rate of biochemical CO_2 uptake. The latter is defined by the difference between the hyperbolic minimum of a RuBP carboxylation-limited and an electron transport-limited gross rates, A_j and A_c [$\text{mol C} \cdot \text{m}^{-2} \cdot \text{s}^{-1}$], respectively, and the leaf dark respiration, R_d [$\text{mol C} \cdot \text{m}^{-2} \cdot \text{s}^{-1}$].

$$A_n = G_c(c_a - c_i) = \frac{A_j + A_c - \sqrt{(A_j + A_c)^2 - 4c'A_jA_c}}{2c'} - R_d \quad (\text{S.6.1})$$

The smoothness of the hyperbolic minimum is controlled by a curvature factor, $c' = 0.98$. Dark respiration is temperature-dependent according to de Pury and Farquhar (1997; $R_d = 0.01 \cdot V_{c,max}$, where $V_{c,max}$ is the maximum carboxylation rate [$\text{mol C} \cdot \text{m}^{-2} \cdot \text{s}^{-1}$], which is temperature-dependent following Eq. 1 in Harley & Baldocchi, 1995).

Both A_j and A_c depend on intercellular leaf CO_2 concentrations, c_i [kPa], by Michaelis-Menten functions (Farquhar et al., 1980)

$$A_c = V_{c,max} \frac{c_i - \Gamma^*}{c_i + K_c \left(1 + \frac{o_a}{K_o} \right)} \quad (\text{S.6.2})$$

$$A_j = \frac{J}{4} \frac{c_i - \Gamma^*}{c_i + 2\Gamma^*} \quad (\text{S.6.3})$$

where $V_{c,max}$ is the maximum carboxylation rate [$\text{mol C} \cdot \text{m}^{-2} \cdot \text{s}^{-1}$], J is the electron transport rate [$\text{mol e}^- \cdot \text{m}^{-2} \cdot \text{s}^{-1}$], Γ^* is the CO_2 compensation point [kPa], o_a is the atmospheric oxygen concentration [kPa], and K_c and K_o are Michaelis-Menten constant for carboxylation and oxygenation [kPa], respectively. The electron transport rate is given by the hyperbolic minimum of a biochemical maximum rate and a light-limited rate, J_{max} and J_l [$\text{mol e}^- \cdot \text{m}^{-2} \cdot \text{s}^{-1}$], respectively, where $J_l = \kappa \cdot I$, and κ is a proportionality constant between electron-transport rate and absorbed interception [$\text{mol C} \cdot \text{J}^{-1}$] ($\kappa \approx 6.90 \cdot 10^{-7} \text{ mol C} \cdot \text{J}^{-1}$ for a quantum yield of $0.3 \text{ mol photon} \cdot (\text{mol e}^-)^{-1}$ and an average PAR wavelength of 550 nm).

$$J = \frac{J_{max} + J_l - \sqrt{(J_{max} + J_l)^2 - 4c''J_{max}J_l}}{2c''} \quad (\text{S.6.4})$$

The smoothness of this hyperbolic minimum is controlled by another curvature factor, $c'' = 0.90$. The temperature-dependence of both $V_{c,max}$ and J_{max} were modeled using Eq. 1 in Harley and Baldocchi (1995).

The coupling of xylem hydraulics (Section S.3) and photosynthesis (Eq. S.6.1-4) suffers from a closure problem, namely the selection of xylem water potentials and stomatal conductances, G_w and G_c , at

which to evaluate transpiration, E , and photosynthesis, A_n . THORP closes this problem by implementing Sperry et al.'s (2017) *Gain-Risk* algorithm, which assumes that stomata are assumed maximize photosynthesis while simultaneously minimizing the risk of hydraulic damage (Wolf et al., 2016), and this cost minimization is formulated by maximizing whole-tree conductance (Sperry et al., 2017). The *Gain-Risk* algorithm enables for a simultaneous solution of the unknowns, particularly Ψ_L , E , G_w , G_c , c_i , and A_n . The *Gain-Risk* algorithm has been validated at the individual scale in garden experiments (Venturas et al., 2018; Wang et al., 2019) and at the ecosystem level (Sabot et al., 2019). The *Gain-Risk* framework is described in full detail in Sperry et al. (2017), to which we refer readers. In short, the *Gain-Risk* algorithm develops first a supply curve of transpiration values as function of potential leaf water potentials, $E(\Psi_L)$ (Sperry & Love 2015; Sperry et al. 2016), and second a gain curve of photosynthesis values as function of potential leaf water potentials, $A_n(\Psi_L)$. From the supply curve, whole-tree conductances are represented by the canopy conductance, $k_c = -dE/d\Psi_L$ (Eq. S.3.32). Both conductance and gain curves are normalized by their maximum values, and the optimal Ψ_L is selected as the Ψ_L that maximizes the sum of the normalized conductance and gain curves (Eq. S.3.35a; with solution for k_c that simultaneously meets the two definitions given by Eq. S.3.32 and Eq. S.3.35d).

Light-limitations and competition drive more aboveground growth in THORP. This is partially driven by the magnitude of marginal light-use efficiency, $\wp = \partial A_n / \partial I$ [mol C·J⁻¹], which represents the expected gain in productivity for a given increase in light capture (see Section S.8). Generally, \wp is large when photosynthesis is light-limited, and \wp declines as photosynthesis becomes more limited by physiological electron transport rates (i.e. J_{max}) or more limited by carboxylation (i.e. A_c). We evaluate \wp by the chain rule similar to the approach of Buckley et al. (2002; their Eq. A26-27).

$$\wp = \frac{\partial A_n}{\partial I} = \frac{\partial A_n}{\partial A_j} \frac{\partial A_j}{\partial J} \frac{\partial J}{\partial J_I} \frac{\partial J_I}{\partial I} \quad (\text{S.6.5})$$

The first of the terms on the right-hand side of Eq. S.6.5, $\partial A_n / \partial A_j$, is evaluated by differentiation of Eq. S.6.1.

$$\frac{\partial A_n}{\partial A_j} = \frac{1}{2c'} \left[1 - \frac{A_j + (1-2c')A_c}{\sqrt{(A_j + A_c)^2 - 4c'A_jA_c}} \right] \quad (\text{S.6.6})$$

The second of the terms on the right-hand side of Eq. S.6.5, $\partial A_j / \partial J$, is evaluated by differentiation of Eller et al.'s (2018) analytical solution for A_j (Eq. S3.8a in their Supplementary Info), which we have reproduced below.

$$A_j = \mathcal{H} - \sqrt{\mathcal{H}^2 - \mathcal{U}G_c} \quad (\text{S.6.7})$$

$$\mathcal{H} = \frac{\frac{J}{4} + G_c(c_a + 2\Gamma^*) - R_d}{2} \quad (\text{S.6.8})$$

$$\mathcal{U} = \frac{J}{4}(c_a - \Gamma^*) - R_d(c_a + 2\Gamma^*) \quad (\text{S.6.9})$$

$$\frac{\partial A_j}{\partial J} = \frac{1}{8} \frac{G_c(c_a - \Gamma^*) - A_j}{\sqrt{\mathcal{H}^2 - \mathcal{U}G_c}} = \frac{1}{8} \frac{G_c(c_a - \Gamma^*) - A_j}{\mathcal{H} - A_j} \quad (\text{S.6.10})$$

The third of the terms on the right-hand side of Eq. S.6.5, $\partial J / \partial J_I$, is evaluated by differentiation of Eq. S.6.4.

$$\frac{\partial J}{\partial J_I} = \frac{1}{2c''} \left[1 - \frac{J_I + (1-2c'')J_{max}}{\sqrt{(J_I + J_{max})^2 - 4c''J_IJ_{max}}} \right] \quad (\text{S.6.11})$$

The fourth and final term on the right-hand side of Eq. S.6.5, $\partial J_I / \partial I$ is equal to κ by its definition ($J_I = \kappa \cdot I$).

The marginal water use efficiency, $\lambda = \partial A_n / \partial E$ [mol C·(mol H₂O)⁻¹] (Cowan & Farquhar, 1977; though we adopt the notation of Hari et al., 1986), which THORP uses to predict allocation to hydraulic structures (Givnish, 1986; see Section S.8), was not explicitly formalized within Sperry et al.'s (2017) development of the *Gain-Risk* algorithm. Consistent with the approaches of Givnish (1986) and Novick et al. (2016), we interpret λ from the supply function, $E(\Psi_L)$ (Sperry & Love 2015; Sperry et al. 2016), and the gain function, $A_n(\Psi_L)$ (Manzoni et al., 2011), as $\lambda = (\partial A_n / \partial \Psi_L) / (\partial E / \partial \Psi_L)$ evaluated at the optimal Ψ_L predicted by the *Gain-Risk* algorithm. Though consistent with these past studies due to similar assumptions, our approach is different in practice, however. Rather than estimate λ directly from the supply and gain functions by finite-difference (i.e. $\lambda \approx \Delta A_n / \Delta E$), we calculate λ according to Buckley et al.'s (2017) Eq. 4, the derivation for which makes the same assumptions as the model presented here (e.g. zero mesophyll resistance, invariant with leaf temperature, etc.) and which is an analytical solution for $\lambda = (\partial A_n / \partial \Psi_L) / (\partial E / \partial \Psi_L) = (\partial A_n / \partial G_w) / (\partial E / \partial G_w)$. This approach was chosen so that the solution for λ would be independent of the numerical resolution of the supply function, which may become coarser and less refined at increasingly negative leaf water potentials. Nevertheless, the two calculations for λ agree well. Buckley et al.'s (2017) solution for λ under our simplifications is

$$\lambda = \frac{A_n}{E} \frac{\Xi}{\Xi + G_c} \quad (\text{S.6.12})$$

where

$$\Xi = \frac{\partial A_n}{\partial c_i} = \frac{\partial A_n}{\partial A_c} \frac{\partial A_c}{\partial c_i} + \frac{\partial A_n}{\partial A_j} \frac{\partial A_j}{\partial c_i} \quad (\text{S.6.13})$$

in which $\partial A_n / \partial A_j$ has already been defined in Eq. S.6.6, and the remaining terms can be solved by differentiating Eq. S.6.1 and Eller et al.'s (2018) analytical solution for A_c and A_j (Eq. S3.8 in their Supplementary Info; identical to Eq. S.6.7 for A_j).

$$\frac{\partial A_n}{\partial A_c} = \frac{1}{2c'} \left[1 - \frac{A_c + (1-2c')A_j}{\sqrt{(A_j + A_c)^2 - 4c'A_jA_c}} \right] \quad (\text{S.6.14})$$

$$\frac{\partial A_c}{\partial c_i} = V_{c,max} \frac{\Gamma^* + K_c \left(1 + \frac{\phi_a}{K_o} \right)}{\left[c_i + K_c \left(1 + \frac{\phi_a}{K_o} \right) \right]^2} \quad (\text{S.6.15})$$

$$\frac{\partial A_j}{\partial c_i} = \frac{J}{4} \frac{3\Gamma^*}{(c_i + 2\Gamma^*)^2} \quad (\text{S.6.16})$$

Sperry et al. (2017) included the effects of transpiration leaf cooling as part of the *Gain-Risk* optimization, which we have excluded from THORP. Instead, we assume the leaf temperature may be approximated by the air temperature. This change has negligible effects on the algorithm's optimal Ψ_L . The cooling mechanism was not included in THORP, because its inclusion can lead to $\lambda < 0$ when λ is evaluated simply as $(\partial A_n / \partial \Psi_L) / (\partial E / \partial \Psi_L)$. Negative λ arose when $\partial A_n / \partial \Psi_L > 0$, since $\partial E / \partial \Psi_L$ is always non-positive (Sperry & Love 2015; Sperry et al. 2016). Inclusion of transpirative cooling can result in a peaked $A_n(\Psi_L)$ curve ($\partial^2 A_n / \partial \Psi_L^2 < 0$), due to suppression of $V_{c,max}$ and J_{max} through their temperature-dependence at lower temperatures found at larger E and more-negative Ψ_L . When this peaked $A_n(\Psi_L)$

response occurs, an optimal Ψ_L predicted by the *Gain-Risk* algorithm more-negative than the leaf potential at which A_n is maximum would cause $\partial A_n / \partial \Psi_L > 0$ and $\lambda < 0$. Additionally, we have ignored transpirative cooling to simplify the derivation of dE/dD , dE/da_L , $dE/dC_{R,H,i}$, and $dE/dC_{R,V,i}$ terms in Section S.3 (particularly in the assumptions necessary to state Eq. S.3.41).

It is noteworthy that the modeled λ varies diurnally here as xylem water potentials changes (Wolf et al., 2016), which is consistent with studies that directly interpret λ from steady-state measurements of gas exchange under various conditions taken at subdaily time scales (e.g. Hall & Schulze, 1980; Fites & Teskey, 1987; Thomas et al., 1999; Manzoni et al., 2011) by applying equations derived by Cowan and Farquhar (1977; their Eq. 14-17) or similar equations.

S.7 Maintenance Respiration and Senescence

Whole-tree maintenance respiration, R_m [$\text{mol C} \cdot \text{s}^{-1}$] is the sum of leaf, sapwood, and root maintenance respiration rates

$$R_m = a_L R_d + r_{sW}^m C_{sW} + r_R^m C_R \quad (\text{S.7.1})$$

where r_{sW}^m and r_R^m are the carbon pool-specific maintenance respiration rates for sapwood and roots, respectively [s^{-1}]. Leaf dark respiration, R_d [$\text{mol C} \cdot \text{m}^{-2} \cdot \text{s}^{-1}$], and its temperature-dependence were defined in Section S.6. The temperature-dependences of r_{sW}^m and r_R^m were modeled using Q_{10} -type equations with $Q_{10} = 1.80$ for the sapwood of Scots Pine (Zha et al., 2004), and $Q_{10} = 1.98$ for the roots of Scots Pine (Janssens et al., 1999). Future versions of THORP may include nitrogen partitioning and represent respiration's sensitivity to nitrogen content (Sprugel et al., 1995) to predict changes in allocation in nutrient-limited environments, under anthropogenic atmospheric nitrogen deposition, and in response to elevated atmospheric carbon dioxide concentrations.

Senescence rates are determined simply from organs' mean life spans. The senescence rates of leaves, sapwood, and the two root pools within the i th soil layer, S_L , S_{sW} , $S_{R,H,i}$, and $S_{R,V,i}$, respectively [$\text{mol C} \cdot \text{s}^{-1}$], are given by

$$S_L = \frac{C_L}{\tau_L} \quad (\text{S.7.2})$$

$$S_{sW} = \frac{C_{sW}}{\tau_{sW}} \quad (\text{S.7.3})$$

$$S_{R,H,i} = \frac{C_{R,H,i}}{\tau_R} \quad (\text{S.7.4})$$

$$S_{R,V,i} = \frac{C_{R,V,i}}{\tau_R} \quad (\text{S.7.5})$$

where τ_L , τ_{sW} , and τ_R are the mean life spans of the leaf, sapwood, and root pools, respectively [s]. Mean life spans are currently assumed constant in THORP; however future versions may include variable senescence rates that depend on environmental and physiological factors, most notably embolism (Mackay et al., 2015), to predict responses to stress-induced and seasonal deciduousness and test the role of hydraulic segmentation theory within a tree's allocation response.

S.8 Dynamic Allocation Fractions

THORP predicts the dynamic partitioning of an individual tree's biomass between sapwood, roots, and leaves that optimizes net growth at sub-daily time-scales. THORP optimizes net growth since a tree's growth and survival are determined by competitiveness and ability to uptake resources, which are related to size and thus biomass integrated over time (Franklin, 2007). THORP does not presently describe allocation for reproduction. Growth and senescence are simulated continuously at each time-step, and allocation fractions recalculated each day at noon as the costs and benefits of enhancing the uptake of different resources vary, suggesting that the tree's allometry is best-adapted to midday conditions. We note that while the optimality model by Buckley and Roberts (2006a) did not explicitly optimize tree allometry for midday conditions, they parameterized their model with constant leaf water potentials (i.e. stomatal conductance changed with tree-size to maintain a constant leaf water potential regardless of the hydrostatic gradient or in-series hydraulic resistances throughout the plant) that were based on midday measurements (Yoder et al., 1994), and thus their results implicitly reflect this assumption. The simulated tree is ever-striving towards an optimal allometry that balances water-use and light interception. This optimum may dynamically change as environmental conditions shift and depends on the tree's existing structure and physiology. This optimization results in the most growth occurring in the most limiting organ until overall fitness is limited by all resources equally (Bloom et al., 1985). We assume that the allocation to the k th carbon pool, where k may represent leaves ($k = L$), sapwood ($k = sW$), and roots in each soil layer ($k = R, i$), is enhanced when economic gain for that pool is large and diminished when the economic cost is large. We express this concept mathematically using the ratio of the economic gain and cost as

$$u_k \propto \frac{\text{marginal gain}_k}{\text{marginal cost}_k} \quad (\text{S.8.1})$$

where u_k is the instantaneous allocation fraction to the k th carbon pool, and *gain* is defined here as the total net canopy carbon assimilation rate, which equals the total gross assimilation, $a_L(A_n + R_d)$, minus the whole-tree respiration, R_m (including leaf respiration, $a_L \cdot R_d$, by Eq. S.7.1) (Bloom et al., 1985), while *cost* represents senescence costs (Magnani et al., 2000).

$$\text{marginal gain}_k = \frac{d}{dc_k} [a_L(A_n + R_d) - R_m] \quad (\text{S.8.2})$$

$$\text{marginal cost}_k = \frac{dS_k}{dc_k} = \tau_i \quad (\text{S.8.3})$$

Through Eq. S.8.1-3, marginal gain terms are weighted by the mean life spans of the corresponding carbon pool, τ_i , meaning that carbon is allocated in a manner that considers how long any investment of carbon will last and potentially benefit a tree. Investments with short-lived payoffs (i.e. small τ_i) benefit the tree only briefly and thus reflect poor investments over the duration of a tree's life. So that all allocation fractions sum to unity ($\sum u_k = 1$ for all k), we evaluate each allocation fraction as its marginal *gain-cost* ratio normalized by the sum of all marginal *gain-cost* ratios

$$u_k = \frac{\max\left(0, \frac{\text{marginal gain}_k}{\text{marginal cost}_k}\right)}{\sum_j \max\left(0, \frac{\text{marginal gain}_j}{\text{marginal cost}_j}\right)} \quad (\text{S.8.4})$$

where j is all k carbon pools (leaves, sapwood, and the $2N$ root carbon pools). This approach is analogous to the gradient ascent method (Cauchy, 1847; Curry, 1944) in the mathematical field of nonlinear optimization. We do not allocate carbon to an organ when its economic gain is negative; hence the max operators eliminate negative values in Eq. S.8.4. In this case, no new carbon is allocated to that organ

until benefit becomes positive. Additionally, we do not allow roots of either root pool to be allocated to a soil layer when that soil layer is saturated ($\Psi_{soil,i} \geq 0$) by setting the corresponding root layer's marginal gain-cost ratio terms to zero (marginal gain $_{R,H,i}$ /marginal cost $_{R,H,i} = 0$; marginal gain $_{R,V,i}$ /marginal cost $_{R,H,i} = 0$). This constraint prevents roots from growing at soil depths where gasses could not diffuse and where roots would suffocate. Furthermore, this constraint is internally consistent with THORP's allocation scheme, considering the lifespan for suffocating roots would be very short ($\tau_R \approx 0$; marginal cost $_{R,H,i} \rightarrow \infty$; marginal cost $_{R,V,i} \rightarrow \infty$), and through Eq. S.8.3-4, roots should preferentially grow elsewhere (i.e. where $\Psi_{soil} < 0$). However, we do not explicitly change the value of τ_R for soil layers where $\Psi_{soil,i} \geq 0$, since such a change leads to numerical difficulties in calculating root senescence through Eq. S.7.4-5.

THORP presently estimates the allocation from instantaneous conditions (i.e. all of THORP's submodules, including allocation, are performed in unison for the same conditions and at the same time-scales), and consequently ignores any possible anticipatory plant behaviors. Simulating anticipation would require either integrating conditions over longer time-scales or some stochastic approach based on previous environmental conditions (either approach would be for allocation's response to environment, not other processes like photosynthesis or transpiration). Both methods have their merits, though the former is not appropriate for predicting short-term allocation change strategies, which THORP attempts. Future version of THORP may consider some anticipatory behavior, especially if ever intending to focus THORP as a tool for prediction at small spatial scales. Alternatively, there is evidence that plant allocation is synced to the previous year's environmental conditions (e.g. Richardson et al., 2013), which could form a simple basis for modeling anticipation. However, we presently only attempt to validate THORP's general qualitative trends to various stimuli, again instantaneously, and do not attempt to postulate at which time-scales plants sense their surroundings, perhaps in an integratory way, or any potential role of "memory". Nonetheless, we emphasize that only the estimation of allocation fractions ($u_L, u_{SW}, u_{RH}, u_{RV}$) is strictly instantaneous in THORP; however, the resulting allometry is the time-integral of the product of allocation fraction and growth rate (G) minus the relevant senescence (Eq. S.9.3-5). So while the allocation is instantaneous, the allometry better reflects a longer-term effective mean of the environment. Delays between stimuli and the obvious appearance of response in the allometry will be advanced or delayed depending on G 's strength or weakness, respectively.

THORP does not solve for the global optimum of an objective function, and thus is not an optimality model in the traditional sense. Our approach is similar to Caldararu et al.'s (2020) approach to dynamic nitrogen allocation and is meant to approximate Buckley and Robert's (2006a) dynamic, numerical solution for how additional biomass should be optimally partitioned within the constraints of the carbon available for allotment. We emphasize that Buckley and Roberts (2006a) solved for the optimal *path* rather than the optimal allometry, and we attempt to approximate that path. Like strict optimality models, THORP's allocation to a carbon pool will cease when the size of that pool is optimal (i.e. when the *marginal gain* is zero in our case, where we seek to maximize *gain*). Our approach is conceptually, though not necessarily mathematically, similar to maximizing growth, since we have assumed that growth rates, G , are a positive, monotonic function of NSC storage (Eq. S.9.2). Consequently, THORP seeks to maximize assimilation, which leads to elevated NSC and growth.

The use of the gradient ascent method (Cauchy, 1847; Curry, 1944) and Eq. S.8.4 may be more intuitive when considering a system with only two carbon pools ($j = 2$). For purpose of this explanation, let us consider a plant with only shoots and roots (with only 'horizontal' roots stored in a single soil layer) denoted by their sizes, C_{Shoot} and C_{Root} , respectively. If fitness, F , is a surface defined in C_{Shoot} - C_{Root} space, and if one's location along the F - C_{Shoot} - C_{Root} continuum can only change total distance of ΔC (where $(\Delta C)^2 = (\Delta C_{Shoot})^2 + (\Delta C_{Root})^2$, and $\Delta C = G \cdot \Delta t$ if ignoring senescence), then the best path towards the

optimum (i.e. where $\partial F/\partial C_{Shoot} = \partial F/\partial C_{Root} = 0$) would require that allocation to either pool be weighted by their slope (projected on the relevant axis) of the fitness surface (i.e. $\Delta C_{Shoot} \propto \partial F/\partial C_{Shoot}$, and $\Delta C_{Root} \propto \partial F/\partial C_{Root}$). Hence, we arrive to the general form of Eq. S.8.4, particularly that $\Delta C_{Shoot} = \Delta C \cdot \partial F/\partial C_{Shoot} / (\partial F/\partial C_{Shoot} + \partial F/\partial C_{Root})$, and $\Delta C_{Root} = \Delta C \cdot \partial F/\partial C_{Root} / (\partial F/\partial C_{Shoot} + \partial F/\partial C_{Root})$. These gradient ascent equations are applied to two arbitrary fitness surfaces in Figure S1 in comparison to the true optimal paths. The optimal path depends on the initial coordinates (C_{Shoot} , C_{Root}), which were arbitrarily chosen in these examples, and the gradient ascent method's ability to accurately approximate the true, optimal path depends on the size of the rate of allocation (represented here by ΔC). This pondering of allocation strategy leads us next to ask about how to reasonably define the fitness proxy, F , and whether this allocation strategy is weighted by more than just the slope of the fitness surface.

We recognize that most optimality approaches define fitness as the difference between gain and cost (suggesting $F = \text{gain} - \text{cost}$; Bloom et al., 1985), and in this case, the optimal allometry satisfies *marginal gain* – *marginal cost* = 0. In comparison, our Eq. S.8.1-8.4 may appear slightly unorthodox. However, a common definition for F is gross assimilation minus respiration (e.g. Bloom et al., 1985; Buckley & Roberts, 2006a; Franklin, 2007; McMurtrie et al., 2008; Mäkelä et al., 2008), where traditionally assimilation represents *gain* and respiration represents *cost*, and senescence costs are not typically considered. We have defined *gain* here as gross assimilation minus respiration (Eq. S.8.2), which agrees well with the traditional definition for fitness, F . The difference then is that and how we include senescence costs within the allocation algorithm. Hereon, we use cost as a term to refer solely to senescence costs, since respiration costs are already incorporated within the *gain* term. Prior developmental stages of the model assumed that $u_k \propto (\text{marginal gain}_k - \text{marginal cost}_k)$ and lead to unrealistic results over a large range of physiological and environmental conditions, particularly zero root allocation and excessive stem allocation. These responses result from roots' large senescence costs (short life span) versus woods' small costs (long life span). The difference between gain and cost has not always been the sole assumed fitness proxy, and notable exceptions include Magnani et al. (2000; their Eq. 13) who used the ratio of *marginal gain* and *marginal cost*, where their *cost* reflected senescence. Since the difference between gain and costs (i.e. $u_k \propto \partial(a_L \cdot (A_n + R_d) - R_m - S_k)/\partial C_k$) produced unrealistic results, we consider the intuitive alternative supported by Magnani et al. (2000) that $u_k \propto \partial(a_L \cdot (A_n + R_d) - R_m)/\partial C_k / \partial S_k/\partial C_k$, which simplifies to $u_k \propto \tau_k \cdot \partial \text{gain}/\partial C_k$, where τ_k is the pool's mean life span (Eq. 7.2-4), and we use *gain* to refer to $a_L \cdot (A_n + R_d) - R_m$. This choice of allocation strategy suggests plastic allocation by which a one-time allocation of $u_k \cdot \Delta C$ to pool k is expected to increase the gross profit of the system by $u_k \cdot \Delta C \cdot \partial \text{gain}/\partial C_k$ for an amount of time equal to τ_k . Thus, the time-scale of allocation and that of reaping the benefits from investment are not coupled. The previous alternative, $u_k \propto (\text{marginal gain}_k - \text{marginal cost}_k)$, suggests that a portion of all gain must be continually spent to replace senescing biomass, which implies a temporal rigidity in plant allometry and a lack of opportunism. Considering that root distributions are seasonally dynamic and active regions may switch between deep and shallow distributions within a couple months without replacing older root zones (Chen et al., 2002, 2004; Schenk, 2005), we prefer $u_k \propto \text{marginal gain}_k / \text{marginal cost}_k$ over $u_k \propto (\text{marginal gain}_k - \text{marginal cost}_k)$. The same choice could have been made based on the inherent plasticity of seasonal leaf phenology (at least for deciduous species). Our choice that $u_k \propto \text{marginal gain}_k / \text{marginal cost}_k$ suggests that $F = \text{gain}$ (recall that this gain is total net assimilation) and that life spans (or senescence rates) do not affect the true optimal allometry (i.e. where $\partial F/\partial C_k = 0$) but instead only affects the allometric path (i.e. how it approaches the true optimum). Revisiting our hypothetical two pool system, this choice means that the weighting includes not just the slope of the F - C_{Shoot} - C_{Root} surface, but also the life span, such that $\Delta C_{Shoot} = \Delta C \cdot \tau_{Shoot} \cdot \partial F/\partial C_{Shoot} / (\tau_{Shoot} \cdot \partial F/\partial C_{Shoot} + \tau_{Root} \cdot \partial F/\partial C_{Root})$ and $\Delta C_{Root} = \Delta C \cdot \tau_{Root} \cdot \partial F/\partial C_{Root} / (\tau_{Shoot} \cdot \partial F/\partial C_{Shoot} + \tau_{Root} \cdot \partial F/\partial C_{Root})$.

Figure S2 compares a numerical solution for purely maximizing whole-tree net assimilation, $a_L \cdot A_n$, and THORP's allocation algorithm based on the gradient ascent method for various combinations of environmental conditions. The numerical solution was found by iteratively running Sperry et al.'s (2017) *Gain-Risk* algorithm for all combinations of potential allocation fractions (u_{sW} , u_L , u_{RH} , u_{RV}) and choosing the combination of potential allocation fractions with the highest resulting value for $a_L \cdot A_n$. THORP's allocation was performed by effectively removing cost terms (both respiratory and senescent; by setting r_{sW}^m and to r_R^m zero and all life-spans equal; $\tau_k = 1$ for all k) for comparison between the two allocation approaches. THORP's allocation reasonably matches the numerically optimal solution qualitatively. Quantitatively, however, THORP tends to over-predict SMF and under-predict RMF and LMF under some conditions (generally, drier, cooler, sunnier conditions). Though predicted mass fractions may differ between the true, numerical optimization and THORP's approximation, we are satisfied that THORP behaves in the correct direction in response to each stimuli. This comparison is not meant to demonstrate whether either method predicts physiologically realistic mass fractions or whether THORP predicts realistic trends in allocation under different environments in comparison to observed or generally agreed trends in allocation, but rather to show that THORP's analytical approximation behaves near-optimally. Predicting physiologically realistic values and trends in mass fractions requires proper inclusion of cost terms into the objective function and is explored in the main text (Figures 2-6).

By applying the product and chain rules, marginal gain terms are solved from Eq. S.8.2 by the following general equation that considers the increase in net carbon assimilation associated with increasing light-capture and water-use.

$$\text{marginal gain}_k = (A_n + R_d) \frac{da_L}{dC_k} + a_L \wp \frac{dI}{dC_k} + a_L \lambda \frac{dE}{dC_k} - \frac{dR_m}{dC_k} \quad (\text{S.8.5})$$

We have assumed that trees measure their fitness in solely terms of carbon-, water-, and light-use. The first term on the right-hand side of Eq. S.8.5 represents the productivity of leaves, since it is nonzero only when $k = L$, for which case it simplifies to $(A_n + R_d) \cdot X_L$, where X_L is the specific leaf area (see Section S.1). When leaves are productive, leaf growth is enhanced until excess leaf area begins to limit optimal light interception and hydraulics, which are represented by the second and third terms in Eq. S.8.5 becoming increasingly negative. The second term is the contribution to marginal gain from increased light capture, where $\wp = \partial A_n / \partial I$ (see Section S.6; defined in Eq. S.6.5-11), and the third term is the contribution from improving water-use and further opening stomata, where $\lambda = \partial A_n / \partial E$ (see Section S.6; defined in Eq. S.6.12). Investment in leaves and new wood (through the resulting increase in H and W) improves light interception, while investment in roots and sapwood improve water-use efficiency. For a given canopy width, W , there is a leaf area, a_L , that maximizes I . This behavior is due to that I is the light intercepted by the average leaf instead of the total canopy light interception. Larger leaf areas always mean larger total canopy light interception; however, the interception of the average-leaf begins to decline after an optimum has been passed. Both the second and third terms in S.8.5 depend on leaf area, a_L , and their contributions diminish as leaf area declines. In the extreme case when there are no leaves ($a_L = 0$), all new growth is allocated towards leaves, while no further growth is allocated to sapwood and roots. When the tree is light-limited, \wp is large, and allocation is shifted to leaves and aboveground woody biomass (stems), since those pools can increase light interception (i.e. $dI/dC_k > 0$ for $k = L$ and $k = sW$). As leaves and stems grow, light capture improves, \wp declines, and allocation approaches a new pseudo-equilibrium. Similarly, when the tree is water-stressed, λ is large, and allocation is shifted towards stems and roots to improve hydraulic efficiency of the soil-root-xylem pathway (since generally $dE/dC_k > 0$ for $k = sW$ and $k = R$). As stems and roots grow, water-use acclimates to the new hydraulic conditions, λ declines, and allocation approaches another pseudo-equilibrium.

For the leaf carbon pool ($k = L$), Eq. S.8.5 simplifies to

$$\text{marginal gain}_L = \chi_L \left[A_n + a_L \left(\lambda \frac{dE}{da_L} + \wp \frac{dI}{\partial a_L} \right) \right] \quad (\text{S.8.6})$$

Where $\partial E/\partial a_L$ and $\partial I/\partial a_L$ were defined earlier in Eq. S.3.57 and Eq. S.5.3, respectively.

For the sapwood carbon pool ($k = sW$), Eq. S.8.5 simplifies to

$$\text{marginal gain}_{sW} = a_L \left[\lambda \frac{dE}{dD} + \wp \left(\frac{dI}{\partial H} \frac{\partial H}{\partial D} + \frac{dI}{\partial W} \frac{\partial W}{\partial D} \right) \right] \frac{dD}{dC_W} - r_{sW}^m \quad (\text{S.8.7})$$

where dE/dD was defined in Eq. S.3.56, $\partial I/\partial H$ was defined in Eq. S.5.4, $\partial H/\partial D$ was defined in Eq. S.1.5, $\partial I/\partial W$ was defined in Eq. S.5.5, $\partial W/\partial D$ was defined in Eq. S.1.6, and dD/dC_W was defined in Eq. S.1.7. Note that $\partial E/\partial D$ as defined by Eq. S.3.25 includes the terms associated with the change in E expected for a change in H .

For the i th root carbon pools ($k = R, i$ and), Eq. S.8.5 simplifies to

$$\text{marginal gain}_{R,H,i} = a_L \lambda \frac{dE}{dC_{R,H,i}} - r_R^m \quad (\text{S.8.8})$$

$$\text{marginal gain}_{R,V,i} = a_L \lambda \frac{dE}{dC_{R,V,i}} - r_R^m \quad (\text{S.8.9})$$

where $\partial E/\partial C_{R,i}$ terms were defined in Eq. S.3.59.

Marginal cost terms are evaluated from the definitions of and senescence (see Section S.7).

$$\text{marginal cost}_L = \frac{1}{\tau_L} \quad (\text{S.8.10})$$

$$\text{marginal cost}_{sW} = \frac{1}{\tau_{sW}} \quad (\text{S.8.11})$$

$$\text{marginal cost}_{R,H,i} = \text{marginal cost}_{R,V,i} = \frac{1}{\tau_R} \quad (\text{S.8.12})$$

Note that THORP currently applies constant mean life spans; however, if the sensitivity of senescence rates to environmental and physiological factors was represented in THORP, then allocation would be more responsive to those conditions. For example, if modeled leaf senescence rates enhanced under embolism (Mackay et al., 2015), then leaves' mean life spans would decrease under water-stress, marginal costs of the leaf carbon pool would increase, allocation to the leaf carbon pool would quickly decline, and allocation would be further shifted towards stems and roots, or at least more so than predicted solely by the increase in λ as discussed earlier. Future versions of THORP will include environmental cued senescence.

S.9 Carbon Pool Dynamics

Growth and photosynthesis are uncoupled in THORP (Merganičová et al., 2019). Instead, growth relies on a nonstructural carbohydrate (NSC) storage pool, which allows the model to capture recovery processes after environmental disturbances (Barigah et al., 2013; Hartmann, 2015). We defined NSC as starch NSC and not as soluble sugars required for osmoregulation (Martínez-Vilalta et al. 2016). The NSC pool fills through the gross canopy carbon assimilation rate, $a_L \cdot (A_n + R_d)$ [$\text{mol C} \cdot \text{s}^{-1}$] (see Section S.6), and empties through total maintenance respiration, R_m [$\text{mol C} \cdot \text{s}^{-1}$] (see Section S.7). Carbon is

loaded from the NSC pool, C_S [mol C], into phloem for growth and construction-respiration at rate $G/(1-f_c)$ [mol C·s⁻¹] (where f_c is the fraction of carbon spent on construction-respiration [-]), from which a portion, G [mol C·s⁻¹], is partitioned between total above- and below-ground allocation.

$$\frac{\partial C_S}{\partial t} = a_L(A_n + R_d) - R_m - \frac{G}{1-f_c} \quad (\text{S.9.1})$$

Growth rates depend on the size of the storage pool and have been modeled previously as a Michaelis-Menten function of the NSC pool size (De Schepper & Steppe, 2010; Trugman et al., 2018, Jones et al., 2019). To simplify parameterization, we assume that the behavior is restricted to the linear-portion of the Michaelis-Menten curve as is assumed in some transport-resistance models of plant growth (e.g. Dewar, 1993), and we modify the result by Schiestl-Aalto et al.'s (2015) unitless modifier, here denoted as g_T , that describes growth's temperature-dependence for Scots Pine (their Eq. 10),

$$G = g_T(T_a) \zeta C_S (1 - f_c) \quad (\text{S.9.2a})$$

$$g_T(T_a) = \begin{cases} 0, & T_a < 0^\circ\text{C} \\ \frac{1}{1 + \exp[-(0.185^\circ\text{C}^{-1})(T_a - 18.4^\circ\text{C})]}, & T_a \geq 0^\circ\text{C} \end{cases} \quad (\text{S.9.2b})$$

where ζ is a proportionality constant between phloem loading, $G/(1-f_c)$, and NSC pool size [s⁻¹]. We recognize that this is a crude representation of growth dynamics which we hope to improve in future versions; we emphasize that the present focus of THORP is to predict biomass partitioning for a given tree-size rather than accurately predicting how quickly growth occurs, since allocation better reflects trends in size rather than age (e.g. Brouwer, 1962; Mencuccini et al., 2005).

From the total growth rate, G , carbon is allocated to leaf, sapwood, and soil layer-specific root carbon pools (defined in Section S.1) according to their allocation fractions, u_L , u_{sW} , $u_{R,H}$, and $u_{R,V}$ (see Section S.8), while biomass is lost from each structural pool according the senescence rates, S_L , S_{sW} , $S_{R,H,i}$, and $S_{R,V,i}$ (see Section S.7).

$$\frac{\partial C_L}{\partial t} = u_L G - S_L \quad (\text{S.9.3})$$

$$\frac{\partial C_{sW}}{\partial t} = u_{sW} G - S_{sW} \quad (\text{S.9.4})$$

$$\frac{\partial C_{R,H,i}}{\partial t} = u_{R,H,i} G - S_{R,H,i} \quad (\text{S.9.5})$$

$$\frac{\partial C_{R,V,i}}{\partial t} = u_{R,V,i} G - S_{R,V,i} \quad (\text{S.9.6})$$

Senesced sapwood carbon is added to the heartwood pool in THORP.

$$\frac{\partial C_{hW}}{\partial t} = S_{sW} \quad (\text{S.9.7})$$

As carbon pools are updated at each time-step, the basal diameter, D , increases according to

$$\frac{\partial D}{\partial t} = u_{sW} G \frac{\partial D}{\partial C_W} \quad (\text{S.9.8})$$

where $\partial D/\partial C_W$ was defined in Eq. S.1.7. New H and W at the end of the time-step are calculated from the new D through the power-law scaling equations (Eq. S.1.2-3). The new D_t is computed by $C_{hW} = \rho_{cS} \cdot \zeta \cdot H \cdot D_t^2$ from the new H , D , and C_{hW} values. Leaf area is updated as $a_L = X_L \cdot C_L$, and stem and root maximum hydraulic conductances are computed according to Sections S.3 and S.4, respectively.

S.10 SIMULATION DESCRIPTIONS

This section describes in full detail the ten simulations summarized in Table 2 in the main text. Results are presented in the main text (Figures 2-6), except for those experiments with a pruning, which are in Figure S11.

S.10.1 Control Experiment

We simulate the growth of a Scots Pine (*Pinus sylvestris*) tree over a 100-year period under relatively favorable conditions to qualitatively validate THORP's predictions of allometry and its changes that result from age or size. We test whether THORP captures age- or size-dependent trends in biomass partitioning with realistic biomass fractions (leaf mass fraction, LMF; aboveground woody (stem) mass fraction, SMF; root mass fraction, RMF) as well as other observed partitioning behaviors such as the relationships between leaf area and sapwood area (i.e. the Pipe Model; Shinozaki et al., 1964) and between root and shoot masses (Davidson, 1969). We refer to this simulation as the “control” experiment to which we will compare later subsequent simulations to show THORP's sensitivity to environmental conditions and disturbances. In accordance with Poorter and Nagel (2000) and Poorter et al. (2012, 2015), we often present our results as LMF, SMF, and RMF plotted against total dry mass to best elucidate the effects of size and the differences between treatments. THORP simulates the size of carbon pools and not explicitly biomass; when biomass fractions are reported, they were calculated assuming the dry biomass is 50% carbon by weight, except roots which were assumed to be 55% carbon by weight (Janssens et al., 1999).

We parameterized the model for Scots Pine with values either reported or estimated from past literature. These parameters, their symbols, values, and source are summarized in Table 3 in the main text. Several parameters represent Loblolly Pine (*Pinus taeda*) instead of Scots Pine; however, the two species are of the same genus, and the overall parameterization is meant to represent an evergreen conifer. Belowground hydraulic resistances represent multiple mechanisms including root embolism (Domec et al., 2006), rhizosphere resistance (Newman, 1969; Sperry et al., 1998), root shrinkage and soil detachment (Herkelrath et al., 1977), and switching between apoplastic and symplastic pathways (Fiscus, 1975; Steudle & Peterson, 1998). However, measurements of belowground resistances of tree roots are typically estimated from measurements of potential gradients between root collar and bulk soil which do not capture the various mechanisms separately (e.g. Martínez-Vilalta et al., 2007; Poyatos et al., 2018; Lintunen et al., 2019). We parameterized belowground resistances in THORP using measurements reported by Poyatos et al. (2018; see Table 3 in main text) that represent the properties of both Scots Pine

roots and the soil at their study site in the Poblet nature reserve (Prades Mountains, Northeastern Iberian Peninsula, 41° 19' 58.05" N, 1° 0' 52.26" E). The climate there is Mediterranean, with a mean annual rainfall of 664 mm (spring and autumn being the rainiest seasons and with a marked summer dry period) and moderately warm temperatures (11.3 °C on average; Poyatos et al. 2013). Consequently, soil parameters were selected to represent the Poblet nature reserve's soil and geology. Similarly, the lower boundary condition (at the bottom of the simulated soil column, which is here 30 m deep) for solving Richards equation is in free drainage (see Section S.2), which was chosen because the water table at the Poblet nature reserve has been estimated as deep as 70-100 m in agreement with nearby observations (Fan et al., 2013). Note that the 30 m deep 'soil column' refers to the domain over which Richards equation is solved and does not strictly represent solely soil; it represents true soil at shallow depths, weathered bedrock at deeper depth, and their transition in between. The model was simulated for a total of 100-years at 6-hour time-steps with NOAA re-analysis data (NCEP/NCAR Reanalysis 1; Kalnay et al., 1996) as environmental forcing, namely air and soil temperatures, relative air humidity of the air, precipitation, windspeeds, and incoming solar insolation. We chose the NOAA re-analysis data set, because it immediately provided all of THORP's forcing inputs, except relative humidity which was calculated from specific humidity. Re-analysis data was taken from 1948-1958 and repeated 10-times and from the land cell with the smallest Euclidean distance from the Poblet nature reserve. We chose the 1948-1958 period instead of the entire available NOAA re-analysis data set (i.e. 1948 to present) to avoid long-term warming and drying trends. In other experiments, simulations were run for a minimum for 100 years and until a total tree dry biomass similar to the end of the control simulation was achieved. When run longer than 100 years, additional repetitions of the 1948-1958 NOAA re-analysis data were simulated.

The control experiment was initialized with variables chosen to represent Scots Pine an environment similar to the modern Poblet nature reserve and its climate from the mid-twentieth century. The initial allometry was calculated for a tree with a $1.5 \cdot 10^{-2}$ m basal diameter, from which height and canopy width can be calculated by Eq. S.1.2-3 (~4.4 m and ~0.6 m, respectively). Wood biomass was calculated from Eq. S.1.1 in the SI. Sapwood and heartwood masses were calculated assuming the sapwood fraction of the total wood is 94% for Scots Pine of similar size (Mencuccini & Grace, 1996). Leaf area was calculated by an initial LAI of 0.4 based on Poyatos et al. (2013), from which leaf mass can be solved through the specific leaf area and leaf carbon content by weight (50%). Total root mass was calculated assuming an initial RMF of 30% based on Poorter et al. (2011) for gymnosperms at the appropriate size. Root mass was converted to total root carbon, C_R , by the root carbon content by weight (55%) and was distributed between soil layers according to the asymptotic function $Y = 1 - \beta^d$ (Gale & Grigal, 1987, Jackson et al., 1996; Venturas et al., 2018), where Y is the cumulative root fraction from the ground surface to depth, d . This initial rooting distribution is not unreasonable for our site considering its

trees are rain-fed due to the depth of its water table. The extinction coefficient, β , was chosen so that 99% of root biomass was above a 3 m depth, chosen for being approximately the mean rooting depth for Pines (Fan et al., 2017). Soil water potentials were initialized assuming hydrostatic equilibrium with a 74 m deep water table, except in simulations when a groundwater table was introduced, in which the initial soil water potentials were assumed to be in hydrostatic equilibrium with the defined groundwater table depth. Then within each soil layer, total root carbon, $C_{R,i}$, was divided into intralayer- and interlayer-conductive portions, $C_{R,H,i}$ and $C_{R,V,i}$, respectively. The initial proportioning of $C_{R,H,i}$ and $C_{R,V,i}$ was chosen so that a layer's total hydraulic resistance, $R_{R,i}$ (Eq. S.3.2), was equal portions of 'horizontal' and 'vertical' resistances, $R_{R,H,i}$ and $\Sigma R_{R,V,j}$ for $1 \leq j \leq i$, respectively, so that root-water uptake within a single soil-layer was equally limited by each form of resistance. This initialization requires solving the proportioning in a top-down approach, beginning with the topmost soil layer and then successively solving each next, deeper soil layer, since the total vertical resistance, $\Sigma R_{R,V,j}$ for $1 \leq j \leq i$, depends on the interlayer-conductive root carbon of all shallower layers. Furthermore, this initial proportioning depends on the soil and root collar water potentials through $f_{R,i}$ (Eq. S.3.3), which we assumed both equaled the initial soil water potential profile for the sake of this initialization. The NSC pool was initialized assuming NSC concentrations of 20% in leaves, 4% in wood, and that 20% of the total NSC is belowground (Hoch & Körner, 2003). Biomass fractions (LMF, SMF, RMF) are reported after a ~2.6 years spin up period for allometry and soil hydrology to equilibrate.

S.10.2 Hydrometeorological Drought Experiments

Simulations were performed to test if THORP captures trees' sensitivity to water stress and soil hydrology. The study site is rain-fed so we introduced water stress by reducing precipitation rates. In the first two of these simulations, conditions were the same as control experiment except precipitation rates were reduced to 50% and 75% of their control values. Since simulations were performed at different growth rates due to differences in carbon assimilation rates, we compare allocation from these simulations to the control experiment in terms of total biomass rather than solely by time. We test THORP's predictive power under water stress by comparing biomass partitioning (LMF, SMF, RMF), rooting depth, and Huber values (the ratio of sapwood and leaf areas) to those of the control experiment. Rooting depth is generally reported as the depth above which 95% of root biomass is present ($Z_{95\%}$ in Figure 2a,c, 5a,b,c, S.6a,e, S.7a,e, S.8a,e, S.9a,e), and we sometimes consider the depth above which 99.5% of root biomass is present ($Z_{99.5\%}$ in Figure 5c).

A third water stress experiment was performed with a shallow, 2 m deep water table to investigate the drought response of trees that can access stable sources of water and to demonstrate THORP's sensitivity in predicting allocation. This simulation was the same as control experiment except precipitation rates were reduced to 50%, and the free drainage lower boundary condition for solving Richards equation was replaced by a constant pressure (Dirichlet) boundary condition (see Eq. S.2.26). Specifically, Richards equation was solved only for the nodes above the defined groundwater table, and the closest internode that was deeper than defined groundwater table became the new bottom boundary for this domain. All nodes below the defined groundwater table were assumed in hydrostatic equilibrium with groundwater table; however, this assumption does not alter THORP's predictions of allometry, since we constrained root growth to layers where $\Psi_{soil,i} < 0$ (discussed in Section S.8). We assumed that the internode that defined the bottom of the domain over which Richards equation was solved was in constant hydrostatic equilibrium with the water table, so that the soil water potential at the bottom of soil column (i.e. the Dirichlet condition) was positive but small. Similarly, soil water potentials were initialized assuming hydrostatic equilibrium with the water table. We recognize that this lower boundary condition does not necessitate that the water table's true location (i.e. where the soil water potential is zero) stay at the defined depth for the groundwater table, and in fact the water table depth will slightly vary seasonally and deepen over time as the tree's transpirational needs increase with size. We tracked the true depth of the water table throughout this simulation to compare to the simulated rooting depth and report its mean values. After running THORP with a 2 m deep water table, additional experiments were simulated with deeper groundwater tables to investigate the role of soil moisture profiles on rooting depth and root distribution with depth. Between experiments, the groundwater table was lowered in 2 m increments down to 20 m, then down to 40 m in 4 m increments, and lastly down to 80 m in 8 m increments.

S.10.3 Aboveground Competition and Elevated Atmospheric CO₂

We performed a simulation with an added overstory canopy ($H_n > H$ in Section S.5) that shades the simulated tree to validate THORP's predictions of allocation responses to competition for light. This simulation is the same as the control experiment, except a 30 m tall overstory with a LAI of 3 was introduced ($K_n = 3.2 \cdot 10^{-2} \text{ m}^{-1}$ in S.5 of SI instead of value in Table 3 in main text) after the ~2.6 spin-up period. We recognize that this simulation represents an end-member case where target tree is more light-stressed than that of the control case, but its belowground resource acquisition is not affected, since we have not altered soil moisture conditions. In reality, additional trees from the overstory would also transpire, dry soils, influence the depths from which our target tree can conduct water, and thus directly influence belowground allocation for the target tree as well.

We performed an experiment with elevated atmospheric CO₂ concentrations that was identical to the control except CO₂ concentrations were elevated to 600 ppm to compare to past Free-Air CO₂ Enrichment (FACE) experiments and other meta-analyses. The current version of THORP does not describe nutrient acquisition and partitioning, so this simulation represents the case of elevated CO₂ without the possibility of nutrient limitation.

S.10.4 Recovery from Pruning

We performed simulations designed after the classic Brouwer (1962) pruning experiments to test THORP's ability to capture recovery after disturbance. In the pruning experiments, Brouwer (1962) measured changes in shoot and root biomasses of bean plants. After a period of time, he pruned half of either the leaves or the roots, and after a week or so, the initial proportion of root-to-shoot masses had recovered. Similar experiments have since been repeated and concluded to characterize a wide range of species (Alexander & Maggs 1971; Farrar & Gunn, 1998; Poorter & Nagel, 2000). After a given time into the control experiment, we disturbed our simulated tree by removing half of either its root or shoot mass and then continued the remainder of the 100-year simulation. Our disturbance does not strictly represent true pruning like in the Brouwer (1962) experiment, but may represent other various processes that can alter biomass distributions, such as defoliation due to herbivory or by fire or dieback due to severe drought. We performed four total recovery experiments to show the effects of tree size on recovery: two in which pruning occurred after the initial ~2.6 year spin up period and two in which pruning occurred after the first 30 years of simulation.

We 'pruned' roots by simply reducing the root carbon pool of each soil layer by 50% (both interlayer and intralayer pools halved), and we 'pruned' shoots by reducing the leaf and aboveground sap- and heart-wood carbon pools by 50%. Additionally, 'pruning' shoots required extra changes so not to invalidate THORP's assumptions about the fractal hydraulic architecture of the tree (see Section S.4) and light interception (see S.5). We made parameter changes at the time of pruning that represent a trunk that has been cut in half vertically (i.e. the main trunk is semicircular in horizontal cross-section and no longer circular). These changes require that for a given basal diameter, the stem xylem conductance is halved (b_2 which controls stem conductance was halved). We assume that the halved-tree grows in a way that maintains its basal semicircularity, and so half as much woody biomass is required to grow radially (ζ which governs wood volume was halved). Lastly, we assume that the LAI of the half-tree, which influences light interception, has not changed despite there being only half the total leaf area. We

maintain LAI at the time of pruning by reducing the canopy area by half (b_1 which controls canopy width was multiplied by $\sqrt{0.5}$).

Pruning experiments resulted in shifted allocation towards the pruned organs to recover the shoot-root ratio of the control experiment (Figure S11a). After pruning, shoot-root ratios are recovered within fewer than 10 years in all simulations regardless of initial size or whether above- or belowground carbon pools were halved. Though shoot-root ratios recovered in all simulations, total biomass and productivity only recovered in experiments in which roots were pruned (Figure S11b), largely because roots represented a relatively small fraction of the total biomass. In experiments with pruned shoots, total biomass never returned to that of the control experiment, and the change in total biomass per unit time (slopes of lines in Figure S11b) were halved relative to the control experiment. This reduction in productivity is the result of halving the total leaf area and thus total canopy carbon assimilation, since aboveground hydraulics and light interception were maintained through the change in parameters (b_1 , b_2 , and ξ) at the time of pruning.

References

- Alexander DM, Maggs DH (1971) Growth responses of sweet orange seedlings to shoot and root pruning. *Annals of Botany* 35, 109–115.
- Barigah TS, Bonhomme M, Lopez D, Traore A, Douris M, Venisse J-S, Cochard H, Badel E. (2013). Modulation of bud survival in *Populus nigra* sprouts in response to water stress-induced embolism. *Tree Physiol* 33:261–274.
- Beven, K. J., & Kirkby, M. J. (1979). A physically based, variable contributing area model of basin hydrology. *Hydrological Sciences Bulletin*, 24(1), 43–69.
- Bloom, A. J., Chapin III, F. S., & Mooney, H. A. (1985). Resource limitation in plants-an economic analogy. *Annual review of Ecology and Systematics*, 16(1), 363–392.
- Brouwer, R. (1962). Nutritive influences on the distribution of dry matter in the plant. *Netherlands Journal of Agricultural Sciences* 10, 361–376.
- Buckley, T. N., Miller, J. M., & Farquhar, G. D. (2002). The mathematics of linked optimisation for water and nitrogen use in a canopy. *Silva Fennica*, 36(3), 639–669.
- Buckley, T. N., & Roberts, D. W. (2006a). DESPOT, a process-based tree growth model that allocates carbon to maximize carbon gain. *Tree Physiology*, 26(2), 129–144.
- Buckley, T. N., & Roberts, D. W. (2006b). How should leaf area, sapwood area and stomatal conductance vary with tree height to maximize growth?. *Tree Physiology*, 26(2), 145–157.
- Buckley, T. N., Sack, L., & Farquhar, G. D. (2017). Optimal plant water economy. *Plant, cell & environment*, 40(6), 881–896.
- Cabon, A., Fernández-de-Uña, L., Gea-Izquierdo, G., Meinzer, F. C., Woodruff, D. R., Martínez-Vilalta, J., & De Cáceres, M. (2020a). Water potential control of turgor-driven tracheid enlargement in Scots pine at its xeric distribution edge. *New Phytologist*, 225(1), 209–221.
- Cabon, A., Peters, R. L., Fonti, P., Martínez-Vilalta, J., & De Cáceres, M. (2020b). Temperature and water potential co-limit stem cambial activity along a steep elevational gradient. *New Phytologist*, 226(5), 1325–1340.
- Caldararu, S., Thum, T., Yu, L., & Zaehle, S. (2020). Whole-plant optimality predicts changes in leaf nitrogen under variable CO₂ and nutrient availability. *New Phytologist*, 225(6), 2331–2346.
- Campbell G.S. & Norman J.N. (1998). *An Introduction to Environmental Biophysics* 2nd edn. Springer, New York.
- Cauchy, A. L. (1847). Compte rendu des séances de l'académie des sciences. *Comptes Rendus Hebd. Seances Acad. Sci*, 21(25), 536–538.
- Chen, X., Eamus, D., & Hutley, L. B. (2002). Seasonal patterns of soil carbon dioxide efflux from a wet-dry tropical savanna of northern Australia. *Australian Journal of Botany*, 50(1), 43–52.
- Chen, X., Eamus, D., & Hutley, L. B. (2004). Seasonal patterns of fine-root productivity and turnover in a tropical savanna of northern Australia. *Journal of Tropical Ecology*, 221–224.

- Coussement, J. R., De Swaef, T., Lootens, P., Roldán-Ruiz, I., & Steppe, K. (2018). Introducing turgor-driven growth dynamics into functional–structural plant models. *Annals of botany*, 121(5), 849–861.
- Cowan IR, Farquhar GD. (1977). Stomatal function in relation to leaf metabolism and environment. *Symp Soc Exp Biol* 31:471–505.
- Curry, H. B. (1944). The method of steepest descent for non-linear minimization problems. *Quarterly of Applied Mathematics*, 2(3), 258–261.
- Davidson, R. L. (1969). Effect of root/leaf temperature differentials on root/shoot ratios in some pasture grasses and clover. *Annals of Botany*, 33(3), 561–569.
- de Pury, D.G.G. and Farquhar, G.D. (1997). Simple scaling of photosynthesis from leaves to canopies without the errors of big-leaf models. *Plant, Cell & Environment*, 20: 537–557.
- De Schepper, V. & Steppe, K. (2010). Development and verification of a water and sugar transport model using measured stem diameter variations. *J. Exp. Bot.*, 61, 2083–2099.
- Dewar, R. C. (1993). A root-shoot partitioning model based on carbon-nitrogen-water interactions and Münch phloem flow. *Functional Ecology*, 356–368.
- Domec, J.C., Scholz, F.G., Bucci, S.J., Meinzer, F.C., Goldstein, G. & Villalobos-Vega, R. (2006) Diurnal and seasonal variation in root xylem embolism in neotropical savanna woody species: impact on stomatal control of plant water status. *Plant, Cell and Environment*, 29, 26–35.
- Eller, C. B., Rowland, L., Oliveira, R. S., Bittencourt, P. R., Barros, F. V., da Costa, A. C., ... & Cox, P. (2018). Modelling tropical forest responses to drought and El Niño with a stomatal optimization model based on xylem hydraulics. *Philosophical Transactions of the Royal Society B: Biological Sciences*, 373(1760), 20170315.
- Evans, J. R. (1989). Photosynthesis and nitrogen relationships in leaves of C₃ plants. *Oecologia*, 78(1), 9–19.
- Fan, Y., Li, H., & Miguez-Macho, G. (2013). Global patterns of groundwater table depth. *Science*, 339(6122), 940–943.
- Fan, Y., Miguez-Macho, G., Jobbágy, E. G., Jackson, R. B., & Otero-Casal, C. (2017). Hydrologic regulation of plant rooting depth. *Proceedings of the National Academy of Sciences*, 114(40), 10572–10577.
- Farrar JF, Gunn S (1998). Allocation: allometry, acclimation — and alchemy? In ‘Inherent variation in plant growth. Physiological mechanisms and ecological consequences’. (Eds H Lambers, H Poorter and MMI Van Vuuren) pp. 183–198. (Backhuys Publishers: Leiden, The Netherlands).
- Farquhar, G. D., von Caemmerer, S. V., & Berry, J. A. (1980). A biochemical model of photosynthetic CO₂ assimilation in leaves of C₃ species. *Planta*, 149(1), 78–90.
- Fatichi, S., Leuzinger, S., & Körner, C. (2014). Moving beyond photosynthesis: from carbon source to sink-driven vegetation modeling. *New Phytologist*, 201(4), 1086–1095.
- Fatichi, S., Pappas, C., Zscheischler, J., & Leuzinger, S. (2019). Modelling carbon sources and sinks in terrestrial vegetation. *New Phytologist*, 221(2), 652–668.

- Field, C. H., & Mooney, H. A. (1986). Photosynthesis--nitrogen relationship in wild plants. In *On the Economy of Plant Form and Function: Proceedings of the Sixth Maria Moors Cabot Symposium, Evolutionary Constraints on Primary Productivity, Adaptive Patterns of Energy Capture in Plants, Harvard Forest, August 1983*. Cambridge [Cambridgeshire]: Cambridge University Press, c1986.
- Fiscus, E. L. (1975). The interaction between osmotic-and pressure-induced water flow in plant roots. *Plant Physiology*, 55(5), 917-922.
- Fites, J. A., & Teskey, R. O. (1988). CO₂ and water vapor exchange of *Pinus taeda* in relation to stomatal behavior: test of an optimization hypothesis. *Canadian Journal of Forest Research*, 18(2), 150-157.
- Franklin, O. (2007). Optimal nitrogen allocation controls tree responses to elevated CO₂. *New Phytologist*, 174(4), 811-822.
- Fritts, H. C., Shashkin, A., Hemming, D. L., Leavitt, S. W., Wright, W. E., & Downes, G. M. (2000). User Manual for TREERING 2000.
- Gale, M. R., & Grigal, D. F. (1987). Vertical root distributions of northern tree species in relation to successional status. *Canadian Journal of Forest Research*, 17(8), 829-834.
- Givnish, T. J. (1986). Optimal stomatal conductance, allocation of energy between leaves and roots, and the marginal cost of transpiration. In *On the economy of plant form and function: proceedings of the Sixth Maria Moors Cabot Symposium, Evolutionary Constraints on Primary Productivity, Adaptive Patterns of Energy Capture in Plants, Harvard Forest, August 1983*. Cambridge [Cambridgeshire]: Cambridge University Press, c1986..
- Hall, A. E., & Schulze, E. D. (1980). Stomatal response to environment and a possible interrelation between stomatal effects on transpiration and CO₂ assimilation. *Plant, Cell & Environment*, 3(6), 467-474.
- Hari, P., Mäkelä, A., Korpilahti, E., & Holmberg, M. (1986). Optimal control of gas exchange. *Tree physiology*, 2(1-2-3), 169-175.
- Harley, P. C. and Baldocchi, D. 1995. Scaling carbon dioxide and water vapour exchange from leaf to canopy in a deciduous forest. I. Leaf model parametrization. *Plant, Cell Environ.* 18, 1146–1156.
- Hartmann H. (2015). Carbon starvation during drought-induced tree mortality – are we chasing a myth? *J Plant Hydraulics*, 2:005.
- Herkelrath WN, Miller EE, Gardner WR. 1977. Water uptake by plants: II. The root contact model. *Soil Science Society of America Journal* 41: 1039–1043.
- Hoch, G., Körner, C. (2003) The carbon charging of pines at the climatic tree line: a global comparison. *Oecologia* 135, 10–21.
- Hölttä, T., Vesala, T., Sevanto, S., Perämäki, M., & Nikinmaa, E. (2006). Modeling xylem and phloem water flows in trees according to cohesion theory and Münch hypothesis. *Trees*, 20(1), 67-78.
- Hölttä, T., Mencuccini, M., & Nikinmaa, E. (2009). Linking phloem function to structure: analysis with a coupled xylem–phloem transport model. *Journal of theoretical biology*, 259(2), 325-337.
- Hölttä, T., Mäkinen, H., Nöjd, P., Mäkelä, A., & Nikinmaa, E. (2010). A physiological model of softwood cambial growth. *Tree Physiology*, 30(10), 1235-1252.

- Hölttä, T., Kurppa, M., & Nikinmaa, E. (2013). Scaling of xylem and phloem transport capacity and resource usage with tree size. *Frontiers in plant science*, 4, 496.
- Hölttä, T., Lintunen, A., Chan, T., Mäkelä, A., & Nikinmaa, E. (2017). A steady-state stomatal model of balanced leaf gas exchange, hydraulics and maximal source–sink flux. *Tree physiology*, 37(7), 851–868.
- Horn, H. S. (2000). Twigs, trees, and the dynamics of carbon in the landscape. *Scaling in biology*, 199–220.
- Jackson, R. B., Canadell, J., Ehleringer, J. R., Mooney, H. A., Sala, O. E., & Schulze, E. D. (1996). A global analysis of root distributions for terrestrial biomes. *Oecologia*, 108(3), 389–411.
- Janssens, I. A., Sampson, D. A., Cermak, J., Meiresonne, L., Riguzzi, F., Overloop, S., & Ceulemans, R. (1999). Above-and belowground phytomass and carbon storage in a Belgian Scots pine stand. *Annals of Forest Science*, 56(2), 81–90.
- Jones, S., Rowland, L., Cox, P., Hemming, D., Wiltshire, A., Williams, K., ... & Mencuccini, M. (2019). The Impact of a Simple Representation of Non-Structural Carbohydrates on the Simulated Response of Tropical Forests to Drought. *Biogeosciences Discussions*, 1–26.
- Kalnay, E., Kanamitsu, M., Kistler, R., Collins, W., Deaven, D., Gandin, L., ... & Zhu, Y. (1996). The NCEP/NCAR 40-year reanalysis project. *Bulletin of the American meteorological Society*, 77(3), 437–472.
- Körner, C. (2015). Paradigm shift in plant growth control. *Current opinion in plant biology*, 25, 107–114.
- Lacointe, A., & Minchin, P. E. (2008). Modelling phloem and xylem transport within a complex architecture. *Functional Plant Biology*, 35(10), 772–780.
- Lawrence, D. M., Fisher, R. A., Koven, C. D., Oleson, K. W., Swenson, S. C., Bonan, G., ... & Kluzek, E. (2019). The Community Land Model version 5: Description of new features, benchmarking, and impact of forcing uncertainty. *Journal of Advances in Modeling Earth Systems*, 11(12), 4245–4287.
- LeBauer, D. S., & Treseder, K. K. (2008). Nitrogen limitation of net primary productivity in terrestrial ecosystems is globally distributed. *Ecology*, 89(2), 371–379.
- Li, Y., Tian, D., Yang, H., & Niu, S. (2018). Size-dependent nutrient limitation of tree growth from subtropical to cold temperate forests. *Functional Ecology*, 32(1), 95–105.
- Lintunen, A., Paljakka, T., Salmon, Y., Dewar, R., Riikonen, A., & Hölttä, T. (2019). The influence of soil temperature and water content on belowground hydraulic conductance and leaf gas exchange in mature trees of three boreal species. *Plant, Cell & Environment*.
- Lockhart, J. A. (1965). An analysis of irreversible plant cell elongation. *Journal of theoretical biology*, 8(2), 264–275.
- Luo, Y., Hui, D., & Zhang, D. (2006). Elevated CO₂ stimulates net accumulations of carbon and nitrogen in land ecosystems: A meta-analysis. *Ecology*, 87(1), 53–63.

- Mackay, D. S., Roberts, D. E., Ewers, B. E., Sperry, J. S., McDowell, N. G., & Pockman, W. T. (2015). Interdependence of chronic hydraulic dysfunction and canopy processes can improve integrated models of tree response to drought. *Water Resources Research*, 51, 6156–6176.
- Mackay, D. S., Savoy, P. R., Grossiord, C., Tai, X., Pleban, J. R., Wang, D. R., ... & Sperry, J. S. (2020). Conifers depend on established roots during drought: results from a coupled model of carbon allocation and hydraulics. *New Phytologist*, 225(2), 679-692.
- Magnani, F., Mencuccini, M., & Grace, J. (2000). Age-related decline in stand productivity: the role of structural acclimation under hydraulic constraints. *Plant, Cell & Environment*, 23(3), 251-263.
- Mäkelä, A. (1986). Implications of the pipe model theory on dry matter partitioning and height growth in trees. *J. Theor. Biol.*, 123. pp. 103-120.
- Mäkelä, A., Berninger, F., & Hari, P. (1996). Optimal control of gas exchange during drought: theoretical analysis. *Annals of Botany*, 77(5), 461-468.
- Mäkelä, A., Valentine, H. T., & Helmisaari, H. S. (2008). Optimal co-allocation of carbon and nitrogen in a forest stand at steady state. *New Phytologist*, 180(1), 114-123.
- Mäkelä, A., Leila Grönlund, Pauliina Schiestl-Aalto, Tuomo Kalliokoski, Teemu Hölttä. (2019). Current-year shoot hydraulic structure in two boreal conifers—implications of growth habit on water potential, *Tree Physiology*, tpz107.
- Manzoni S., Vico G., Katul G., Fay P.A., Polley W., Palmroth S. & Porporato A. (2011) Optimizing stomatal conductance for maximum carbon gain under water stress: a meta-analysis across plant functional types and climates. *Functional Ecology* 25, 456–467.
- Marshall, J. D., & Waring, R. H. (1985). Predicting fine root production and turnover by monitoring root starch and soil temperature. *Canadian Journal of Forest Research*, 15(5), 791-800.
- Martínez-Vilalta, J., Korakaki, E., Vanderklein, D., & Mencuccini, M. (2007). Below-ground hydraulic conductance is a function of environmental conditions and tree size in Scots pine. *Functional Ecology*, 21(6), 1072-1083.
- Martínez-Vilalta, J., Sala, A., Asensio, D., Galiano, L., Hoch, G., Palacio, S. et al. (2016). Dynamics of non-structural carbohydrates in terrestrial plants: a global synthesis. *Ecol. Monogr.*, 86, 495–516.
- McDowell, N. G., Beerling, D. J., Breshears, D. D., Fisher, R. A., Raffa, K. F., & Stitt, M. (2011). The interdependence of mechanisms underlying climate-driven vegetation mortality. *Trends in ecology & evolution*, 26(10), 523-532.
- McLaughlin, B. C., Blakey, R., Weitz, A. P., Feng, X., Brown, B. J., Ackerly, D. D., ... & Thompson, S. E. (2020). Weather underground: Subsurface hydrologic processes mediate tree vulnerability to extreme climatic drought. *Global change biology*, 26(5), 3091-3107.
- McMahon, T.A. (1973) Size and shape in biology. *Science*, 179, 1201–1204.
- McMurtrie, R. E., Norby, R. J., Medlyn, B. E., Dewar, R. C., Pepper, D. A., Reich, P. B., & Barton, C. V. (2008). Why is plant-growth response to elevated CO₂ amplified when water is limiting, but reduced when nitrogen is limiting? A growth-optimisation hypothesis. *Functional Plant Biology*, 35(6), 521-534.

- Meir, P., B. Kruijt, M. Broadmeadow, E. Barbosa, O. Kull, F. Carswell, A. Nobre and P.G. Jarvis. (2002). Acclimation of photosynthetic capacity to irradiance in tree canopies in relation to leaf nitrogen concentration and leaf mass per unit area. *Plant Cell Environ.* 25:343–357.
- Mencuccini, M., John Grace. (1996). Hydraulic conductance, light interception and needle nutrient concentration in Scots pine stands and their relations with net primary productivity, *Tree Physiology*, Volume 16, Issue 5, pages 459–468.
- Mencuccini, M., Martínez-Vilalta, J., Vanderklein, D., Hamid, H. A., Korakaki, E., Lee, S., & Michiels, B. (2005). Size-mediated ageing reduces vigour in trees. *Ecology letters*, 8(11), 1183–1190.
- Merganičová, Katarína, Ján Merganič, Aleksi Lehtonen, Giorgio Vacchiano, Maša Zorana Ostrogović Sever, Andrey L D Augustynczyk, Rüdiger Grote, Ina Kyselová, Annikki Mäkelä, Rasoul Yousefpour, Jan Krejza, Alessio Collalti, Christopher P O Reyer. (2019). Forest carbon allocation modelling under climate change, *Tree Physiology*, tpz105.
- Millard, P., Sommerkorn, M., & Grelet, G. A. (2007). Environmental change and carbon limitation in trees: a biochemical, ecophysiological and ecosystem appraisal. *New Phytologist*, 175(1), 11–28.
- Newman EI (1969). Resistance to water flow in soil and plant. II. A review of experimental evidence on the rhizosphere resistance. *J Appl Ecol* 6:261–272.
- Nikinmaa, E., Hölttä, T., Hari, P., Kolari, P., Mäkelä, A., Sevanto, S., & Vesala, T. (2013). Assimilate transport in phloem sets conditions for leaf gas exchange. *Plant, Cell & Environment*, 36(3), 655–669.
- Niklas, K. J., & Spatz, H. C. (2004). Growth and hydraulic (not mechanical) constraints govern the scaling of tree height and mass. *Proceedings of the National Academy of Sciences*, 101(44), 15661–15663.
- Novick, K. A., Miniati, C. F., & Vose, J. M. (2016). Drought limitations to leaf-level gas exchange: results from a model linking stomatal optimization and cohesion–tension theory. *Plant, cell & environment*, 39(3), 583–596.
- Oleson, K. W., Lawrence, D. M., Gordon, B., Flanner, M. G., Kluzek, E., Peter, J., ... & Heald, C. L. (2010). *Technical description of version 4.0 of the Community Land Model (CLM)*. NCAR Tech. Note. NCAR/TN-4781STR.
- Oleson, K. W., Lawrence, D. M., Bonan, G. B., Drewniak, B., Huang, M., Koven, C. D., ... & Swenson, S. C. (2013). *Technical description of version 4.5 of the community land model (CLM)*, NCAR Tech. Note. NCAR/TN-503+ STR.
- Penman HL. 1948. Natural evaporation from open water, bare soil and grass. *Proceedings of the Royal Society of London, Series A, Mathematical and Physical Sciences*, 193, 1032, 120–145.
- Philip JR, de Vries DA. (1957). Moisture movement in porous materials under temperature gradients. *Transactions American Geophysical Union*, vol. 38, no. 2, pp. 222–232.
- Poorter, H., & Nagel, O. (2000). The role of biomass allocation in the growth response of plants to different levels of light, CO₂, nutrients and water: a quantitative review. *Functional Plant Biology*, 27(12), 1191–1191.

- Poorter, H., Niklas, K. J., Reich, P. B., Oleksyn, J., Poot, P., & Mommer, L. (2012). Biomass allocation to leaves, stems and roots: meta-analyses of interspecific variation and environmental control. *New Phytologist*, 193(1), 30-50.
- Poorter, H., Jagodzinski, A. M., Ruiz-Peinado, R., Kuyah, S., Luo, Y., Oleksyn, J., ... & Sack, L. (2015). How does biomass distribution change with size and differ among species? An analysis for 1200 plant species from five continents. *New Phytologist*, 208(3), 736-749.
- Poyatos, R., Aguadé, D., Galiano, L., Mencuccini, M., & Martínez-Vilalta, J. (2013). Drought-induced defoliation and long periods of near-zero gas exchange play a key role in accentuating metabolic decline of Scots pine. *New Phytologist*, 200(2), 388-401.
- Poyatos, R., Aguadé, D., & Martínez-Vilalta, J. (2018). Below-ground hydraulic constraints during drought-induced decline in Scots pine. *Annals of forest science*, 75(4), 100.
- Reyer, C. P. O., Silveyra Gonzalez, R., Dolos, K., Hartig, F., Hauf, Y., Noack, M., Lasch-Born, P., Rötzer, T., Pretzsch, H., Mesenburg, H., Fleck, S., Wagner, M., Bolte, A., Sanders, T. G. M., Kolari, P., Mäkelä, A., Vesala, T., Mammarella, I., Pumpanen, J., Collalti, A., Trotta, C., Matteucci, G., D'Andrea, E., Foltýnová, L., Krejza, J., Ibrom, A., Pilegaard, K., Loustau, D., Bonnefond, J.-M., Berbigier, P., Picart, D., Lafont, S., Dietze, M., Cameron, D., Vieno, M., Tian, H., Palacios-Orueta, A., Cicuendez, V., Recuero, L., Wiese, K., Büchner, M., Lange, S., Volkholz, J., Kim, H., Weedon, G. P., Sheffield, J., Vega del Valle, I., Suckow, F., Horemans, J. A., Martel, S., Bohn, F., Steinkamp, J., Chikalanov, A., Mahnken, M., Gutsch, M., and Frieler, K. (2019). The PROFOUND database for evaluating vegetation models and simulating climate impacts on forests, *Earth Syst. Sci. Data Discuss.*
- Richards, L.A. 1931. Capillary conduction of liquids through porous medium. *Physics* 1:318–333.
- Richardson, L.F. 1922. Weather prediction by numerical process. University Press, Cambridge. p. 262.
- Richardson, A. D., Carbone, M. S., Keenan, T. F., Czimczik, C. I., Hollinger, D. Y., Murakami, P., ... & Xu, X. (2013). Seasonal dynamics and age of stemwood nonstructural carbohydrates in temperate forest trees. *New Phytologist*. 197: 850-861., 197, 850-861.
- Sabot, M. E., De Kauwe, M. G., Pitman, A. J., Medlyn, B. E., Verhoef, A., Ukkola, A. M., & Abramowitz, G. (2019). Plant profit maximization improves predictions of European forest responses to drought. *New Phytologist*.
- Salmon, Y., Lintunen, A., Dayet, A., Chan, T., Dewar, R., Vesala, T., & Hölttä, T. (2020). Leaf carbon and water status control stomatal and nonstomatal limitations of photosynthesis in trees. *New Phytologist*, 226(3), 690-703.
- Savage, V. M., Bentley, L. P., Enquist, B. J., Sperry, J. S., Smith, D. D., Reich, P. B., & Von Allmen, E. I. (2010). Hydraulic trade-offs and space filling enable better predictions of vascular structure and function in plants. *Proceedings of the National Academy of Sciences*, 107(52), 22722-22727.
- Schenk, H. J. (2005). Vertical vegetation structure below ground: scaling from root to globe. In *Progress in botany* (pp. 341-373). Springer, Berlin, Heidelberg.
- Schiestl-Aalto, P., Ryhti, K., Mäkelä, A., Peltoniemi, M., Bäck, J., & Kulmala, L. (2019). Analysis of the NSC storage dynamics in tree organs reveals the allocation to belowground symbionts in the framework of whole tree carbon balance. *Frontiers in Forests and Global Change*, 2, 17.

- Shao, J., Si, B., & Jin, J. (2019). Rooting depth and extreme precipitation regulate groundwater recharge in the thick unsaturated zone: A case study. *Water*, 11(6), 1232.
- Shinozaki, K., Yoda, K., Hozumi, K., & Kira, T. (1964). A quantitative analysis of plant form-the pipe model theory: I. Basic analyses. *Japanese Journal of ecology*, 14(3), 97-105.
- Smith, D. D., & Sperry, J. S. (2014). Coordination between water transport capacity, biomass growth, metabolic scaling and species stature in co-occurring shrub and tree species. *Plant, Cell & Environment*, 37(12), 2679-2690.
- Sperry, J.S., Adler, F.R., Campbell, G.S. & Comstock, J.P. (1998) Limitation of plant water use by rhizosphere and xylem conductance: results from a model. *Plant, Cell and Environment*, 21, 347–359.
- Sperry, J. S., Smith, D. D., Savage, V. M., Enquist, B. J., McCulloh, K. A., Reich, P. B., ... & von Allmen, E. I. (2012). A species-level model for metabolic scaling in trees I. Exploring boundaries to scaling space within and across species. *Functional Ecology*, 26(5), 1054-1065.
- Sperry J.S. & Love D.M. (2015) Tansley review: What plant hydraulics can tell us about plant responses to climate-change droughts. *New Phytologist* 207, 14–27.
- Sperry J.S., Wang Y., Wolfe B., Mackay D.S., Anderegg W.R.L., McDowell N.G. & Pockman W.T. (2016) Pragmatic hydraulic theory predicts stomatal responses to climatic water deficits. *New Phytologist* 212, 577–589.
- Sperry, J. S., Venturas, M. D., Anderegg, W. R., Mencuccini, M., Mackay, D. S., Wang, Y., & Love, D. M. (2017). Predicting stomatal responses to the environment from the optimization of photosynthetic gain and hydraulic cost. *Plant, cell & environment*, 40(6), 816-830.
- Sperry, J. S., Venturas, M. D., Todd, H. N., Trugman, A. T., Anderegg, W. R., Wang, Y., & Tai, X. (2019). The impact of rising CO₂ and acclimation on the response of US forests to global warming. *Proceedings of the National Academy of Sciences*, 116(51), 25734-25744.
- Sprugel, D. G., Ryan, M. G., Brooks, J. R., Vogt, K. A., & Martin, T. A. (1995). Respiration from the organ level to the stand. In *Resource physiology of conifers* (pp. 255-299). Academic Press.
- Steppe, K., De Pauw, D. J., Lemeur, R., & Vanrolleghem, P. A. (2006). A mathematical model linking tree sap flow dynamics to daily stem diameter fluctuations and radial stem growth. *Tree physiology*, 26(3), 257-273.
- Steudle, E., & Peterson, C. A. (1998). How does water get through roots?. *Journal of experimental Botany*, 49(322), 775-788.
- Strigul, N., Pristinski, D., Purves, D., Dushoff, J., & Pacala, S. (2008). Scaling from trees to forests: tractable macroscopic equations for forest dynamics. *Ecological Monographs*, 78(4), 523-545.
- Tetens O.(1930). Über einige meteorologische Begriffe. *Z. Geophys* 6, 207-309.
- Thomas, D. S., Eamus, D., & Bell, D. (1999). Optimization theory of stomatal behaviour: II. Stomatal responses of several tree species of north Australia to changes in light, soil and atmospheric water content and temperature. *Journal of Experimental Botany*, 50(332), 393-400.

- Thompson, M. V., & Holbrook, N. M. (2003). Application of a single-solute non-steady-state phloem model to the study of long-distance assimilate transport. *Journal of Theoretical Biology*, 220(4), 419-455.
- Torres-Ruiz, J. M., Cochard, H., Mencuccini, M., Delzon, S., and Badel, E. (2016) Direct observation and modelling of embolism spread between xylem conduits: a case study in Scots pine. *Plant, Cell & Environment*, 39: 2774–2785.
- Trugman, A. T., Detto, M., Bartlett, M. K., Medvigy, D., Anderegg, W. R. L., Schwalm, C., ... & Pacala, S. W. (2018). Tree carbon allocation explains forest drought-kill and recovery patterns. *Ecology letters*, 21(10), 1552-1560.
- van Genuchten, M. T. (1980). A closed-form equation for predicting the hydraulic conductivity of unsaturated soils 1. *Soil science society of America journal*, 44(5), 892-898.
- Venturas, M. D., Sperry, J. S., Love, D. M., Frehner, E. H., Allred, M. G., Wang, Y., & Anderegg, W. R. (2018). A stomatal control model based on optimization of carbon gain versus hydraulic risk predicts aspen sapling responses to drought. *New Phytologist*, 220(3), 836-850.
- von Allmen, E.I., Sperry, J.S., Smith, D.D., Savage, V.M., Enquist, B.J., Reich, P.B. and Bentley, L.P. (2012). A species-level model for metabolic scaling of trees II. Testing in a ring- and diffuse-porous species. *Funct Ecol*, 26: 1066-1076.
- Walker, A. P., Hanson, P. J., De Kauwe, M. G., Medlyn, B. E., Zaehle, S., Asao, S., ... & Norby, R. J. (2014). Comprehensive ecosystem model-data synthesis using multiple data sets at two temperate forest free-air CO₂ enrichment experiments: Model performance at ambient CO₂ concentration. *Journal of Geophysical Research: Biogeosciences*, 119(5), 937-964.
- Wang, Y., Sperry, J. S., Venturas, M. D., Trugman, A. T., Love, D. M., & Anderegg, W. R. (2019). The stomatal response to rising CO₂ concentration and drought is predicted by a hydraulic trait-based optimization model. *Tree physiology*, 39(8), 1416-1427.
- West, G. B., Brown, J. H., & Enquist, B. J. (1999). A general model for the structure and allometry of plant vascular systems. *Nature*, 400(6745), 664-667.
- West GB, Enquist BJ, Brown JH. (2009). A general quantitative theory of forest structure and dynamics. *Proc Natl Acad Sci USA* 106(17):7040–7045.
- Wolf, A., Anderegg, W. R., & Pacala, S. W. (2016). Optimal stomatal behavior with competition for water and risk of hydraulic impairment. *Proceedings of the National Academy of Sciences*, 113(13), E7222-E7230.
- Yoder, B. J., Ryan, M. G., Waring, R. H., Schoettle, A. W., & Kaufmann, M. R. (1994). Evidence of reduced photosynthetic rates in old trees. *Forest Science*, 40(3), 513-527.
- Zha, T., Kellomäki, S., Wang, K. Y., Ryyppö, A., & Niinistö, S. (2004). Seasonal and annual stem respiration of Scots pine trees under boreal conditions. *Annals of Botany*, 94(6), 889-896.